B-SITE CATION MIXED MULTIFERROIC PEROVSKITE MATERIALS

SUEN WAI PING

M.Phil

The Hong Kong Polytechnic University

2010

The Hong Kong Polytechnic University

Department of Applied Physics

B-Site Cation Mixed Multiferroic Perovskite Materials

Suen Wai Ping

A thesis submitted in partial fulfilment of the requirements for the degree of Master of Philosophy

August 2009

Certificate of Originality

I hereby declare that this thesis is my own work and that, to the best of my knowledge and belief, it reproduces no material previously published or written nor material which has been accepted for the award of any other degree or diploma, except where due acknowledgement has been made in the text.

_____(Signed)

SUEN WAI PING (Name of student)

Abstract

In recent years, investigation in multiferroic materials has attracted considerable interest as these materials can simultaneously exhibit ferroelectric and magnetic properties. It is expected that the interaction between electric and magnetic orders will give rise to novel properties and hence attractive for practical applications. $BiFeO_3$ (BFO) is a promising multiferroic material because it possesses ferroelectric and antiferromagnetic behaviors at room temperature. However, the coupling between the ferroelectric and magnetic behaviors is very small and results in limited applications. Therefore, doping is sought after to improve the coupling. It has been reported that the solid solution between BFO and another multiferroic material $BiMnO_3$ (BMO) can have better electric and magnetic coupling. However, the underlying mechanism is not fully understood. Particularly, the relationship between the microstructure and the physical properties, which is important for complex perovskite oxides, is unclear. Therefore we propose to give a comprehensive study on the property-microstructure relationship of BFO-BMO solid solution.

In this project, the solid solution $BiFe_{1-x}Mn_xO_3$ (BFMO) has been prepared by several methods including the rapid liquid-phase sintering technique. The effects of Mn doping level on both the microstructures and properties have been examined. These include the doping induced variations in lattice parameters, microstructure, dielectric properties, ferroelectric properties, magnetic properties, and phase

transition temperature, etc. From the results obtained, it is found that single phase ceramics could only be obtained in BFMO compound when $x \leq 0.4$. A structural phase transition took place from rhombohedral to tetragonal when the Mn doping level was increased to $x=0.4$. This result was consistence with the Raman analysis. The dielectric properties of BFMO were investigated in the frequency range of 10 Hz to 10 MHz over a broad temperature range. When Mn was doped into the solid solution, the dielectric constant was drastically increased and a relaxation peak corresponding to a step-decrease in dielectric constant was also observed. The relaxation peak was shifted to a higher frequency with increasing Mn concentration. The activation energy for the dielectric relaxation was found to decrease from 0.39 ($x=0.1$) to 0.29 eV ($x=0.4$), indicating a Mn-related polaron hopping motion Fe^{3+} and Mn^{3+} ions. The impedance of grain and grain boundary was resolved by an equivalent circuit model. The activation energies for grain and grain boundary conductions were similar and could be explained by a constriction model where the grain and grain boundary conductions have the same mechanism. Magnetic hysteresis loop measurements showed that the magnetization of the solid solution increased with increasing amount of Mn substitution. This result was consistent with the XPS analysis. Moreover, the microstructures of the ceramic samples were studied by electron diffraction. Superlattice structures were observed in Mn doped samples, where computer simulation was used to find out possible chemical ordering in the structure.

Different synthesized techniques were used to synthesize BFO and

comparisons were made with respect to their physical properties. Single phase BFO could only be synthesized by the rapid liquid-phase sintering and wet chemical reaction methods. BFO synthesized by the rapid liquid-phase sintering technique exhibited the least leakage current and therefore best ferroelectric properties. The wet chemical reaction method was effective to obtain stoichiometric and stable single phase BFO, which is a reliable method worthy of further investigation.

List of Publications

1. H.Huang, S.Ke, M.Cao, W.P.Suen and H.L.W.Chan, "A microscopic model for the dielectric behavior in a series of giant/colossal dielectric constant materials", (under preparation)

2. S.Ke, W.P.Suen, H.Huang and H.L.W.Chan, "Nanosized $BiFeO_3$ powders synthesized by a wet chemical route", (under preparation)

3. W.P.Suen, S.Ke, H.Huang and H.L.W.Chan, "Colossal dielectric constant and polaronic conduction in Mn-doped $BiFeO_3$", (under preparation)

4. W. P. Suen, H. Huang and H. L.W. Chan, "Effect of Mn substitution in Multiferroic $BiFeO_3$ Ceramics", PP-33, International Union of Materials Research Societies, (2008)

Acknowledgements

I would like to express my sincere gratitude to my supervisors Dr. H.T. Huang and Prof. H.L.W. Chan, who gave me lots of patience, supports and guidance to meet the project goal throughout the whole period of my research study. I would also like to thank Dr. S.M. Ke for providing invaluable supports and suggestions to this work.

I would also like to thank Mr. M. N. Yeung of the Material Research Center for his assistance in the material characterization. My thanks are also extended to Dr. W. Lu for his help in TEM operation. Thanks are also given to Mr. K. C. Chan for training me in VSM operation.

I would like to give my thanks to my colleagues and friends in AP: Mr. M. X. Cao, Miss. Y. Ye, Dr. H. Wang, Mr. K. Zhang, Mr. J. Yong, Dr. Y. B. Yao, Mr. K. F. Cheung, Mr. C. M. Leung, Miss. S.F. Hon, Miss. N. W. Fong, Miss. H. L. Li, Mr. H. F. Wong, Mr. W. K. Li, Mr. H. K. Lau, Mr. J. Liu and Miss. K. C. Chan. I owe special thanks to their assistance and discussions in the research work.

I gratefully acknowledge the financial support from the Research Grants Council of the Hong Kong Special Administrative Region and the Department of Applied Physics, the Hong Kong Polytechnic University.

Last but not least, I would like to express my deepest appreciations to my family and my best friend for their support, encouragement and enduring love.

Table of Content

List of Figure Captions

List of Table Captions

Chapter 1
Introduction

1.1 Research background

In 1894, Curie proposed a possible magnetoelectric (ME) effect on a crystal according to symmetry considerations [1]. The searching for ME materials started mainly in Russia, United Kingdom and France in the 1950's and 1960's. However, limited progress was made during the past several decades since when ferroelectric and ferromagnetic properties coexist in the same material, the coupling between them turns out to be rather weak. With the advancement in synthesis technique to obtain high quality samples, multiferroic materials have gained rejuvenated interest [2-4], especially in materials with an ABO_3 perovskite structure. Due to the coupling between ferroelectric and ferromagnetic orderings, it is possible to control or switch the electric polarization via magnetic field or *vice versa*. The ME coupling in multiferroic materials is expected to give rise to novel properties and potential applications. For examples, multiferroic materials can be used in multiple-state memory elements where the data are stored in both electric and magnetic polarizations, or in novel memory media which allow the writing of a ferroelectric data bit by an electric field and the reading of magnetization data associated with the change in electric polarization [5]. In addition, the ME coupling also allows extra degrees of freedom in the design of novel actuators, transducers, and storage devices [6]. Apart from many potential applications, the fundamental

physics of multiferroic materials is also rich and fascinating. The mechanism of the coupling between the electric and magnetic orders in multiferroic materials is still not thoroughly understood.

In this chapter, we will provide some background information on perovskite materials and outline the relationship between the physical (electronic and magnetic) properties and their structures. After that, we will give a brief description of the theoretical approach to the understanding of the origin of magnetoelectric effect in perovskite structure. The remaining part of this chapter is devoted to the description of the physical properties of Bi-based perovskites: $BiFeO_3$, $BiMnO_3$, and their solid solutions. The effect of cation ordering on the physical properties, such as structural, electric, magnetic and magnetoelectric properties, will be discussed in the final part of this chapter.

1.2 General description of a perovskite structure

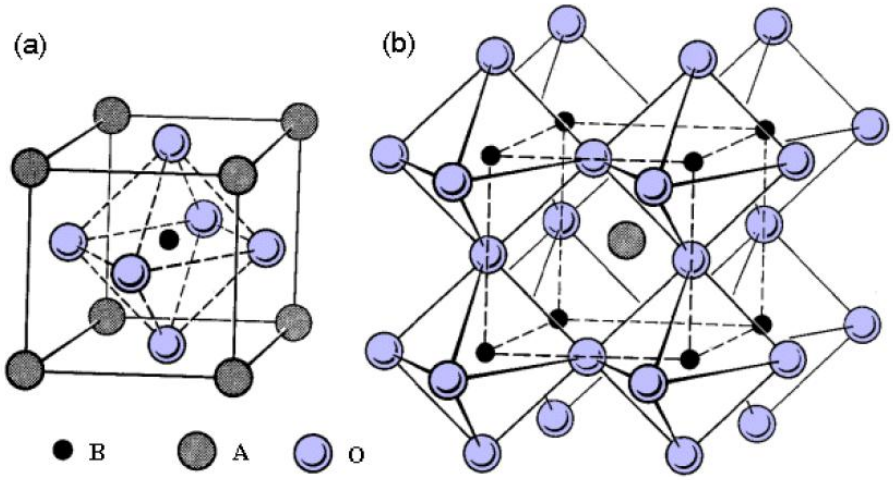

Figure 1.1 Schematic drawing of ABO_3 perovskite: (a) simple cubic structure and (b) simple cubic structure highlighting the corner linked oxygen octahedra.

Perovskite structure is one of the most common structures in complex oxides. A typical perovskite structure has a stoichiometric chemical formula of ABO_3, where O is an anion (usually oxygen) and A and B are cations. Typically, the A-cation is a larger cation with lower valence to form close-packed layer with O^{2-}. The B-cation is typically smaller with higher valence state which can be adopted into an oxygen octahedral coordination environment. The simplest perovskite structure is a cubic, corresponding to a high temperature phase. It is shown in Figure 1.1(a), where the B-cation is at the body centre,

A-cation at the corners of the cube, and oxygen at the face centre. Alternatively, the structure can be viewed as a 3D network of corner sharing BO_6 octahedra as shown in Figure 1.1(b) where the A-cation sits in a cube and is surrounded by 12 O atoms.

The mismatch in ionic radius will easily cause distortions in the perovskite structure, which includes the tilting of oxygen octahedra. In 1926, Goldschmidt introduced a parameter called tolerance factor t to describe the stability of a perovskite structure. This factor is related to the ionic radius and is obtained based on the concept of close-packed structure. It is given by [7],

$$t = \frac{r_A + r_0}{\sqrt{2}\left(r_B + r_O\right)} \tag{1.1}$$

where r_A, r_B, and r_O are the ionic radii of A, B, and O, respectively.

For an ideal cubic perovskite structure, the tolerance factor t is unity. A stable perovskite structure can be obtained when the tolerance factor is within the range of 0.77~1.05. This factor is particularly useful in the study of the degree of structural distortion and the tilting of oxygen octahedra and hence, it is useful in the prediction of materials properties. When $0.985 < t < 1.05$, there is no structural distortion and no octahedral tilting. When $0.965 < t < 0.985$, octahedra antiphase tilting is resulted. When $t < 0.965$, antiphase and/or inphase tilting of octahedra occurs [8, 9]. Different tilting systems can cause different combinations of superlattice spots in electron diffraction

patterns. Detailed discussion can be found in ref. [10].

1.3 Ferroelectric and (ferro) magnetic oxides with a perovskite structure

Transition metal oxides with a perovskite structure form a large group of compounds with interesting properties. Fundamentally, the *d*-electron configuration of the B-cation appears to play an important role in the physical (ferroelectric and (ferro) magnetic) properties.

1.3.1 Ferroelectric phenomena in perovskite structures

In a perovskite structure, if the B-cation has an empty *d*-electron configuration, the tendency for the B-cation to form a strong covalent bonding with neighboring oxygen ions is large. Hence, the B-cation tends to move away from the centrosymmetric position when the temperature goes down below the Curie temperature. The symmetry of the structure is thus lowered and an electric dipolar polarization is generated. Taking $BaTiO_3$ as an example, which has no $3d$ electron for a Ti^{4+} ion, the ferroelectricity is induced by the off-center displacement of the Ti^{4+} ion below the Curie temperature [11].

1.3.2 Magnetic phenomena in perovskite structures

On the other hand, the magnetism of ABO_3 structure arises from the presence of unpaired *d* electrons of the B-cation. Figure 1.2(a-b) shows the magnetic moment

created by an electron through the orbiting and self-spinning. According to the Pauli's exclusion principle, one energy level can be occupied by at most two electrons with opposite spins. Therefore, magnetic moments can be generated if there are partially filled *d*-shells.

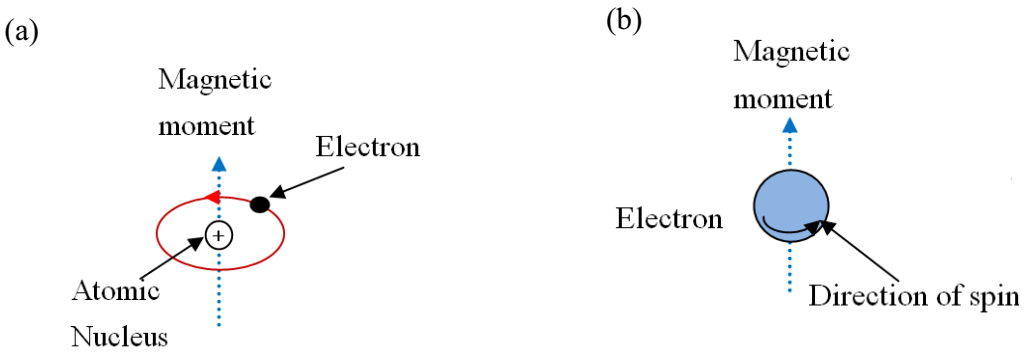

Figure 1.2 (a) Magnetic moment induced by orbiting; (b) Magnetic moment induced by electron spin.

Magnetism can be equated as following:

$$M = \chi H \tag{1.2}$$

$$\mu = 1 + \chi \tag{1.3}$$

where M is magnetization, H is magnetic field strength, χ is magnetic susceptibility, and μ is relative permeability [12].

Classification of Magnetic Behavior

In fact, there are many complex arrangements of magnetic ordering. For

simplicity, only three types of magnetic ordering will be discussed here. They are (1) ferromagnetic, (2) antiferromagnetic, and (3) ferrimagnetic ordering, as shown in Figure 1.3.

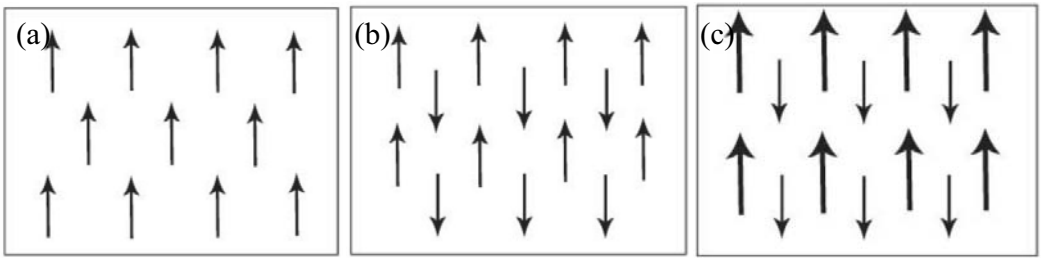

Figure 1.3 Three possible arragements of magnetic moment: (a) ferromagnetic, (b) antiferromagnetic, and (c) ferrimagnetic states.

Figure 1.3(a) indicates a ferromagnetic state. The electron spin moments within a domain are all pointing to the same direction as the external magnetic field. Hence, all the spins sum up to a nonzero value contributing to the localized magnetic moment even in the absence of an external magnetic field. The susceptibility of ferromagnetic material is therefore much larger than 1 [12].

Figure 1.3(b) shows an antiferromagnetic state. The magnetic moments associated with adjacent atoms or ions interact with each other in such a manner that they cancel each other by antiparallel arrangements. Thus, no net magnetic moment can be observed. The magnetic susceptibility of antiferromagnetic material is very small but positive [12].

Figure 1.3(c) shows a ferrimagnetic state. The magnetic moments on adjacent

atoms or ions are antiparallel, but unequal in magnitude. Therefore, the magnetic moments only partially cancel to each other and result in some net magnetization [12].

1.4 Multiferroic materials and magnetoelectric effect

Based on the above description it can be seen that, the requirements on the *d*-electron configuration for ferroelectric and ferromagnetic phenomena to occur in ABO_3 are conflict to each other, i.e., empty *d*-electron for ferroelectricity and unpaired *d*-electron for ferromagnetism. Hence, it is difficult to achieve ferroelectricity and ferromagnetism simultaneously through the manipulation of *d*-electrons. One of the strategies to overcome this difficulty is to introduce the electric polarization by A-site cation off-center displacement instead of the B-site one and to introduce the magnetic moment by unpaired *d*-electrons on the B-site cation. For example, the stereochemically active $6s^2$ lone pair electrons of the A-site cation may hybridize with an empty *p* orbital of oxygen to form a localized lobe, causing a structural distortion and ferroelectricity may result. Typical examples are $BiMnO_3$, $BiFeO_3$, and some Pb-based perovskite oxides that display ferroelectricity in spite of *d*-shell occupancy.

In the case of Bi based ions, because of the large orbital radius of the Bi $6s^2$ lone pairs, the crystal structure of bismuth-based perovskite is usually distorted and has a low symmetry, producing large spontaneous ferroelectric polarization along certain directions. At the same time, B-site transition-metal ions give rise to ferromagnetism or ferrimagnetism. If the magnetic and ferroelectric properties are coupled to each other,

these materials exhibit intrinsic multiferroic behaviors. The coupling between electric and magnetic orders results in the so called magnetoelectric (ME) or magnetocapacitance effect.

Theoretical study about the magnetoelectric coupling

ME effects include both the linear and non-linear responses to an external electric or magnetic field. They can be mathematically expressed in the following forms by an expansion of the free energy of a material,

$$F\left(\vec{E},\vec{H}\right) = F_0 - P_i^s E_i - M_i^s H_i - \frac{1}{2}\epsilon_0\epsilon_{ij} E_i E_j - \frac{1}{2}\mu_0\mu_{ij} H_i H_j - \alpha_{ij} E_i H_j - \frac{1}{2}\beta_{ijk} E_i H_j H_k - \cdots \quad (1.3)$$

$$P_i = -\frac{\partial F}{\partial E_i} = P_i^s + \epsilon_0\epsilon_{ij} E_j + \alpha_{ij} H_j + \frac{1}{2}\beta_{ijk} H_j H_k + \cdots \quad (1.4)$$

$$M_i = -\frac{\partial F}{\partial H_i} = M_i^s + \mu_0\mu_{ij} H_j + \alpha_{ij} E_i + \frac{1}{2}\beta_{ijk} E_i H_j + \cdots \quad (1.5)$$

where F is the free energy of a material, P is the electric polarization, M is the magnetization, E and H are the electric and magnetic fields, respectively. P^s and M^s are the spontaneous polarization and magnetization, respectively. ε and μ are the electric and magnetic susceptibilities, respectively. α and β are the linear and nonlinear ME susceptibilities, respectively [2].

1.5 Bismuth based multiferroic compounds

1.5.1 Bismuth ferrite ($BiFeO_3$)

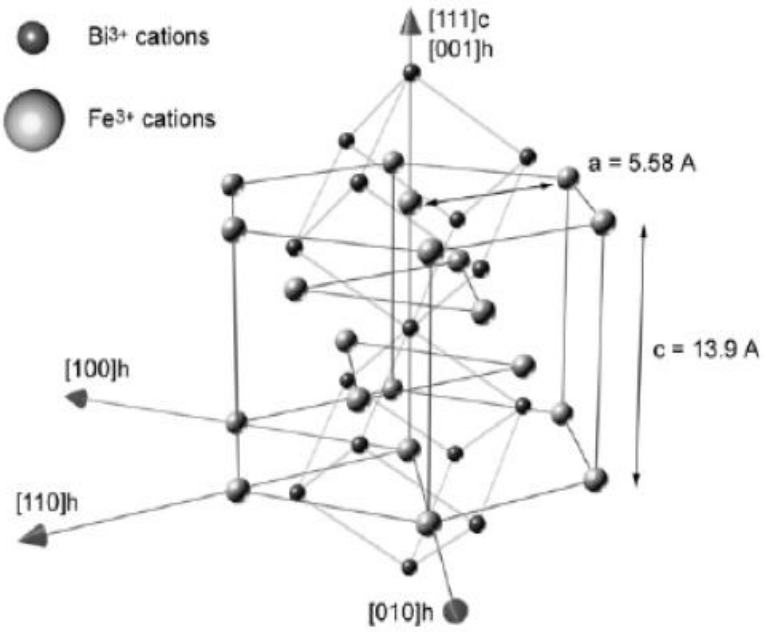

Figure 1.4 The hexagonal unit cell of $BiFeO_3$ [13].

Crystal structure

As a typical example of ME materials, $BiFeO_3$ (BFO) and its structure have been well studied [10, 14-21]. Bulk BFO belongs to the *R*3*c* space group with a highly distorted perovskite structure in rhombohedral symmetry. To gain structural stability, Bi and Fe atoms are moved along the pseudocubic <111> direction and O atoms along the

equivalent <110> directions. The unit cell is thus elongated with the neighboring oxygen octahedra rotated in opposite directions about the <111> axis. Sometimes, BFO can also be represented by a hexagonal structure as shown in Figure 1.4. The lattice parameters are a=3.96 Å and α=89.4° in the rhombohedral representation [19], or equivalently a=5.58 Å and c=13.9Å in the hexagonal representation [19, 20]. Since there are antiparallel octahedral tiltings around pseudocubic <111> directions, superlattice diffraction spots can be observed in this compound [10]. Moreover, this compound has high Curie ($T_C \approx 850$ °C) and Néel ($T_N \approx 370$ °C) temperatures [19, 21]. It shows ferroelectricity and a G-type antiferromagnetism at room temperature.

Ferroelectric and Magnetic properties

The ferroelectricity of $BiFeO_3$ comes from the A-site cation (Bi^{3+}) [22], which has $6s^2$ lone pair and moves away from the centro-symmetric position among neighboring oxygen octahedra. Such an off-center displacement will introduce a spontaneous polarization in the system. From the first-principles calculation, it has been predicted that $BiFeO_3$ has a large spontaneous polarization of 90–100 μC/cm^2 for a rhombohedral structure with a space group $R3c$ or 150 μC/cm^2 for a tetragonal structure [23]. The experimentally measured spontaneous polarization is usually significantly smaller than the theoretically predicted value for BFO in the bulk form [15, 16]. It is still not clear whether this is a result from the intrinsic material's property or from the imperfections in bulk materials.

Moreover, $BiFeO_3$ is G-type antiferromagnetic material. Fe^{3+} ion has five spins which are aligned in a half-filled 3*d* shell. These spins are coupled ferromagnetically in the pseudocubic (111) planes and antiferromagnetically between neighboring (111) planes. Hence the Fe spins form a G-type antiferromagnetic structure as shown in Figure 1.5. According to the neutron diffraction result, the magnetic structure of $BiFeO_3$ is spatially modulated. It is slightly modified to a cycloidal spiral pattern with a long period of 620 Å [24] and with the spiral propagation along the pseudocubic [110] direction as shown in Figure 1.6. The inhomogeneous spin structure of $BiFeO_3$ leads to the cancellation of the macroscopic magnetization [24, 25].

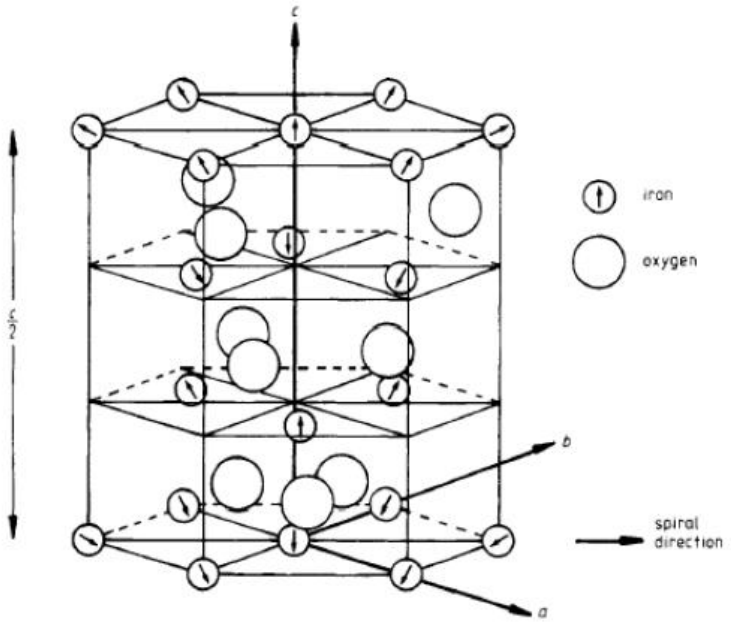

Figure 1.5 The hexagonal structure of $BiFeO_3$ with spiral period. The arrows indicate the Fe^{3+} spin moment direction of the proposed model [24].

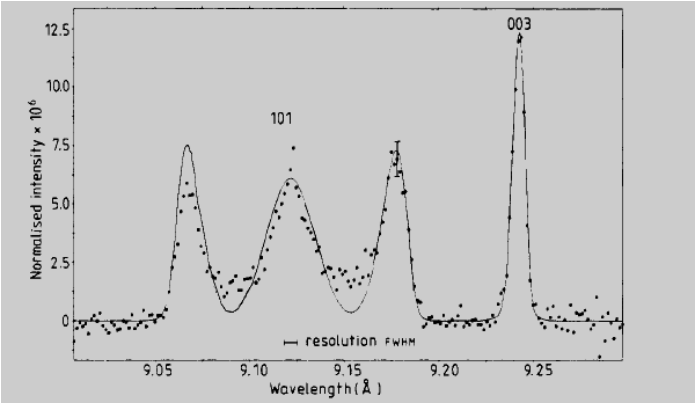

Figure 1.6 Neutron diffraction of $BiFeO_3$ [24].

Magnetoelectric coupling

Since ferroelectricity in BFO comes from Bi^{3+} and antiferromagnetism comes from Fe^{3+}, the coupling between magnetism and ferroelectricity is expected to be week. Popov *et al*. have showed that the destruction of the cycloidal structure by a high magnetic field of ~200 kOe may lead to the onset of a linear magnetoelectric effect [18]. Apart from the application of a large magnetic field [14], both chemical doping [26] and epitaxial strains in the case of thin films [5] can result in a linear magnetoelectric effect. However, for practical application purpose, both the resistivity and magnetization of BFO have to be increased.

1.5.2 Bismuth manganite ($BiMnO_3$)

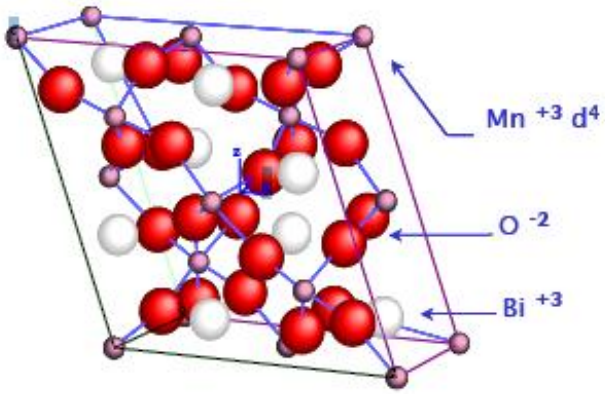

Figure 1.7 Monoclinic structure of $BiMnO_3$.

Crystal structure

Another interesting Bi-based perovskite compound is bismuth manganite ($BiMnO_3$). It is also considered as a multiferroic at low temperatures [27]. However, the information about $BiMnO_3$ is relatively limited. It is widely accepted that $BiMnO_3$ crystal has a distorted *C*2 monoclinic structure, with lattice parameters a = 9.5323 Å, b = 5.6064 Å, c = 9.8535 Å, and β = 110.667° [28]. It has also be reported to have a triclinically distorted perovskite structure with $a = c$ = 3.935 Å ($\alpha = \gamma$ = 91.4°) and b = 3.989 Å (β = 91.0°) [28].

$BiMnO_3$ is not stable at atmospheric pressure. Bulk $BiMnO_3$ can only be synthesized under high temperature (around 1100K) and high pressure (~3-6 GPa) in order to stabilize the highly distorted perovskite structure [29] and it is therefore a quite

impenetrable material for research.

Ferroelectric and ferromagnetic properties

In contrast to $BiFeO_3$, $BiMnO_3$ is ferromagnetic [30]. The ferromagnetic long range ordering below 105 K results from the orbital ordering of the Mn^{3+} ions ($3d^4$). A large magnetization of 3.6 μ_B/f.u. has been measured in polycrystalline samples, which is slightly smaller than that of the fully aligned spin value of 4 μ_B for Mn^{3+}. The magnetic moment of $BiMnO_3$ comes from orbital ordering, where among the six unique Mn–O–Mn superexchange pathways, 4 are ferromagnetic and 2 are antiferromagnetic [31]. This orbital ordering has been studied by both first-principles calculation and experiments [31].

The ferroelectricity in $BiMnO_3$ is still quite controversial. It is predicted to be a ferroelectric since it has a noncentrosymmetric structure which belongs to *C*2 space group and it has $6s^2$ lone pair electrons [22], which is similar to the situation in $BiFeO_3$. It is believed that the monoclinic to orthorhombic phase transition takes place at 773K [29], corresponding to the transition from a ferroelectric to a paraelectric phase. However, direct measurement on the ferroelectric hysteresis loop of $BiMnO_3$ is extremely difficult and the only reported value in the literature gave a very weak polarization of 0.043 $\mu C/cm^2$ at 200 K [32]. Even for samples with higher resistivity [33], the ferroelectric hysteresis loop was still unable to be observed at room temperature.

Magnetoelectric properties

Due to the intrinsic coupling between the ferroelectric and ferromagnetic orders in $BiMnO_3$, magnetodielectric effect has been observed in bulk samples [29]. Kimura *et al* [29] reported that the dielectric constant of the material changed with the external magnetic field. A fairly large negative magnetocapacitance was obtained near the ferromagnetic transition temperature T_C (105K). The maximum change observed was around 0.7% under a very large external field (9T) as shown in Figure 1.8. However, a deep understanding on the magnetoelectric coupling mechanism in $BiMnO_3$ is still lacking.

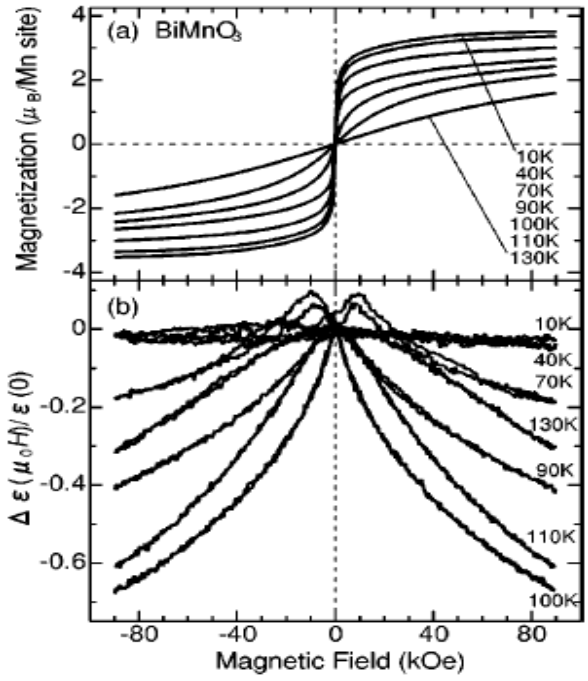

Figure 1.8 (a) Magnetizations and (b) field induced change in dielectric constant of $BiMnO_3$ as a function of a magnetic field at various temperatures [29].

1.6 Bi-based complex perovskite materials ($BiFe_{1-x}Mn_xO_3$)

From the above introduction on BFO and BMO perovskite ceramics, it can be seen that each of them has superior properties and limitations. BFO exhibits ferroelectric and antiferromagnetic properties at room temperature. However, its ME effect is very weak. While BMO has a stronger ME effect but only limited to lower temperatures. Hence, forming the solid solution between BFO and BMO could provide an alternative choice.

Several literature papers have reported the studies on the solid solution between BFO and BMO system [26, 34-42]. Using different synthesis methods, the obtained materials could have different structure and different composition range for the formation of solid solution. For example, under a high pressure synthesis method, 20-60 mol% Mn could enter into the lattice of BFO forming a orthorhombic structure and a doping of more than 60 mol % Mn could cause the solid solution to have a BMO-type monoclinic structure as verified from the XRD patterns shown in Figure 1.9 (a) [39]. However, for other methods under normal pressure, it was reported that the maximum amount of Mn that can be added into the solid solution is 30 mol% and the synthesized material has a BFO-type *R*3*c* rhombohedral structure as verified by the XRD patterns shown in Figure 1.9(b)[35, 38, 42]. The lattice parameters and unit cell volume decrease with increasing amount of Mn. With a small amount of A-site substitution (such as La), the maximum amount of Mn that can be added into the solid solution can be increased to

50 mol% [34, 36].

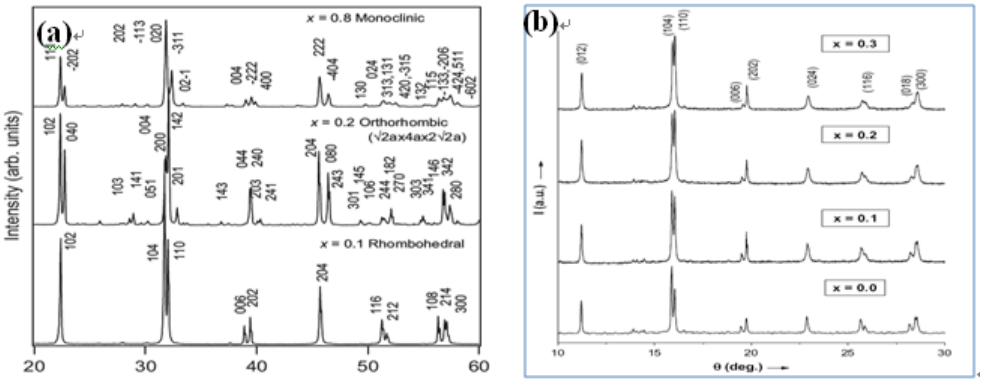

Figure 1.9 XRD patterns of $BiFe_{1-x}Mn_xO_3$ synthesized by (a) a high pressure method [39] and (b) a conventional solid state reaction method [35].

Magnetoelectric properties

In the ME study, preliminary results show that Mn doping can enhance magnetic properties [26, 34-42]. The enhancement in magnetization can be attributed to the suppression of the magnetic spiral spin structure observed in BFO. Sosnowska *et al*. reported that the periodicity of the spin modulation changed from 620 Å to 720 Å after the doping of 20 mol % Mn [26].

There are large variations on the ferroelectric and dielectric properties reported. As shown in Figure 1.10 [35, 36, 42], one group reported increased dielectric loss with increasing amount of Mn doping [35], while another group showed the opposite trend [42]. The lack of consistence and detailed analysis in the dielectric properties of the

BFO-BMO solid solution calls for a detailed study on this type of material.

A positive magnetocapacitance effect has also been found in $BiFe_{0.7}Mn_{0.3}O_3$ sample as shown in Figure 1.11 and this gives a rare example of the non-trivial magnetocapacitance effect at room temperature [38].

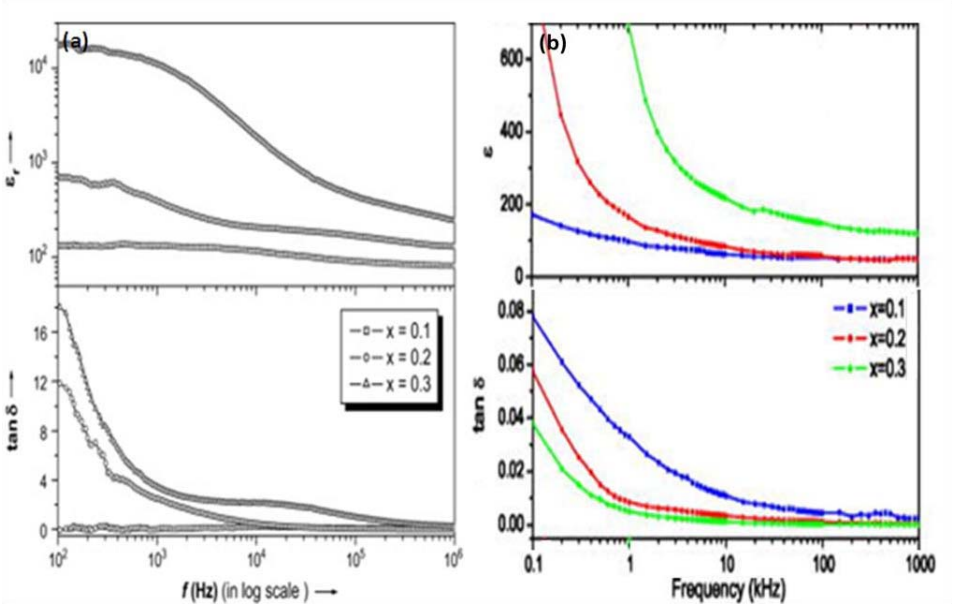

Figure 1.10 Dielectric properties of BFMO (x=0.1–0.3): (a) results reported by Sahu *et. al.* [35] and (b) results reported by Kumar *et. al.*[42].

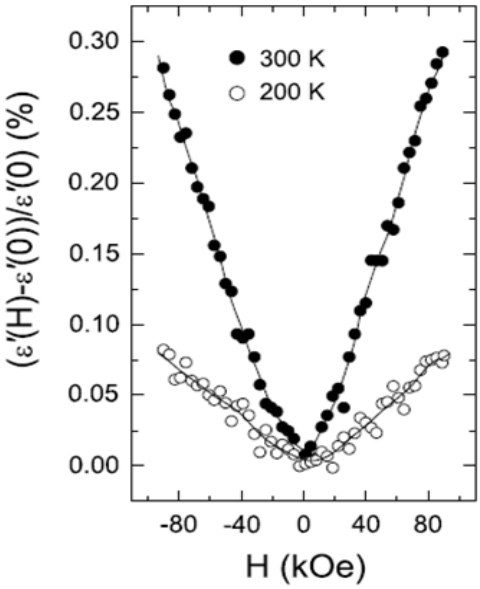

Figure 1.11 Magnetocapacitance effect of $BiFe_{0.7}Mn_{0.3}O_3$ measured at selected temperatures. Dielectric constant in the vertical axis designates the real part of complex dielectric permittivity measured at magnetic field H [38].

Apart from the many investigations in bulk systems, Mn-doped BFO thin film is also a hot topic of intensive research, especially after the Tokyo Institute of Technology and Fujitsu jointly developed a new generation of non-volatile ferroelectric random access memory (FeRAM) based on Mn-doped BFO thin-film capacitors. Such a FeRAM has enabled data storage capacity up to 5 times greater than the materials currently used in the FeRAM production [41]. It is believed that this material has high potential for future applications in the FeRAM field.

1.7 Cation ordering in complex perovskite oxides

Recently, chemical ordering in perovskite ABO_3 structure has attracted a lot of research interest [43-49] since ordering of the mixed metal A or B-site cations or oxygen anion can affect the symmetry of the structure, chemical stability, ferroelectric, dielectric, and magnetic responses, which are important materials properties [48, 50, 51].

There are several recent papers that have studied the stability, kinetic energy and physical properties of cation ordered complex perovskite oxides [52-58]. Wongmaneerung *et.al.* [57] have used $Pb[Sc_{2x/3}Fe_{(1/2-2x/3)}][Fe_{1/6}W_{1/3}]O_3$ complex perovskite oxide to study the relationship between the degree of cation ordering and saturation magnetization. They denoted $[Sc_{2x/3}Fe_{(1/2-2x/3)}]$ as B' and $[Fe_{1/6}W_{1/3}]$ as B'', and found that completely B-site ordered ceramics exhibited a saturation magnetization that is one order of magnitude higher than that of the disordered structure. Another group also found that the magnetic behavior was related to the degree of B-site cation ordering [58], where completely disordered samples displayed antiferromagnetism while ordered samples displayed ferromagnetic behavior. Besides the magnetic properties, the electric properties (such as the dielectric loss) in perovskite oxides are also affected by the degree of B-site cation ordering [52-54].

First-principles calculation is a useful tool to predict the effects of cation ordering on materials properties, such as those in bismuth-based complex perovskite materials [43, 59]. It has been proposed and predicted that $Bi(Fe_{0.5}Cr_{0.5})O_3$ would

display an electrical polarization of 80μC/cm^2 and a saturation magnetization of 1 μ_B/f.u. if Fe^{3+} and Cr^{3+} are ordered to form a double perovskite structure [43]. It would exhibit ferrimagnetic and ferroelectric properties that are superior to those of any known multiferroic materials.

1.8 Objectives

The objectives of the current work are to conduct comprehensive and systematic studies on $BiFe_xMn_{1-x}O_3$ (BFMO) perovskite and to understand the structure-property relationship through a combination of experimental techniques. Due to the excellent properties of the two end members, BFO and BMO, their solid solution was chosen for the present study and BFMO (x=0-0.4) ceramics were synthesized by various methods. Detailed investigation on the dielectric, ferroelectric, and magnetic properties was then conducted. The microstructure of synthesized BFMO ceramics was studied by X-ray diffraction and electron diffraction in order to relate the observed properties to the structure of materials.

1.9 Scope of the work

In Chapter 1, a brief introduction on the multiferroic mechanism in perovskite structure is given in the first part of this chapter. It is followed by a review on recent available literature papers describing the properties of pure and doped $BiFeO_3$, $BiMnO_3$ and their solid solutions.

In Chapter 2, the sample preparation procedures and characterization methods are summarized. Particularly, various characterization techniques such as X-ray diffraction (XRD), scanning electron microscope (SEM), X-ray photoemission

spectroscopy (XPS), Raman spectroscopy, transmission electron microscopy (TEM), and vibrating sample magnetometry (VSM), etc. are briefly introduced.

Chapter 3 presents the main results obtained from the solid solution of BFMO, such as, crystalline phase, microstructure, ferroelectric properties, dielectric properties, impedance spectroscopy, Raman spectroscopy, and oxidation states, etc. The results are discussed in relation to the processing conditions of BFMO ceramics.

Chapter 4 presents the preliminary results of BFO prepared by a novel synthesis method (wet chemical reaction method). The microstructure and physical properties of BFO synthesized by this method are compared with those synthesized by the conventional methods as introduced in Chapter 3.

Chapter 5 summarizes the major findings and conclusions of this work. Future work in this research area is also proposed.

Chapter 2
Experimental Methods and Procedures

2.1 Introduction

The present study involves a number of advanced techniques and facilities for the characterization of ceramics. They include:

1. Structural characterizations of ceramics: X-ray diffraction (XRD), Raman spectroscopy, transmission electron microscopy (TEM), and scanning electron microscopy (SEM).
2. Electrical property characterizations: impedance spectroscopy and ferroelectric *P-E* hysteresis loop measurement.
3. Magnetic property characterization: vibrating sample magnetometry (VSM).
4. Oxidation state characterization: X-ray photoelectron spectrometer (XPS).
5. Thermal analysis: differential scanning calorimeter (DSC).

In this chapter, a brief introduction is given to the above techniques that have been employed in the present work.

2.2 Sample preparations

In this study, $BiFeO_3$ ceramics have been prepared by a conventional mixed oxide solid-state reaction method, a rapid liquid-phase sintering method and a wet chemical method, respectively. $BiFe_{1-x}Mn_xO_3$ (x=0.1-0.4) ceramics were prepared by the rapid liquid-phase sintering method.

The starting raw powders for the solid-state reaction and rapid liquid-phase sintering methods are reagent grade metal oxides which include Bi_2O_3 (99%, International Laboratory, USA), Fe_2O_3 (99.5%, International Laboratory, USA), and MnO_2 (99.9%, International Laboratory, USA). They were weighted according to the stoichiometric compositions of $BiFe_{1-x}Mn_xO_3$ (x=0.0-0.4). They were then mixed in an agate mortar with high-purity ethanol medium and yttrium-stabilized zirconia balls for about 16 hours at 300 rpm. After ball milling, the mixed compounds were dried in an oven at a temperature of over 100°C for 5 hours. For both the conventional solid-state reaction method and the rapid liquid-phase sintering one, the chemical reaction of BFMO is listed below,

$$\frac{1}{2}Bi_2O_3 + \frac{(1-x)}{2}Fe_2O_3 + (x)MnO_2 \rightarrow BiFe_{1-x}Mn_xO_3 + \frac{x}{4}O_2$$

$$x = 0\text{ -}0.4$$

(i) <u>Conventional solid-state reaction method:</u>

After drying, the mixed powders were calcined at 650°C for 2 hours. The calcined powders were wet ball-milled again in alcohol using zirconia balls for 16 hours. After drying, the calcined powders were pressed into pellets by using polyvinyl alcohol (PVA, 10 wt %) as a binder. An uniaxial pressure of ~350 MPa was applied to press the powder into disk samples with a diameter of 12 mm and a thickness of about 1.5 mm. After the burnout of the organic PVA at 650°C for 2 hours with a slow heating and cooling rate of 2°C/min, the green samples were sintered at 800-870°C for 2h with a heating rate of 3°C/min. The samples were cooled down to room temperature with furnace cooling.

(ii) Rapid liquid-phase sintering method:

Following the same procedures as described in the above solid-state reaction method, after the second ball-milling process, the calcined powders were dried and pressed into pellets of 12 mm in diameter and 1.5mm in thickness under an uniaxial pressure of 350 MPa, with a small amount of distilled water as the binder. The green discs were then dehydrated at 100°C for 10h in vacuum. After that, they underwent a rapid liquid-phase sintering process where they were sintered at 860°C for 30 min with a high heating rate of 100°C/s and a fast quenching rate down to room temperature.

(iii) Wet chemical method

The heteronuclear complexes, $Bi[Fe(CN)_6]\cdot nH_2O$ was synthesized at room temperature by mixing nitric acid solutions (2 M/L) with an equimolar amount of

$K_3Fe(CN)_6$ (99+%, International Laboratory, USA) and a stoichiometric amount of $Bi(NO_3)_3 \cdot 5H_2O$ (99+%, International Laboratory, USA). The mixture was kept stirring for 2 hours. The resulting precipitates were collected by suction filtration and then washed with deionized water before drying in air at 50°C. In order to obtain perovskite oxide powders, the complex powders were decomposed at different temperatures for 1 hour. The decomposed powders were then ground and uniaxially pressed into pellets of 12 mm in diameter and 1.5mm in thickness under 350 MPa, with a small amount of distilled water as the binder. Finally, the green pellets were sintered at 800°C for 1 hour with a heating and cooling rate of 10°C/min.

2.3 Structural characterizations

2.3.1 X-ray diffraction (XRD)

The sintered ceramics were ground into powders for the X-ray diffraction (XRD) (Bruker D8 Advance) measurements, where Cu-Kα radiation (λ=0.154 nm) was used and operated at 40 kV and 40 mA. All XRD patterns were recorded under the θ-2θ scanning mode with 2θ scanned from 20 to 80º at a step size of 0.04º and 2s per step.

XRD measurement is a common non-destructive method for characterizing the crystal structure of materials. This technique can be used to analyze the phase structure presented in the materials and the lattice parameters of samples can be determined from XRD spectra. Since each material produces a unique XRD profile, hence, qualitative analysis can be conducted by comparing the XRD pattern to a library of known patterns.

Figure 2.1 shows the schematic diagram of the working principle of XRD. The X-rays diffracted from different crystal lattices interfere with each other and finally produce a diffraction maximum that varies with the scattering angle. From the diagram, the maximum intensity occurs when the path difference AB+BC equals to $2d\sin\theta$ and this leads to the famous Bragg's law,

$$n\lambda = 2d_{hkl}\sin\theta \tag{2.1}$$

where n is an integer, λ is the wavelength of X-ray, d_{hkl} is the lattice spacing between lattice planes (hkl) and θ is the angle between incident beam and (hkl) plane.

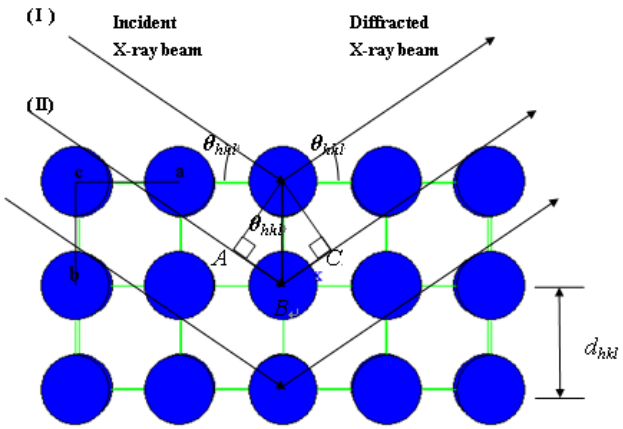

Figure 2.1 Schematic diagram of the working principle of XRD.

2.3.2 Scanning electron microscopy (SEM)

The grain size and uniformity of the synthesized BFMO ceramics were examined by scanning electron microscope (SEM, JEOL 6490). A thin layer of gold film was sputtered on the top surface of a sample before examined by SEM. The SEM is operated by scanning electron beam across a specimen which enables high resolution images of the morphology or topography of a specimen, with great depth of field, at very low or very high magnifications to be obtained. Compositional analysis of such a specimen can also be obtained by analyzing the X-rays produced by the electron-specimen interaction.

2.3.3 Transmission electron microscope (TEM)

Transmission electron microscopy (TEM) is a powerful analytical tool in materials microstructure characterization, where a beam of electrons is transmitted through an ultra thin specimen, interacting with the specimen as it passes through. The transmitted or scattered electron signal is greatly magnified by a series of electromagnetic lenses. The magnified signal may be observed by electron diffraction, conventional imaging (bright-field and/or dark field image), phase-contrast imaging such as high resolution TEM, and convergent beam electron diffraction. Electron diffraction patterns help to determine the crystallographic structure of a material on a fine scale. Amplitude-contrast imaging yields information about the chemistry and microstructure of a material and its defects. Phase-contrast or high-resolution (HR) TEM

imaging gives information about the microstructure of a material and its defects at atomic resolution. The TEM we used is JEOL JEM-2001 with a LaB_6 electron source. The TEM specimens were prepared by grinding and ion milling successively. First, bulk samples were cut into small pieces (3×3 mm^2). The small piece of specimen was then polished to a thickness of 40 μm by a series of abrasive papers. After polishing, the sample was put on a 3-mm-diameter copper supporting grid and thinned further by Ar ion milling. Finally the sample can be thinned down to approximately 50 nm which is sufficiently transparent to electron beams.

2.3.4 Micro-Raman

The Raman spectrometer we used is John-Yvon Horiba HR800 with a blue laser beam (wavelength=488nm) as the source for photon excitations. Diameter of focused beam can be around 100μm.

Raman spectroscopy is a non-invasive technique for the identification of chemical species based on their vibrational modes. It is based on the Raman effect which occurs when laser light is illuminated on the material and scattered. There are three kinds of light scattering in a Raman experiment, i.e., Stokes (longer wavelength), Rayleigh and anti-Stokes scattering, as shown in Figure 2.2. A Raman spectrum is generally composed of several sharp peaks, which are related to the vibrational frequencies. These frequencies can be, in principle, calculated. But in complex molecules, this would be very difficult as various peaks may merge to form complex

bands. By analyzing the vibrational frequencies, each of the chemical bonds in molecules can be identified. These frequencies depend on the masses of atoms in these molecules and on the force constants of inter atomic bonds. These frequencies also depend on the geometrical arrangement of atoms in these molecules. Analysis of the frequency shifts in the spectrum reveals the characteristic vibration frequencies of the atoms and hence the chemical composition and structure of the material.

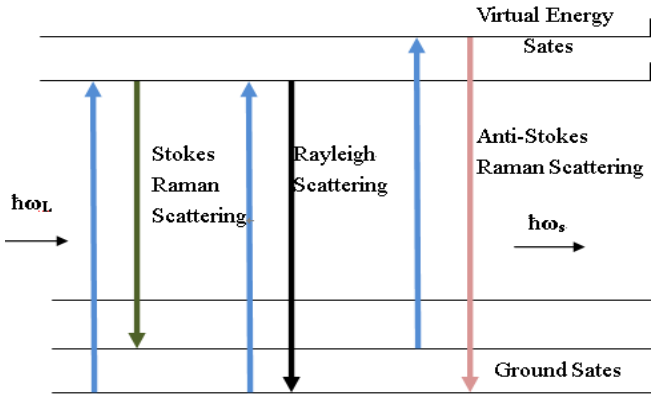

Figure 2.2 Schematic diagram of three kinds of light scattering.

2.3.5 X-ray photoelectron spectrometer (XPS)

In order to identify the composition and the valence state of elements in the samples, the samples were analyzed by X-ray photoelectron spectroscopy (XPS). A monochromatic Al Kα (1486.6eV) X-ray source accompanied with a neutralization gun was used. Correction for the energy shift due to charging effects was made by assuming the C 1s line from adventitious carbon to be at the binding energy of 285.0 eV.

XPS is based on the analysis of electrons escaped from the sample surface (up to 3 nm in depth) by irradiating X-ray beams on the surface. Through the interaction of an X-ray photon with an inner-shell electron of an atom, the energy of the photon can be transferred to the electron and cause the electron to escape from the surface of sample if the energy transferred is large enough. Figure 2.3 shows this photoemission process. An electron at a given electronic level is characterized by its binding energy (E_b) which can be directly determined by using the energy conservation law,

$$E_b = h\nu - E_k - \varphi \tag{2.2}$$

where $h\nu$ is known as the incident photon energy, φ is the work function of a sample, E_k is the measurable kinetic energy of the emitted electron.

XPS spectrum shows the peaks that are directly related to the electronic structure of atoms. The peaks are indexed like the electronic levels from where the photoelectrons are coming. Since each element has a unique binding energy, the XPS spectrum can be used to gives quantitative information on elemental composition of a sample and the chemical state.

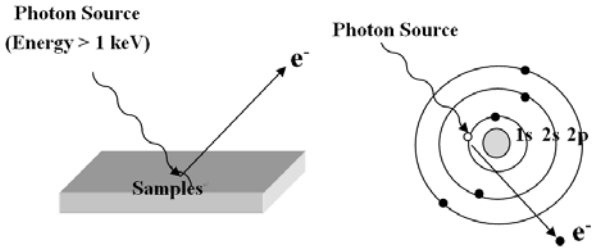

Figure 2.3 Working principle of a photoemission process.

2.3.6 Differential scanning calorimetry (DSC)

DSC (Netzch STA 449C, Jupiter) was used for the thermal analysis. About 10 mg of powder sample was put into a sample crucible with an empty crucible as the reference. The heating rate was 10°C/min and temperature ranged from 25 to 1000°C. In the DSC measurement, the signal was derived from the differential heat supplied to the sample and reference in order to keep the temperature of the two to increase at the same rate. The result was a thermal curve showing the temperature dependent heat capacity of the material, its melting point and phase transition point, etc.

2.4 Electrical and magnetic characterizations

2.4.1 Vibrating sample magnetometer (VSM)

The magnetic properties of the samples were measured by a vibrating sample magnetometer (VSM, LakeShore 7407). Figure 2.4 shows the schematic diagram of a VSM system. It can be used for low temperature measurements down to 4.2 K by using liquid helium cryostat (model 74018). In the measurement, the sample was vibrated with a sinusoidal motion between the poles of an electromagnet. When a known external field H is applied to the vibrating sample with frequency (ω), the change of magnetic flux in the sample induces a voltage in the pickup coils according to the Faraday's law,

$$V = -N\frac{d\Phi}{dt} = -NA\frac{dB}{dt} = -NA\mu_0\frac{d}{dt}(H + M) \quad (2.3)$$

where Φ=BA is the flux passing through the coils, A is the area of coils, N is the number of coils, V is the induction voltage, B is the magnetic field of the sample, μ_0 is the vacuum permeability, M=χH is the magnetization, and χ is the magnetic susceptibility of the sample.

By using a reference sample to calibrate VSM, the output voltage can be directly converted into absolute value of the magnetic moment of the sample.

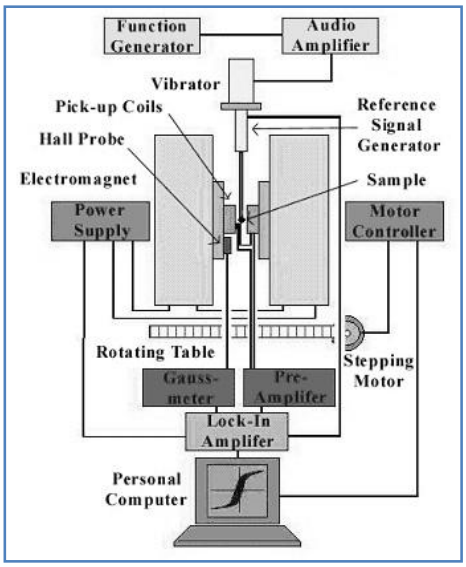

Figure 2.4 Schematic diagram of VSM.

2.4.2 Polarization-electric field (*P-E*) hysteresis loop

Ferroelectric hysteresis loops of the ceramics were measured by a modified Sawyer-Tower circuit. The experimental setup is shown in Figure 2.5, which includes a function generator (HP 8116A), a voltage amplifier (Trek 609D-6) and a digital oscilloscope (HP 5465A). The applied *ac* electric field was under a frequency of 100 Hz.

In the measurement circuit, the reference capacitance was about 1000 times larger than the sample capacitance, which ensured almost the full application of electric voltage across the sample. By measuring the voltage across the reference capacitor, the amount of polarization charge and the polarization of the sample can be calculated by,

$$Q = V_{(ref)}C_{(ref)} \tag{2.5}$$

$$P = \frac{Q}{A} \tag{2.6}$$

where $V_{(ref)}$ is the voltage across the reference capacitor, $C_{(ref)}$ is the capacitance of the reference capacitor, A is the area of electrode on the sample, and Q and P are the polarization charge and the electric polarization of the sample, respectively.

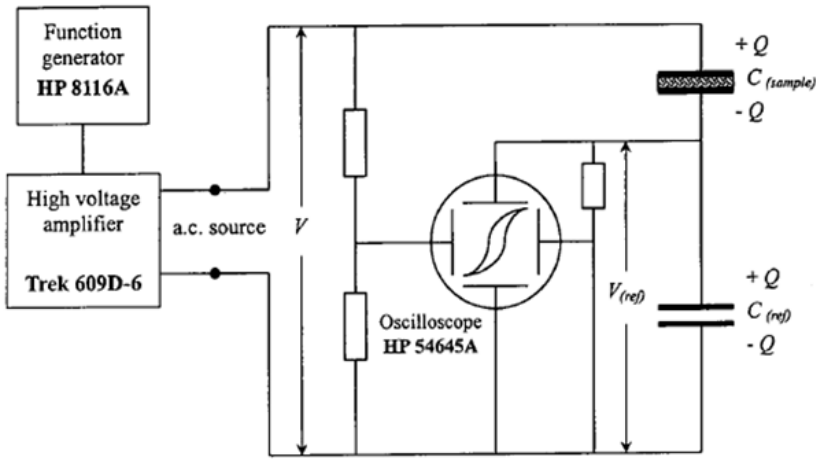

Figure 2.5 Experimental setup for the *P-E* hysteresis loop measurement.

2.4.3 Dielectric measurements

The temperature and frequency dependence of the dielectric properties of the ceramic samples, including the relative permittivity (ε_r) and dielectric loss (tanδ), were measured by a broadband dielectric spectrometer (Novocontrol Aplha-analyzer, Germany). The measuring frequency was varied from 10 Hz to 10 MHz. The temperature of the sample was controlled by a Lakeshore 331 Temperature Controller and was varied from -100 to 100°C. The data were automatically collected every 10°C.

Before dielectric measurements, the disc samples were polished into 0.7 mm in thickness. Gold electrodes were then sputtered onto the top and bottom surfaces of the cylinder shaped ceramic samples for 4 minutes for each surface, using a sputter coater (Edwards Coating System). The same method was also applied to the preparation of electrodes for *P-E* hysteresis loop measurement.

The relative permittivity was calculated from the sample capacitance using $C = \frac{\varepsilon_r \varepsilon_0 A}{d}$, where ε_0 is the vacuum permittivity (8.85×10^{-12} F/m), C is the measured sample capacitance, d is the thickness of sample and A is the area of electrode.

Chapter 3
Structural and Physical Properties of $BiFe_{1-x}Mn_xO_3$

3.1 Introduction

In this Chapter, the results on various structural and physical properties of BFMO ceramics are presented and discussed. Firstly, the crystalline structure of the BFMO solid solution was studied. Main focus was laid on ceramic samples synthesized by solid-state reaction and rapid liquid-phase sintering methods. Secondly, the microstructure of sintered ceramic samples was investigated by SEM and TEM. Thirdly, physical properties such as the dielectric, ferroelectric, and magnetic properties were analyzed. Finally, the lattice vibration modes of the samples and the valence states of some elements were studied.

3.2 Crystalline structure

XRD was used to study the phase information of sintered ceramic samples. The XRD patterns of BFO ceramics synthesized by the conventional solid-state reaction method at different temperatures are shown in Figure 3.1. Similar to previous studies [60, 61], it was hard to obtain high purity BFO by the conventional solid-state reaction method. As can be seen from the XRD patterns, major secondary phases such as $Bi_2Fe_4O_9$ and $Bi_{12}(Bi_{0.5}Fe_{0.5})O_{19.5}$, still remained in the sintered samples. These secondary phases could not be removed even after several intermittent grindings and calcinations before the sample was finally sintered. Generally, more secondary phases would be generated at higher sintering temperatures, while the ceramics were difficult to sinter at lower sintering temperatures. The results imply that the temperature window for stable BFO is quite narrow.

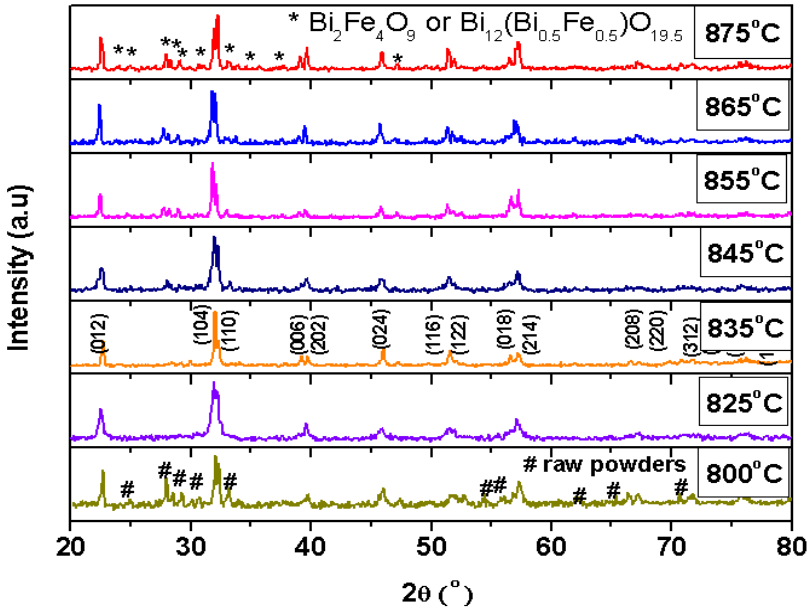

Figure 3.1 XRD patterns of $BiFeO_3$ ceramic synthesized by conventional solid-state reaction method at different sintering temperatures.

In order to obtain single phase BFO and its solid solution with BMO, the rapid liquid-phase sintering method was tried. This was because that the sintering time was short enough during the rapid liquid-phase sintering process to reduce the loss of Bi_2O_3 and the cooling rate was high enough to freeze the metastable single phase before it was decomposed [15, 61]. The XRD patterns of BFMO synthesized by this method are shown in Figure 3.2. No obvious secondary phases can be identified. All the diffraction peaks can be indexed according to a hexagonal structure (*R*3*c*). As the content of Mn is increased, a noticeable change in lattice parameters can be observed. This suggests that Mn ions may have entered into the lattice of BFO to form a solid solution with it. Figure 3.2 (c) shows the enlarged XRD patterns around the 2θ of 32°. Two diffraction peaks

(104) and (110) are clearly separated in pure BFO. With increasing Mn content, these two peaks gradually merge into a single one and, at the same time, they shift accordingly. Similar changes can also be observed in (006), (202), (018), (214), (116) and (122) diffraction peaks as shown in Figure 3.2 (b). Moreover, several diffraction peaks such as (012) and (024) are broadened with increasing Mn content as shown in Figure 3.2 (d). This can be explained by anisotropic strains developed in the BFO lattice as Mn content is increased [26]. The ceramic has a tendency to reduce its rhombohedral distortion and to transform into a non-rhombohedral (tetragonal) structure with increasing Mn content.

The lattice parameters of a hexagonal structure can be calculated by,

$$\frac{1}{d^2}=\frac{4}{3a_h^2}(h^2+hk+k^2)+\frac{1}{c_h^2}l^2 \tag{3.1}$$

where d is the spacing between neighboring (hkl) planes, and a_h and c_h are the lattice parameters in the hexagonal structure.

Sometimes, it is more convenient to use a rhombohedral unit cell. The lattice parameters of a hexagonal structure can be converted into those of a rhombohedral one by the following equations,

$$a_r=\frac{1}{3}\sqrt{3a_h^2+(\frac{c_h}{2})^2} \text{ and } \sin\frac{\alpha_r}{2}=\frac{3}{2\sqrt{3+(\frac{c_h}{2a_h})^2}} \tag{3.2}$$

where a_r and α_r are the lattice parameters in the rhombohedral structure.

The lattice parameters of BFMO were calculated by assuming a rhombohedral

structure for BFMO with x=0–0.3 and a tetragonal structure for x=0.4. The composition dependence of the lattice parameters are summarized in Table 3. 1 and Figure 3.3. The lattice parameters are found to decrease with increasing x and so does the unit cell volume, which agrees well with other reported work [26, 35]. Based on the present results and Raman spectrum (shown later in section 3.8), the substitution of high spin Mn^{3+} (d^4) is expected to cause additional octahedral deformation in a structure which already contains highly deformed FeO_6 octahedra [62] since Mn^{3+} is a Jahn-Teller active ion to cause local Jahn-Teller distortions [63, 64].

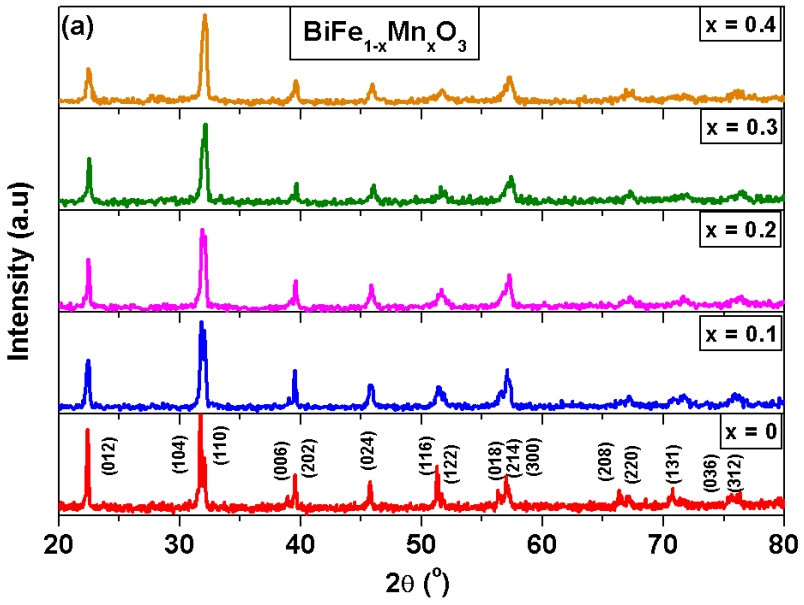

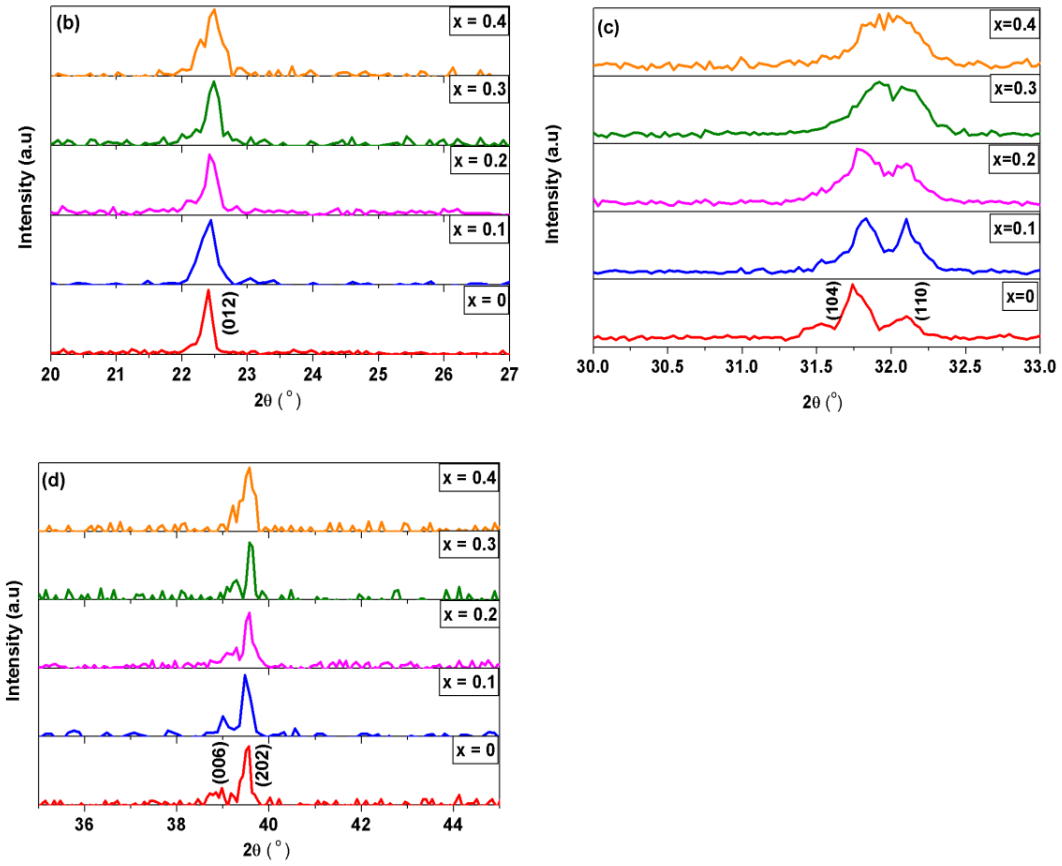

Figure 3.2 XRD patterns of BFMO (x=0–0.4) bulk ceramics synthesized by rapid liquid-phase sintering at 860°C for 30 min with 2θ ranged from (a) 20 to 80°, (b) 20 to 27°, (c) 30 to 33° and (d) 35 to 45°.

Mn contents (x)	a (Å)	α (◦)	c(Å)	V (Å^3)
0	3.9619	89.429	--	62.18
0.1	3.9561	89.648	--	61.91
0.2	3.9508	89.469	--	61.66
0.3	3.9449	89.687	--	61.39
0.4	3.9372	--	3.9548	61.31

Table 3. 1 Composition dependence of the lattice parameters of BFMO (x =0–0.4).

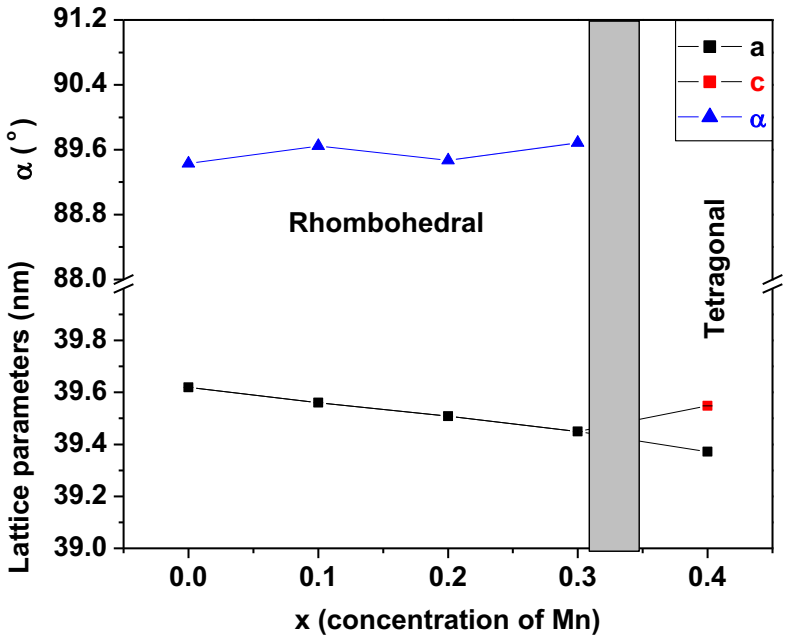

Figure 3.3 Composition dependence of the lattice parameters of BFMO (x=0–0.4).

3.3 Microstructure analysis by SEM

Figure 3.4 (a) – (d) show the SEM images of the surface morphologies of BFMO ceramics (x=0–0.4) which were prepared by rapid liquid-phase sintering technique. It can be seen that BFO has a large amount of porosities and exhibits an abnormal grain structure, similar to those reported for BFO ceramics prepared by other researchers [65-67]. However, for Mn doped BFO samples, a normal grain growth can be found and well defined grains and grain boundaries can be clearly seen. It is believed that the addition of Mn suppresses the formation of liquid phase during the sintering process, although a small amount of liquid phase can still be found around the grain boundaries. The average grain size of BFMO (x=0.1 and 0.2) is around 1.5 to 2 μm, while that of BFMO (x=0.3 and 0.4) increases to 2 to 3.5 μm. It seems that the doping of Mn promotes the grain growth.

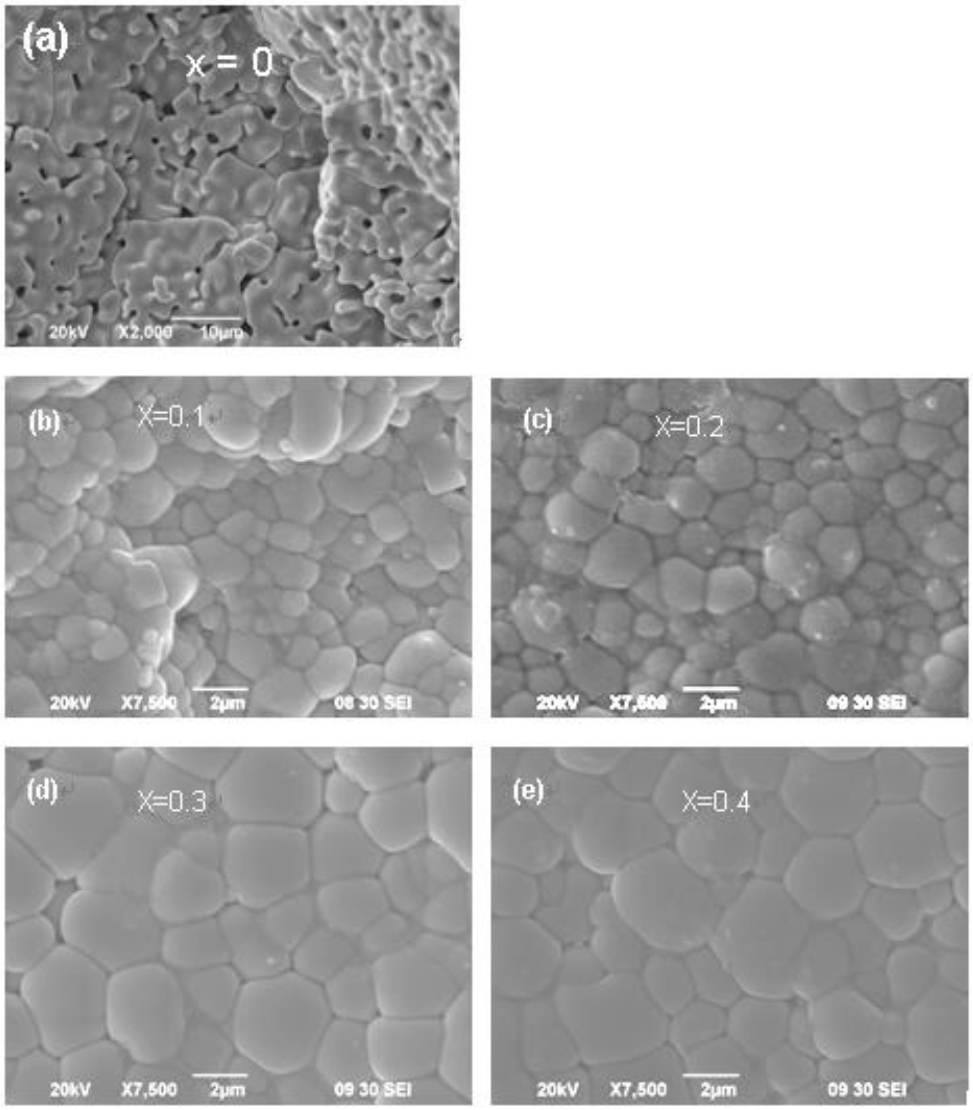

Figure 3.4 SEM micrographs of BFMO sintered at 860°C by rapid liquid-phase sintering: (a) x=0; (b) x=0.1; (c) x=0.2; (d) x=0.3 and (e) x=0.4.

3.4 Ferroelectric properties

3.4.1 *P-E* loop measurement

Figure 3.5 shows the room temperature ferroelectric *P-E* hysteresis loops of BFO ceramics which were synthesized by solid-state reaction and rapid liquid-phase sintering, respectively. For the sample synthesized by the solid-state reaction with a slow heating and cooling rate as described in Chapter 2, a very slim polarization with P_{max} around 3.5 $\mu C/cm^2$ (even under a very high *E*-field of 150 kV/cm) can be observed. In contrast, the samples synthesized by the rapid liquid-phase sintering show quite different ferroelectric properties as shown in Figure 3.5 (b) and (c). For the sample sintered with a heating rate of 40°C/min, an antiferroelectric-like hysteresis loop can be observed, which is related to the aging effect of ferroelectric ceramics [68-71]. For the sample sintered with a heating rate of 100°C/s, a much higher remnant polarization P_r and saturation polarization P_{max} of 7.5 and 15 $\mu C/cm^2$, respectively, can be observed.

From the above results, it is clear that the ferroelectric properties of BFO are very sensitive to the synthesis conditions. Although all BFMO (x=0.1–0.4) ceramic samples were synthesized by the rapid liquid-phase sintering method, they exhibited a high leakage current that made it impossible to measure the *P-E* hysteresis loop. The reason for this high leakage current is due to the electric conduction arising from polaron hopping motion and will be discussed in section 3.6.

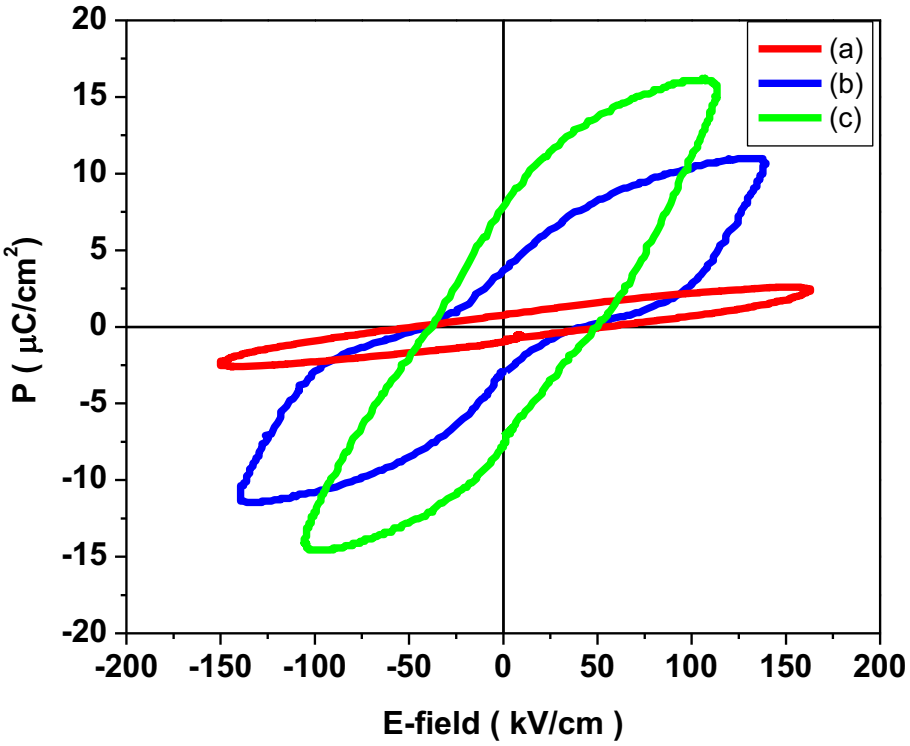

Figure 3.5 Room temperature *P-E* hysteresis loops of BFO ceramics synthesized by different methods: (a) conventional solid-state reaction, (b) rapid liquid-phase sintering with a heating rate of 40°C/min, and (c) rapid liquid phase sintering with a heating rate of 100°C/s.

3.4.2 Transition temperature

The phase transition temperature can be determined by DSC measurements. Figure 3.6 shows the DSC curves of BFO ceramic powders and two peaks can be observed. The endothermic peak at 835°C corresponds to the Curie temperature (T_C) and the exothermic peak at 372°C is the Neel temperature (T_N), both of which agree well with the reported values [15]. As Mn was doped into BFO, the Curie temperature T_C was

observed to decrease with increasing Mn concentration as shown in Figure 3.7. T_C of the BFMO system decreased from 835°C for BFO to 625°C for BFMO (x=0.4). The decrease in T_C shows clearly a linear dependence on the concentration of Mn as illustrated in Figure 3.9. This indicates that Mn has entered into the BFO lattice and a solid solution has been formed between BFO and BMO. The decrease in T_N also exhibits a linear dependence on the concentration of Mn as illustrated in Figure 3.9. For BFMO (x=0.4), the signal corresponding to T_N is too weak to be identified from the DSC curves. This may be due to the small enthalpy change associated with magnetic transition in Mn doped samples. Hence the thermal spectra cannot display a sharp thermal transition at T_N.

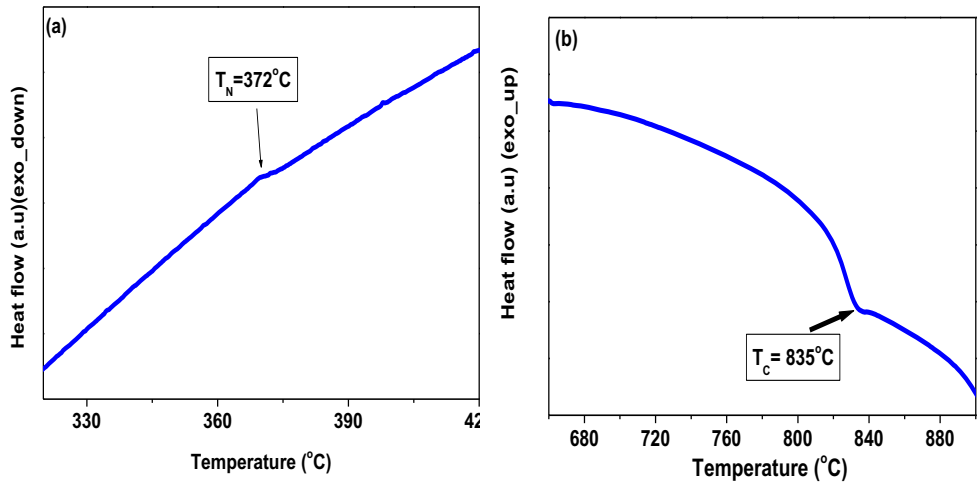

Figure 3.6 DSC curves during the heating of BFO powders in the temperature range of (a) 300–420°C and (b) 650–890°C.

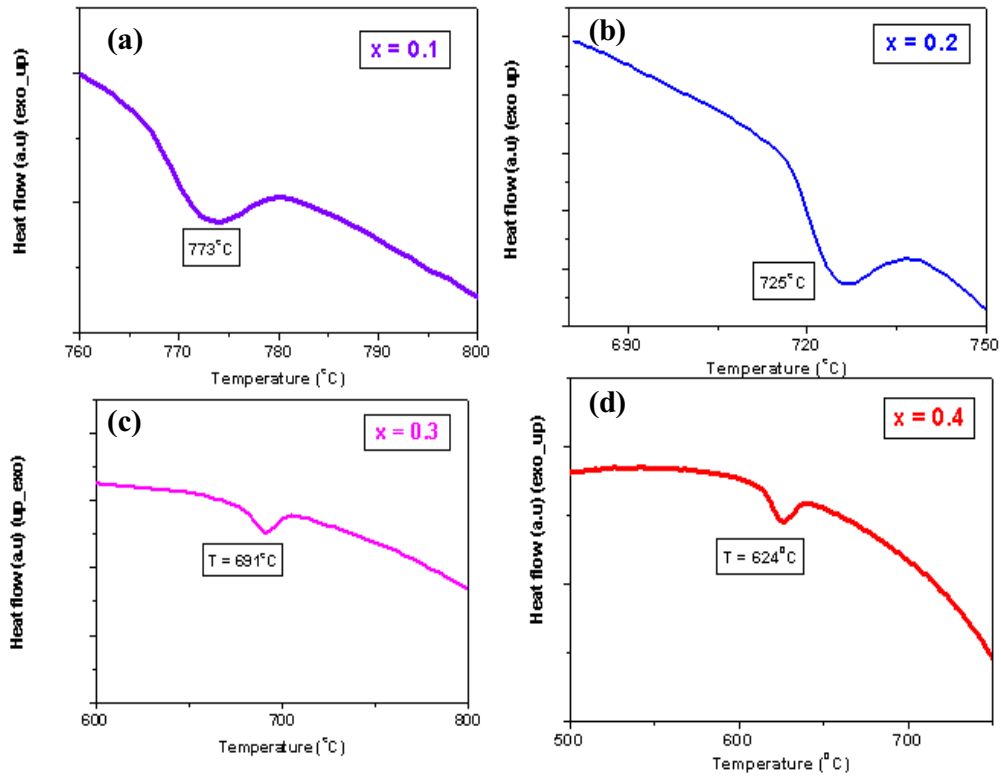

Figure 3.7 DSC curves during the heating of BFMO powders with different Mn content above 500°C: (a) x=0.1; (b) x=0.2; (c) x=0.3; and (d) x=0.4.

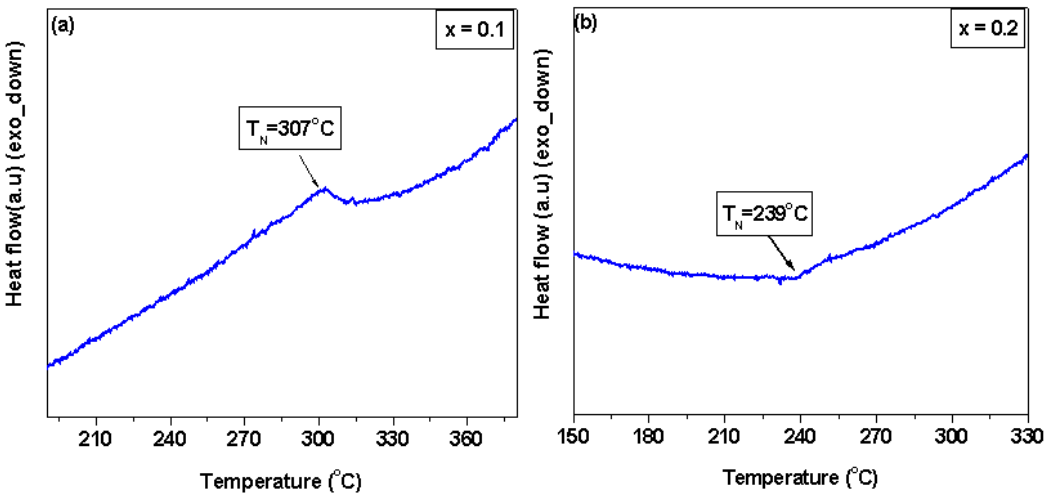

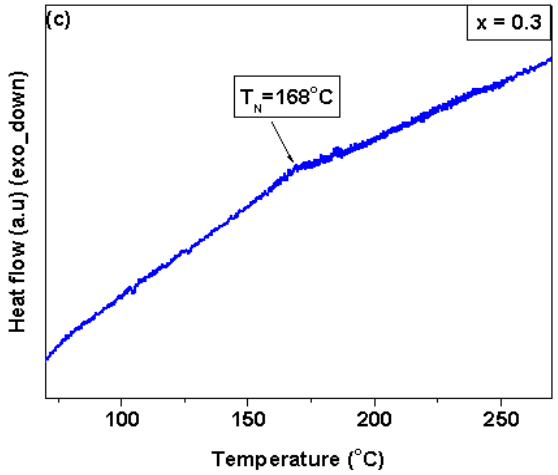

Figure 3.8 DSC curves during the heating of BFMO powders with different Mn content below 500°C: (a) x=0.1; (b) x=0.2; and (c) x=0.3.

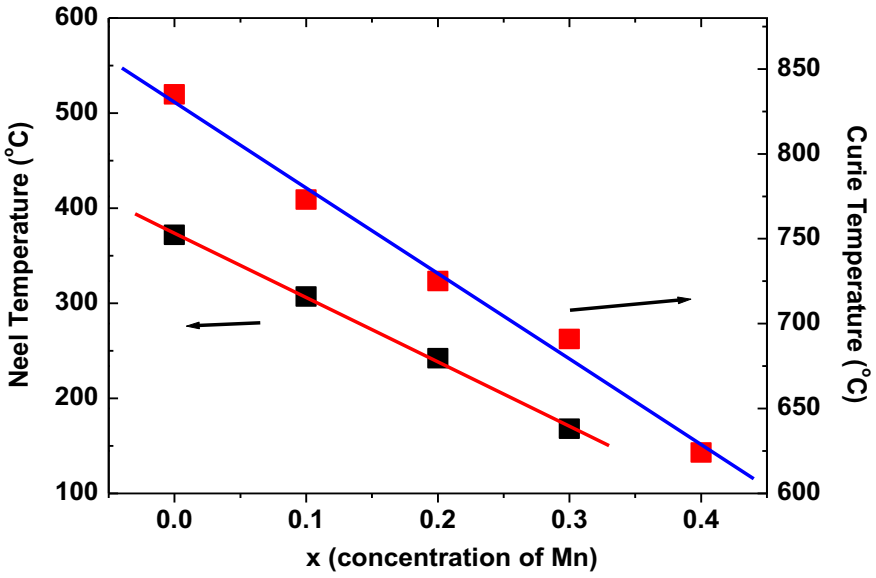

Figure 3.9 Curie and Neel temperatures as a function of the concentration (x) of Mn in BFMO system.

3.5 TEM analysis

The microstructure of BFMO (x=0–0.4) ceramics synthesized by the rapid liquid-phase sintering was characterized by TEM including the selected area diffraction patterns (SADP) and high resolution transmission electron microscopy (HRTEM). For simplicity in the indexing of SADP, crystalline BFMO was represented by its parent pseudo-cubic perovskite structure. In the analysis of the SADPs, the diffraction planes were indexed according to a series of R (the distance between the central spot and the other diffraction spots) and θ values (the angle between lines joining the central spot to each diffraction spot). The d-spacing between a set of parallel planes can be calculated by the basic formula, $Rd=L\lambda$ where $L\lambda$ is the camera constant (10.4 $Åcm^{-1}$ in the present study).

SADPs of pure BFO ceramics recorded along $[110]_p$, $[1\text{-}10]_p$, $[111]_p$ and $[100]_p$ (suffix p refers to the pseudo-cubic structure) zone axes are shown in Figure 3.10 (a – d) , respectively. ½<111> superlattice reflections can be found in the SADP along $[110]_p$ zone axis [as circled in Figure 3.10 (a)], while they are absent along $[1\text{-}10]_p$ zone axis [Figure 3.10(b)]. These superlattice reflections arise from the antiphase rotations of FeO_6 octahedra in the perovskite structure since these oxygen octahedra are corner linked throughout the lattice and form a relatively rigid framework. The titling of one octahedron around the principle axis will cause the antiparallel titling of all the neighboring octahedra lying in the same plane perpendicular to that axis. This doubles the unit cell and results in superlattice reflections. To confirm this, the software CaRIne

Crystallography 3.1 was used to simulate the diffraction patterns in different zone axes, which are shown in Figure 3.11 It can be seen that the <110>-type zone axes are no longer equivalent. If the zone axis is $[110]_p$, the ½<111> superlattice reflections can be observed. When the zone axis is $[1\text{-}10]_p$ which is perpendicular to the axis of antiphase octahedral rotation, the ½<111> superlattice reflections cannot be observed. The same have been observed and discussed in details for other materials with the rhombohedral symmetry [10, 72, 73].

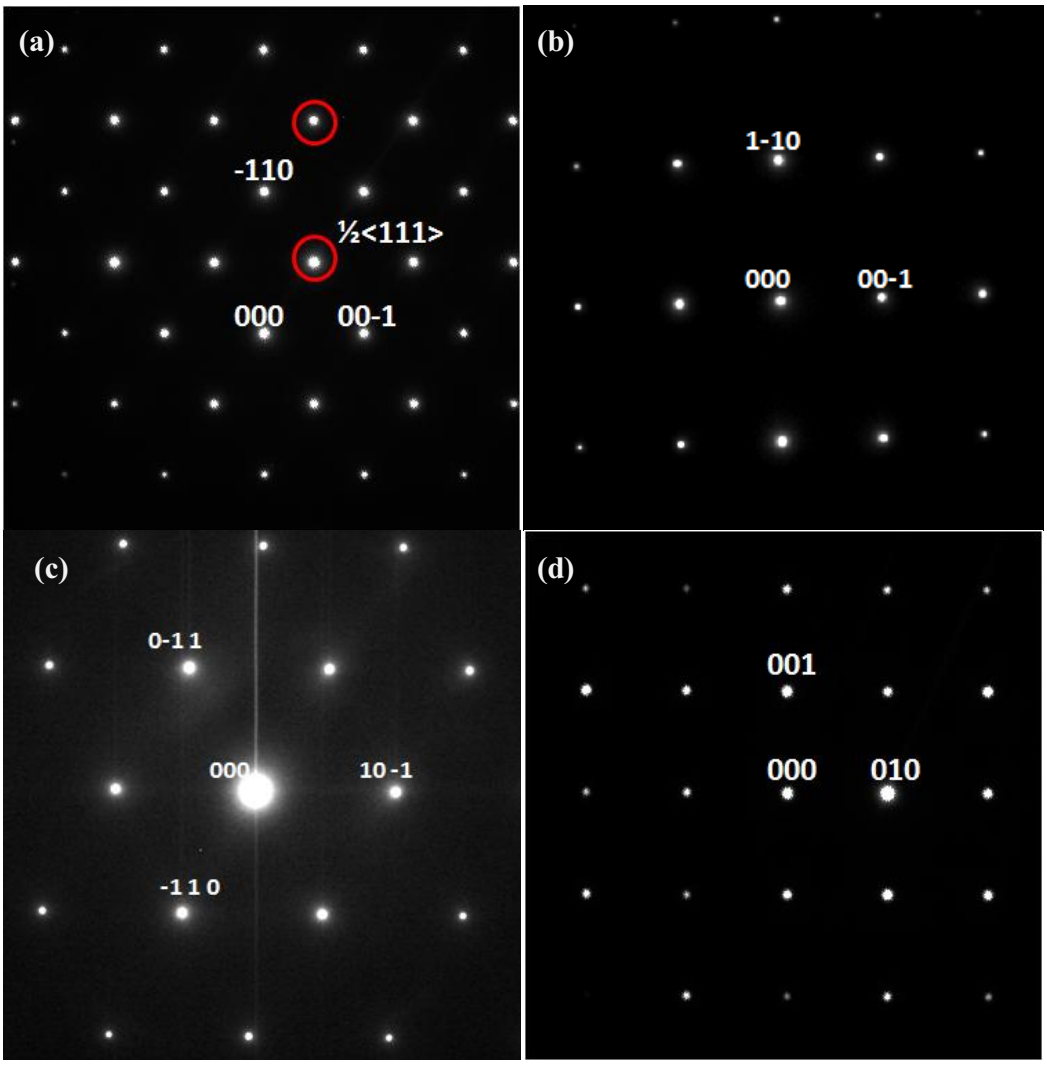

Figure 3.10 SADPs of BFO along different zone axes: (a) $[110]_p$, (b) $[1\text{-}10]_p$, (c) $[111]_p$ and (d) $[100]_p$. Superlattice reflections arising from antiphase tilting are circled.

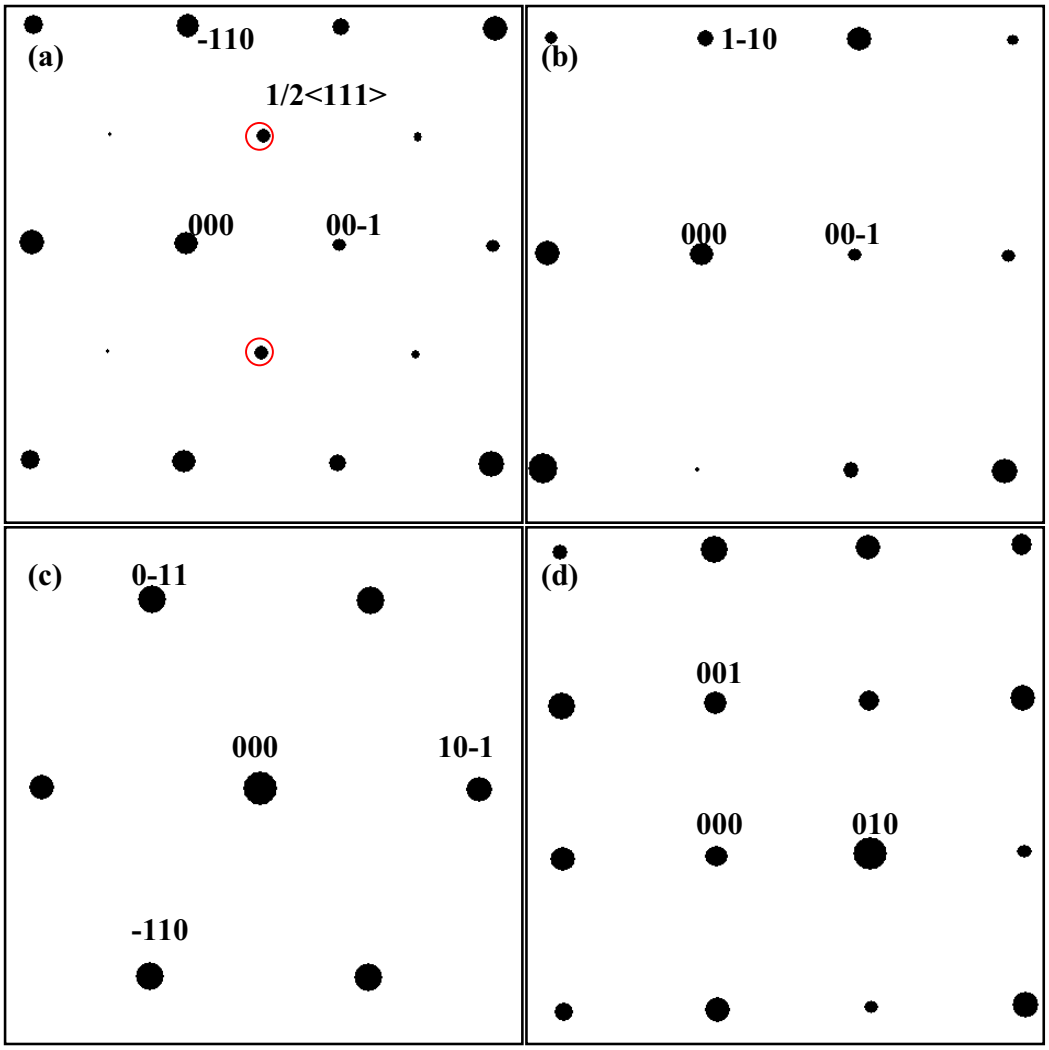

Figure 3.11 Diffraction patterns of BFO along different zone axes simulated by CaRIne Crystallography 3.1: (a) $[110]_p$, (b) $[1\text{-}10]_p$, (c) $[111]_p$, and (d) $[100]_p$. The structural parameters of BFO used in the simulation were from Sosnowska *et al.*[74].

The characteristic SADPs along $[110]_p$, $[111]_p$ and $[100]_p$ zone axes of BFMO (x=0.1–0.4) ceramics synthesized by rapid liquid-phase sintering are illustrated in Figure 3.12 – 14. From Figure 3.12, the ½<111> superlattice reflections which are associated with the antiphase rotations of FeO_6 octahedra can be clearly observed in samples with x=0.1–0.3 but absent for x=0.4. This implies that the unit-cell doubling induced by the antiphase octahedral rotation is gradually destroyed by the addition of Mn. It is interesting to note that BFMO (x=0.1) and BFO have the same diffraction patterns in all the zone axes taken. This indicates that the doping of 10 mol% Mn did not change the structural symmetry of BFO. However, when 20 mol% Mn was doped, extra diffraction spots appeared as shown in Figure 3.13(b) and Figure 3.14(b). For BFMO (x=0.3 and 0.4), a 4-fold periodicity along the $[01\text{-}1]_p$-type direction can be found in the SADPs along $[111]_p$ and $[100]_p$ zone axes as shown in Figure 3.13(c-d) – 14(c-d). Besides, the diffraction patterns of BFMO (x=0.4) are quite different from that of BFMO (x=0.1–0.3).

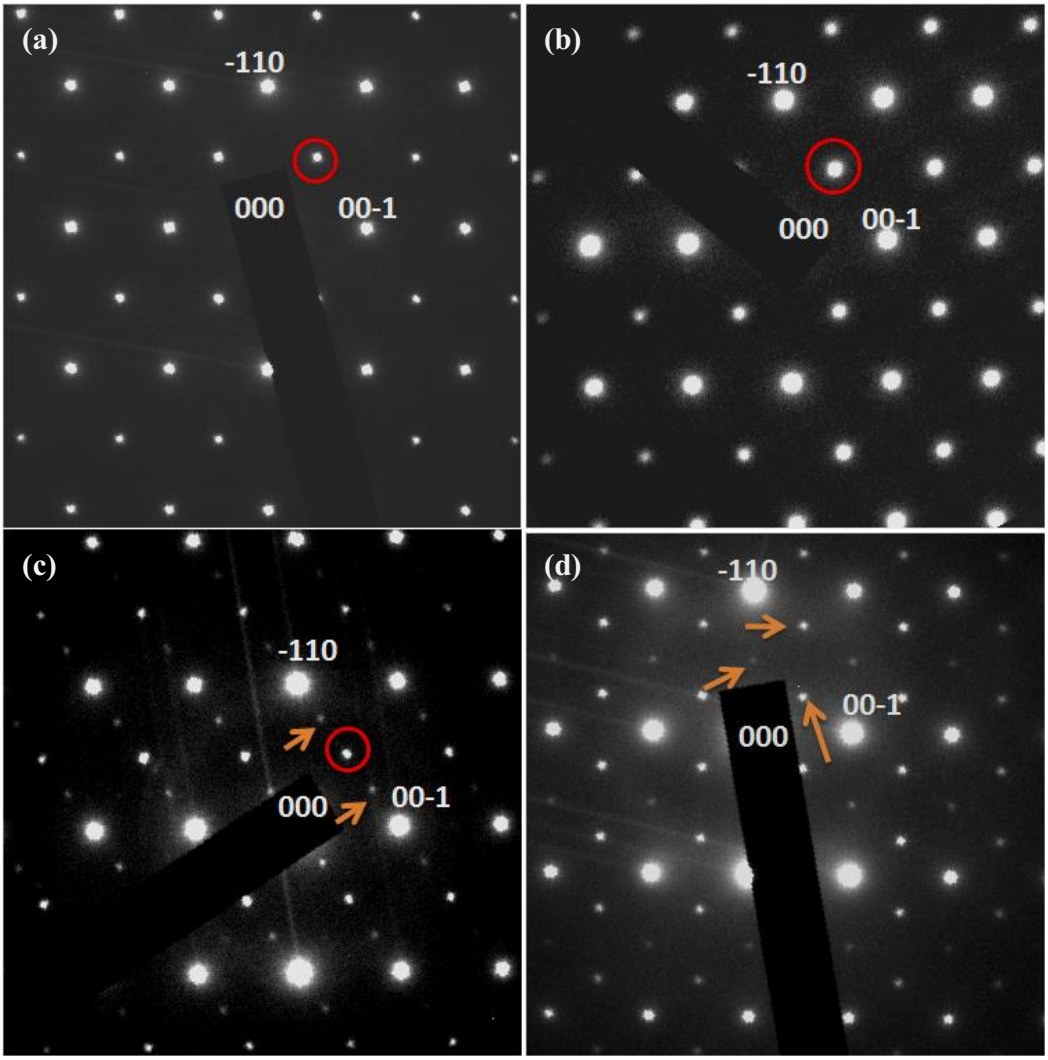

Figure 3.12 SADPs along $[110]_p$ zone axis of BFMO: (a) x=0.1, (b) x=0.2, (c) x=0.3, and (d) x=0.4. ½<111> superlattice reflections associated with antiphase tilting are circled. Extra diffraction spots are arrowed.

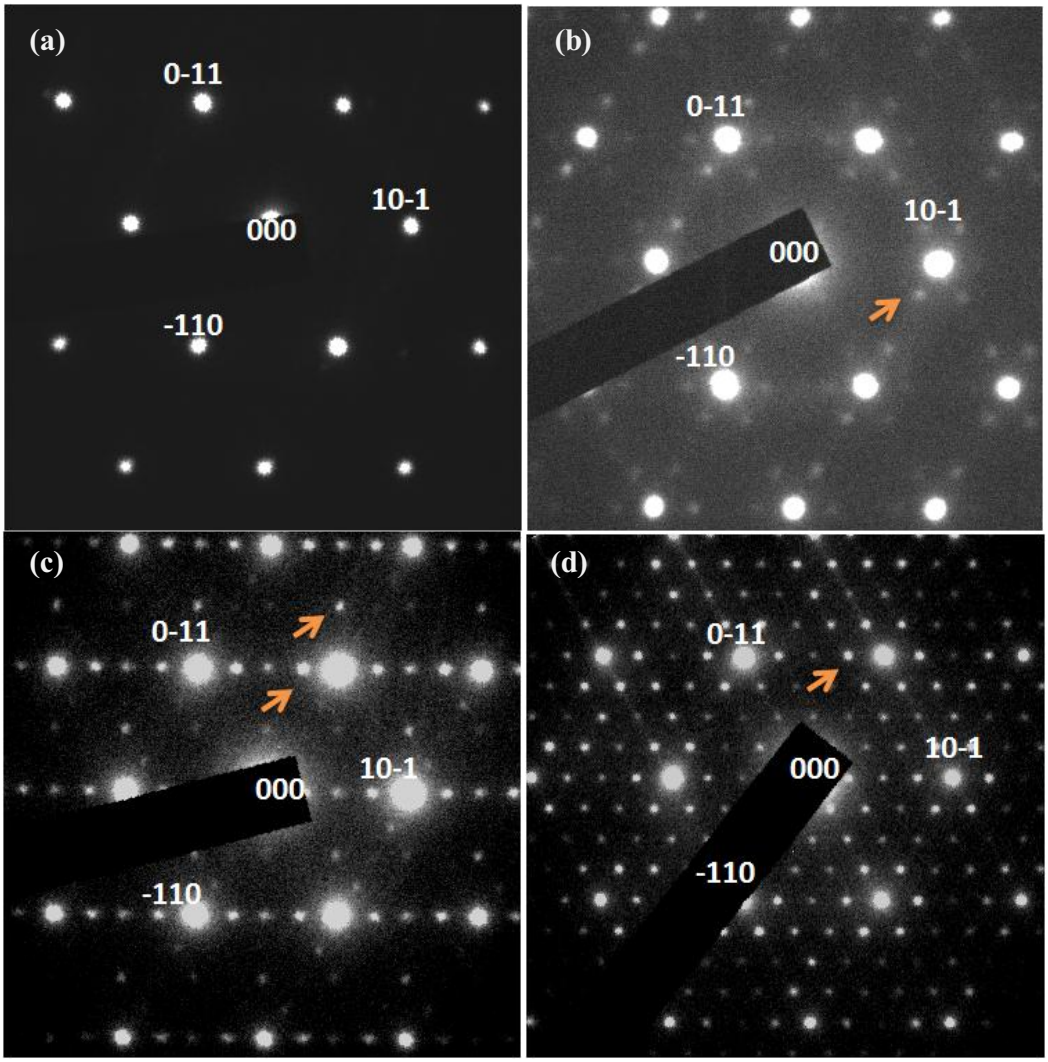

Figure 3.13 SADPs along $[111]_p$ zone axis of BFMO: (a) x=0.1, (b) x=0.2, (c) x=0.3, and (d) x=0.4. Superlattice reflections are arrowed.

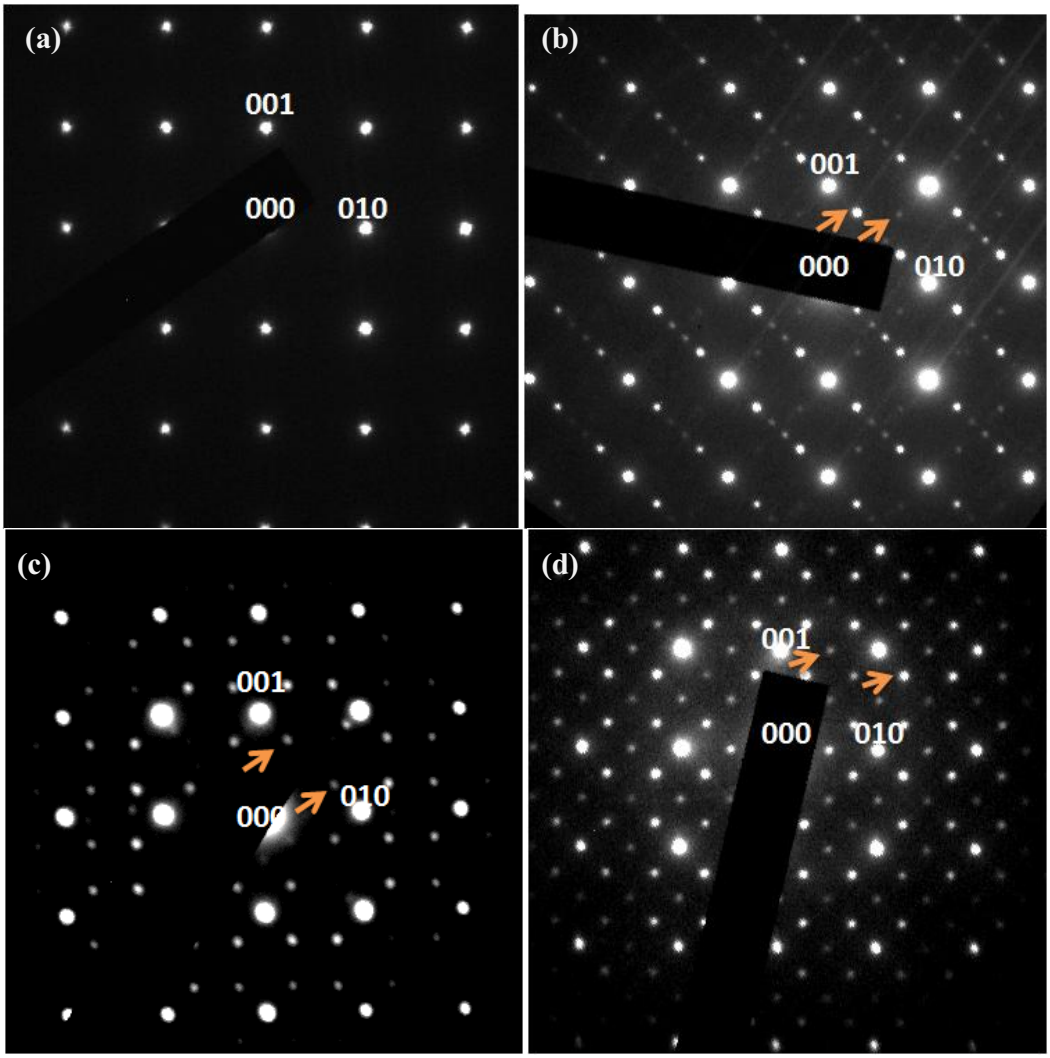

Figure 3.14 SADPs along $[100]_p$ zone axis of BFMO: (a) x=0.1, (b) x=0.2, (c) x=0.3, and (d) x=0.4. Superlattice reflections are arrowed.

To understand the SADPs seen from the BFMO (x=0.4) sample, a structural model was proposed. We assume that there are two sets of periodic sequence: one is the fundamental diffraction spots corresponding to the pseudocubic structure with a_p=3.96 Å and the other is the ¼<111>-type superlattice spots with $4a_p$=15.84 Å in the pseudocubic structure. The reciprocal lattice of this structure is reconstructed and shown in Figure 3.15 based on the electron diffraction patterns. In real space, the ideal structure model is shown in Figure 3.16. In this model, a supercell of $4a_p \times 4a_p \times 4a_p$ is constructed with Mn ions forming a body-centered cubic lattice. Such an ordered structure cannot be found in pure BFO sample and its simulated diffraction patterns along $[111]_p$ and $[100]_p$ zone axes (as shown in Figure 3.17) are similar to those observed experimentally. In should be noted that such ¼<111>-type superlattice reflections may also be resulted from the ordering of oxygen vacancies as observed in pure BMO [75, 76], which can only be observed after prolonged irradiation of electron beams. While in our sample, those superlattice spots appeared at the first time when we looked at the sample. Moreover, as later shown by the XPS spectra, the concentration of Fe^{2+} did not vary with the Mn doping level, the oxygen vacancy concentration does not vary too much with Mn and hence the sudden appearance ¼<111>-type superlattice reflections in BFMO (x=0.4) sample may not arise from the ordering of oxygen vacancy. There are also other possibilities that can generate the ¼<111> superlattice reflections, such as the twinning and antiphase boundaries. However, our preliminary HRTEM pictures shown in Figure 3.18 cannot tell such intrinsic defects inside the grains. The EDX point analysis was performed on grains and grain boundaries and no significant variation in the

concentration of Mn and Fe ions can be detected. Therefore, intrinsic defects such as the twinning and antiphase boundaries are unlikely be the cause of ¼<111> superlattice reflections. However, detailed investigation in the microstructure is still required for a clearer understanding of the superstructure. Such investigation may have to use a combination of techniques including clearer HRTEM pictures and simulations, EELS analysis on composition and valence, EDX analysis on composition, and SADP and simulations, etc., that are taken from samples with different processing conditions (including annealing in different atmospheres).

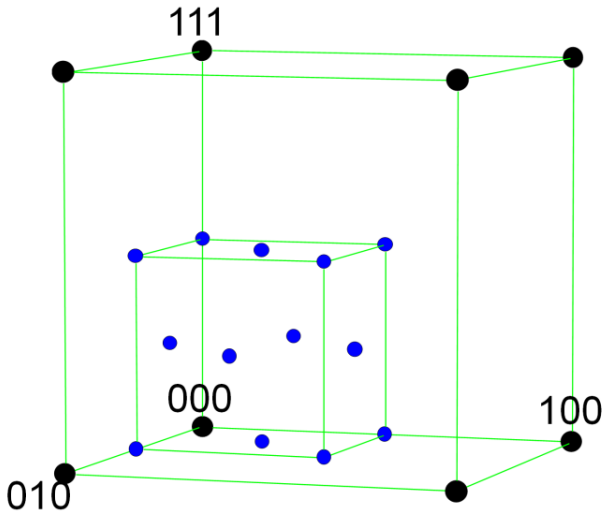

Figure 3.15 Part of the reciprocal lattice reconstructed from the diffraction pattern of BFMO (x=0.4).

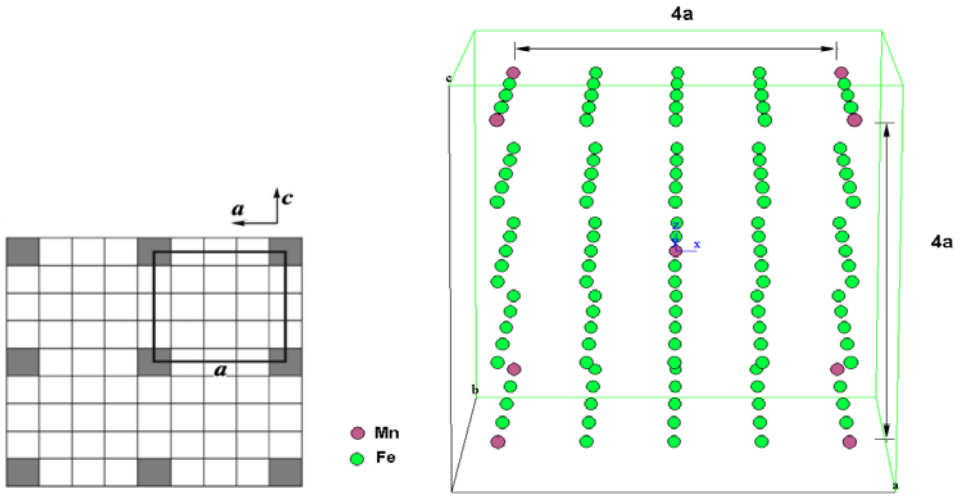

Figure 3.16 The idealized structural model for BFMO (x=0.4) with B site cation ordering in real space.

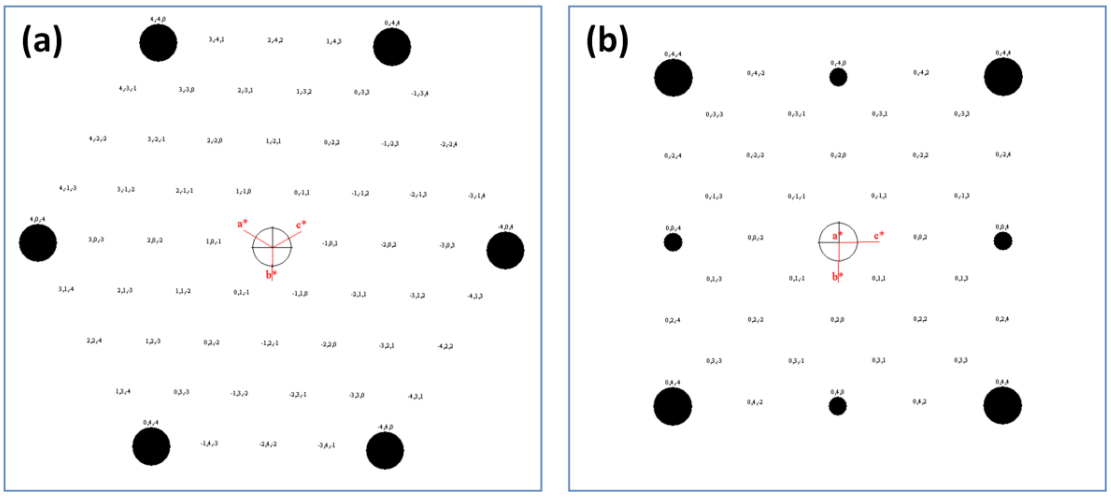

Figure 3.17 Diffraction patterns of the ideal model simulated by CaRIne Crystallography 3.1 along zone axes (a) $[111]_p$ and (d) $[100]_p$, respectively.

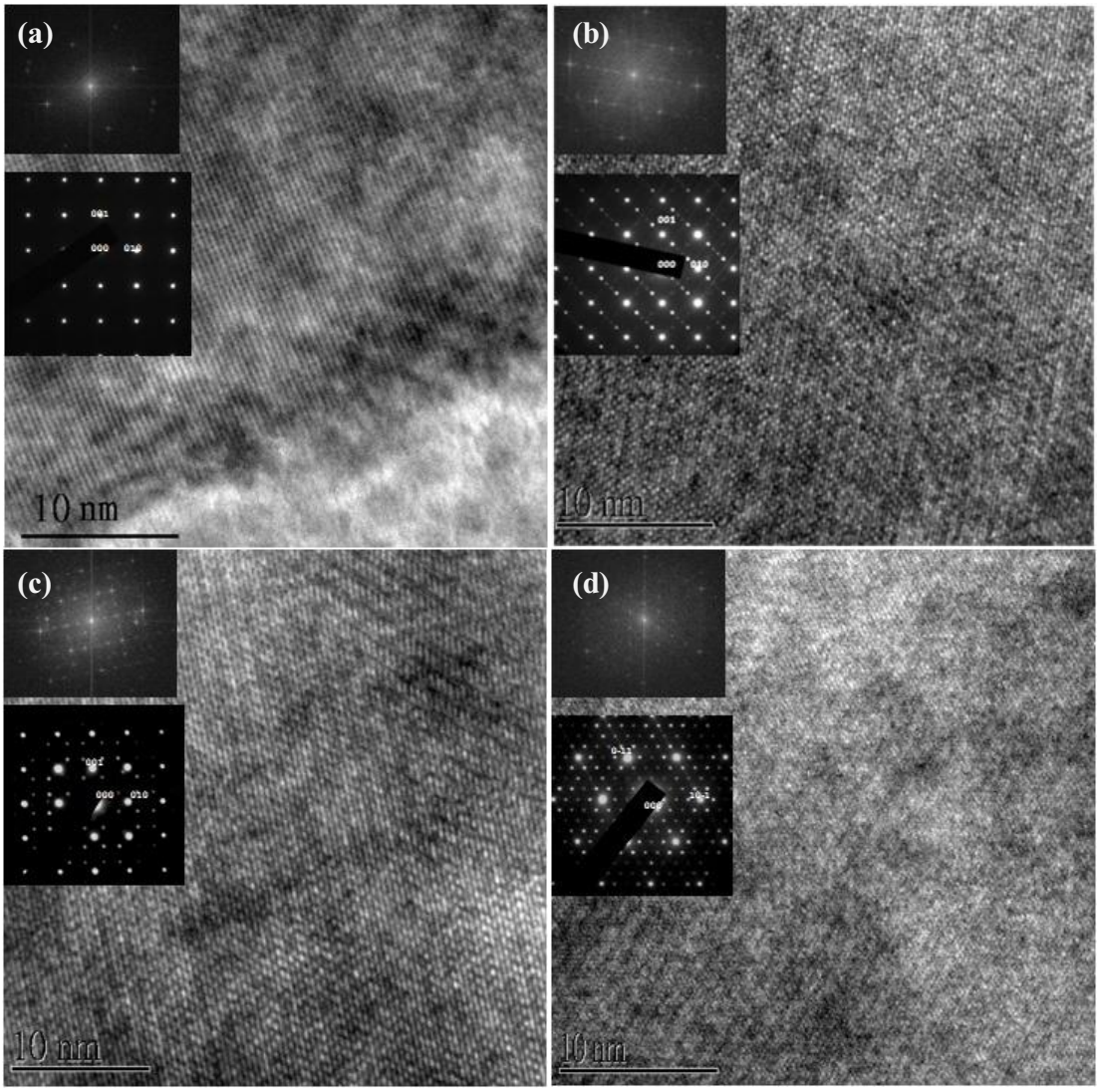

Figure 3.18 HRTEM image of BFMO: (a) x=0.1, (b) x=0.2, (c) x=0.3, and (d) x=0.4. (Inset) Fast Fourier transformtion (FFT) and SADPs of the corrosponding HRTEM image.

3.6 Dielectric measurement

To study the dielectric properties of the synthesized ceramics, temperature and frequency dependent dielectric measurements were conducted. The relative dielectric permittivity can be expressed in a complex form,

$$\varepsilon_r(\omega) = \varepsilon_r'(\omega) - i\varepsilon_r''(\omega) \tag{3.3}$$

where $\varepsilon_r'(\omega)$ and $\varepsilon_r''(\omega)$ are the real and imaginary parts of the relative dielectric permittivity, respectively. The dielectric loss ($\tan\delta$) is given by

$$\tan\delta = \frac{\varepsilon_r''}{\varepsilon_r'} \tag{3.4}$$

Figure 3.19 shows the temperature dependence of the real part of the complex dielectric permittivity (ε') and dielectric loss tangent ($\tan\delta$) in BFMO (x=0–0.4) under different measuring frequencies. Figure 3.19(a) shows that with the increase of temperature, there is a gradual increase in ε' and $\tan\delta$ of pure BFO ceramic. At room temperature and at 1 kHz, for pure BFO, the dielectric constant and loss tangent are about 70 and 0.07, respectively, similar to those reported [16]. Both ε' and $\tan\delta$ decrease with increasing frequencies because the dipoles are unable to follow the alternating of applied field under high frequency. The weak frequency and temperature dependent shows that the contribution to the dielectric properties is dominated by the electrons/domains rather than by the dipoles of the charge defects [16].

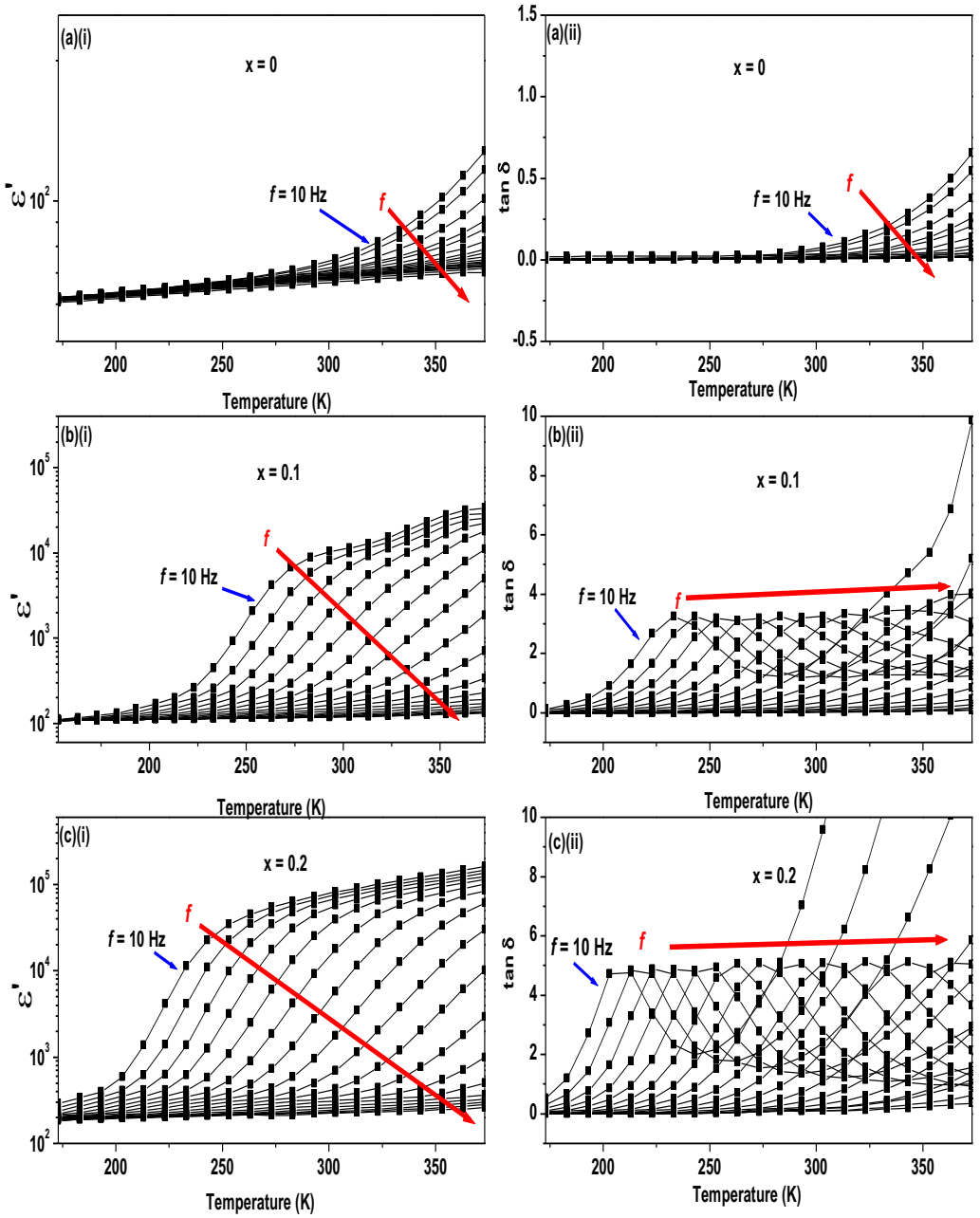
(a)(i)
x = 0
f = 10 Hz
f
ε' 10²
Temperature (K)
(a)(ii)
x = 0
f = 10 Hz
f
tan δ
Temperature (K)
(b)(i)
x = 0.1
f
f = 10 Hz
ε'
Temperature (K)
(b)(ii)
x = 0.1
f = 10 Hz
f
tan δ
Temperature (K)
(c)(i)
x = 0.2
f
f = 10 Hz
ε'
Temperature (K)
(c)(ii)
x = 0.2
f = 10 Hz
f
tan δ
Temperature (K)

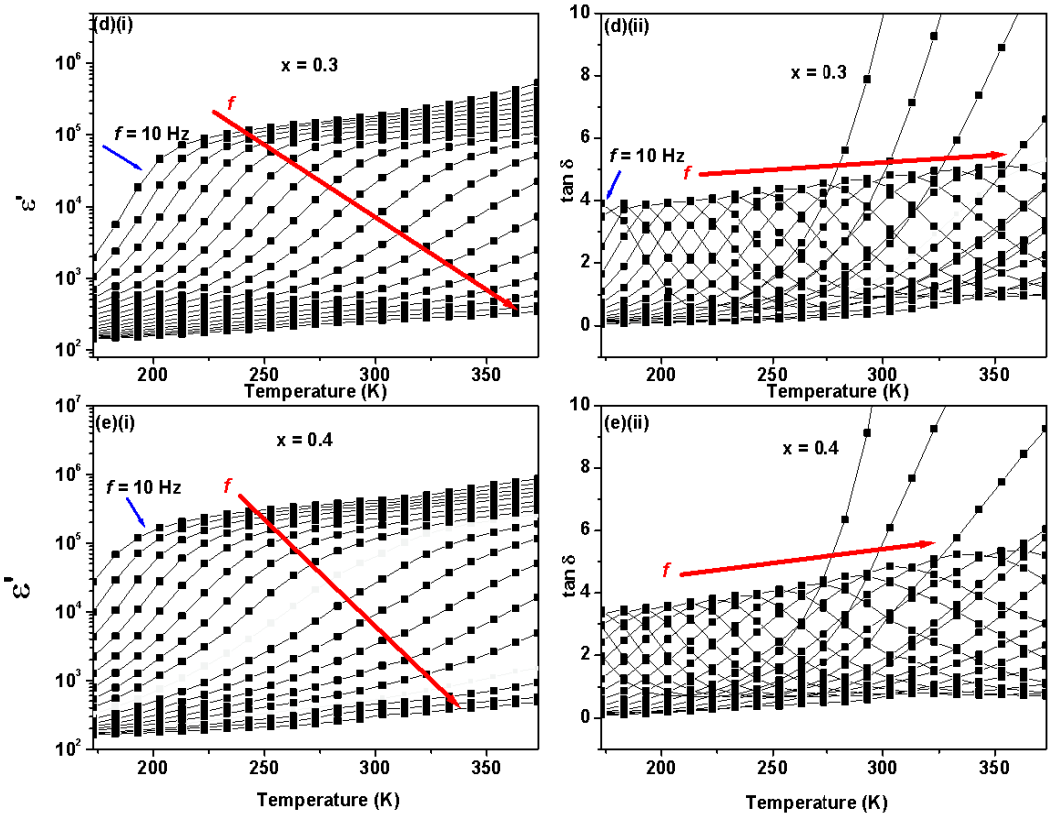

Figure 3.19 Dielectric properties of BFMO ceramics: (i) relative dielectric permittivity ε' and (ii) dielectric loss tanδ with different concentrations of Mn: (a) x=0, (b) x=0.1, (c) x=0.2, (d) x=0.3, and (e) x=0.4.

In BFMO (x=0.1–0.4), which was doped with Mn, a giant dielectric constant can be observed (as shown in Figure 3.19). It can be seen that all Mn-doped BFO ceramics exhibit a large dielectric relaxation response below or around room temperature. With increasing temperatures, ε' (T) displays a step-like increase to a giant value of about 10^5 at low frequency in Mn-doped BFO ceramics. A Debye-like relaxation peak corresponding to the step-like increase in dielectric constant ε'(T) can be clearly

observed. Corresponding to the step-like increase in ε'(T) is a peak in dielectric loss tangent (tanδ) and the peak position shifts to higher temperatures as the measuring frequency increases. Figure 3.20 (a) – (b) illustrate the frequency dependence of the relative dielectric permittivity (ε') and dielectric loss tangent (tanδ) for BFMO (x=0.1–0.4) ceramics measured at room temperature. All the ceramics display a decreasing trend in ε' with increasing frequency from 10Hz to 10 MHz. Moreover, with increasing amount of Mn doping, the dielectric constant increases and the dielectric relaxation becomes more significant. The peak of loss tangent (tan δ) which corresponds to the dielectric relaxation shifts to higher frequencies with increasing amount of Mn doping. Hence the dielectric properties of the ceramics are strongly dependent on the Mn doping level.

As reported, the leakage current in BFO is dominated by Poole-Frenkel emission [77]. In pure BFO, the conduction mainly comes from the oxygen vacancies rather than from Fe^{2+} ions [77]. However, the conduction mechanism in doped sample becomes complicated. In order to understand the physical nature of the dielectric relaxation observed in Figure 3.19, the following Arrhenius equation was used to fit the relaxation frequency (corresponding to the peak in dielectric loss spectra) with the corresponding temperature,

$$f = f_0 \exp(-E_a / kT) \tag{3.5}$$

where f_0 is a pre-exponential coefficient, E_a is the activation energy of conduction or the

ionization energy of a Poole-Frenkel trap, k is Boltzmann's constant and T is the absolute temperature.

The calculated activation energies are summarized in Figure 3.21, where E_a=0.39, 0.37, 0.31 and 0.29 eV for BFMO (x=0.1–0.4) ceramics, respectively. These values are far less than the reported activation energy for the migration of oxygen vacancy in perovskite oxides (0.9-1.4eV) [78]. However, these E_a values are comparable with the activation energy of 0.290 eV for the dielectric relaxation in $LuFe_2O_4$ which is due to a two-site polaron hopping process accompanied by the charge transfer between Fe^{2+} and Fe^{3+} [79]. Moreover, with increasing doping concentration, the activation energy was decreased. This implies that the conduction mechanism of the samples is related to the addition of Mn. The doping of Mn may introduce the hoping motion between Fe^{3+} and Mn^{3+}. Based on first principles calculation, due to the strong hybridization between Fe/Mn 3d and O 2p orbitals, the Fe^{3+}-O^{2+}-Mn^{3+} superexchange interaction should be considered and it is responsible for the magnetic properties observed in BFMO [37, 80].

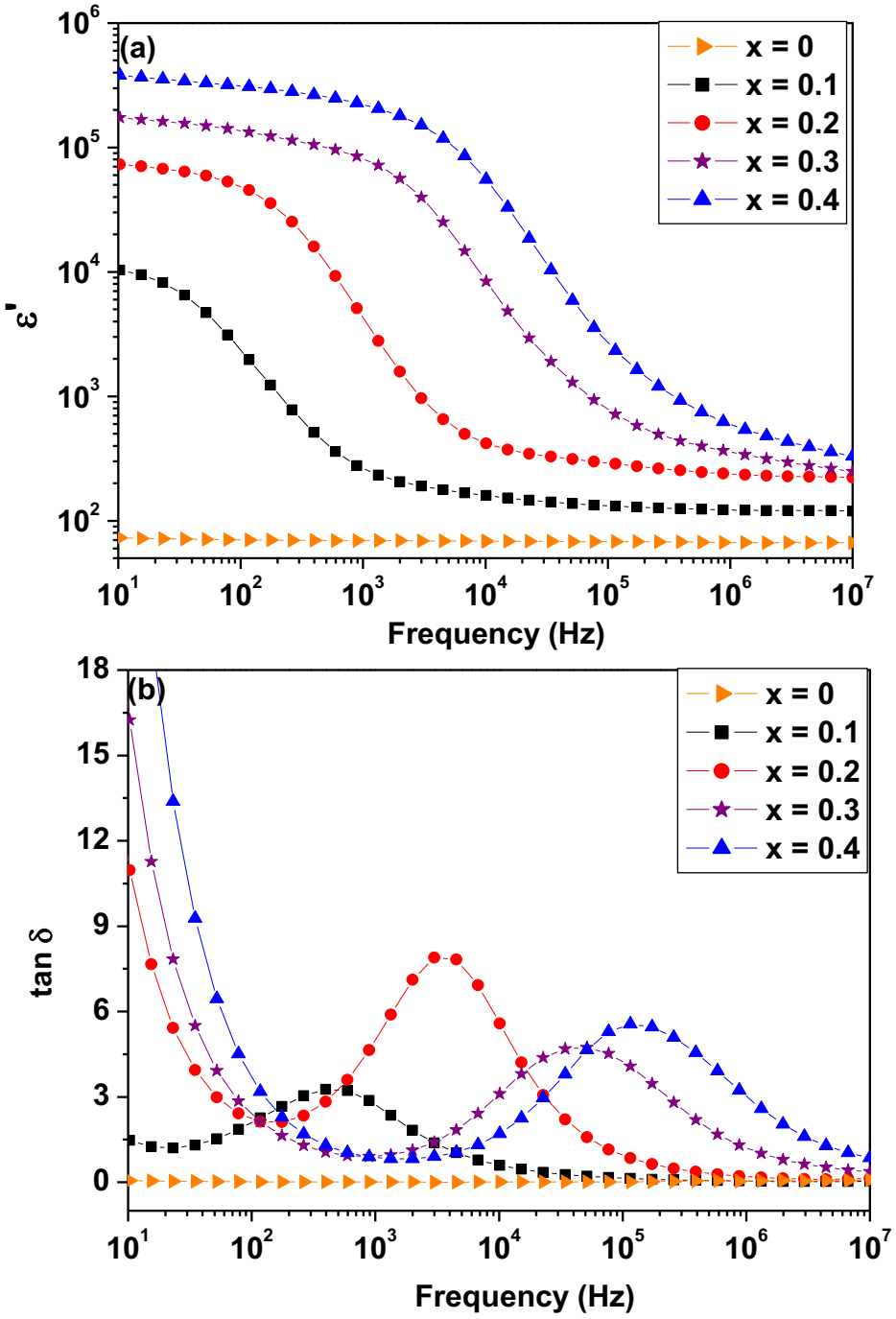

Figure 3.20 Frequency dependent dielectric properties of BFMO ceramic with different concentration (x=0–0.4) measured at room temperature: (a) relative dielectric constant ε'(T) and (b) dielectric loss tanδ.

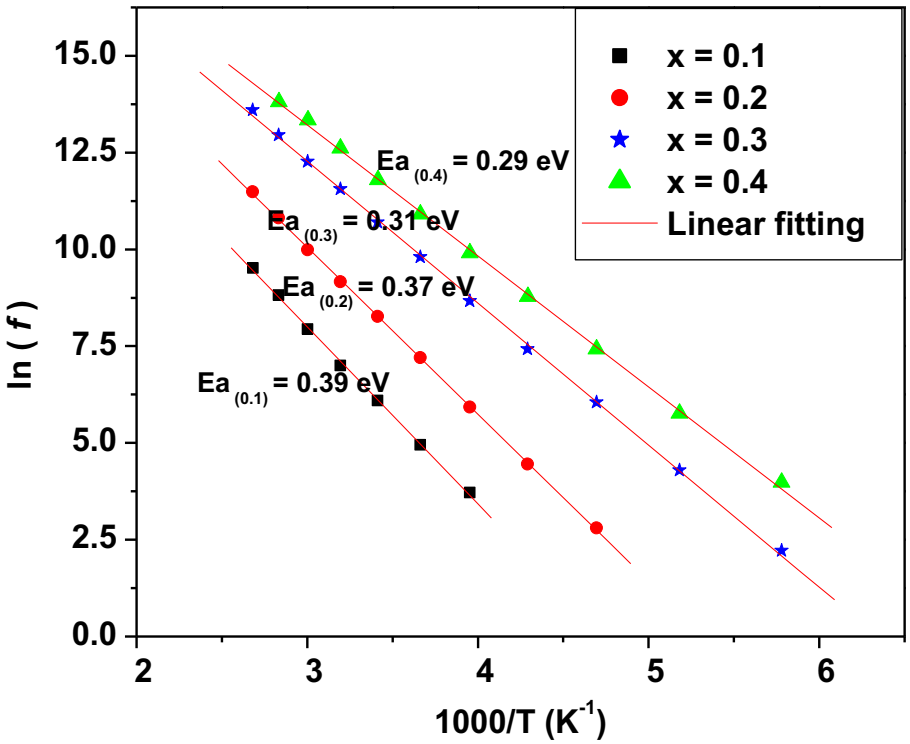

Figure 3.21 Arrhenius fitting on the activation energy (E_a) of BFMO (x=0.1-0.4).

Impedance analysis (Cole-Cole plot):

In order to study the impedance properties based on the microstructure of BFMO (x=0.1–0.4) ceramics, the equivalent circuit analysis was applied by using the Cole-Cole plot or Nyquist diagram (Z" versus Z', where Z' and Z" are the real and imaginary parts of the impedance, respectively). Such a plot allows the differentiation of the contribution from the grain and/or grain boundary in the samples. When the impedance data are

plotted in the Cole-Cole plot, a semi-circle can be displayed which corresponds to a particular physics mechanism involved in the sample. In theory, the displayed semicircle is equivalent to a microstructure formed by parallel conducting and capacitive components of the samples. In the equivalent circuit model, each semicircle can be considered as the combination of a capacitor and a resistor. In most of the cases, the Cole-Cole plot may contain more than one semicircle. It can be considered as a series of combinations of capacitor and resistor as represented by Figure 3.22, one representing the grain effect and the other the grain boundary effect. Let (R_g, C_g) and (R_{gb}, C_{gb}) be the resistances and capacitances of grains and grain boundaries, respectively, the complex impedance Z* for the equivalent circuit in Figure 3.22 can be represented by,

$$Z^* = Z_g + Z_{gb} \tag{3.6}$$

$$Z_g = \frac{1}{\frac{1}{R_g}+i\omega C_g} = \frac{R_g}{1+(\omega R_g C_g)^2} - i\frac{\omega R_g^2 C_g}{1+(\omega R_g C_g)^2} \tag{3.7}$$

$$Z_{gb} = \frac{1}{\frac{1}{R_{gb}}+i\omega C_{gb}} = \frac{R_{gb}}{1+(\omega R_{gb} C_{gb})^2} - i\frac{\omega R_{gb}^2 C_{gb}}{1+(\omega R_{gb} C_{gb})^2} \tag{3.8}$$

$$Z^* = \frac{1}{\frac{1}{R_g}+i\omega C_g} + \frac{1}{\frac{1}{R_{gb}}+i\omega C_{gb}} = Z' - iZ'' \tag{3.9}$$

where

$$Z' = \frac{R_g}{1+(\omega R_g C_g)^2} + \frac{R_{gb}}{1+(\omega R_{gb} C_{gb})^2} \tag{3.10}$$

$$Z'' = R_g\left[\frac{\omega R_g C_g}{1+(\omega R_g C_g)^2}\right] + R_{gb}\left[\frac{\omega R_{gb} C_{gb}}{1+(\omega R_{gb} C_{gb})^2}\right] \quad (3.11)$$

Based on the above equations, the angular frequencies at the maxima of the semicircles corresponding to grains and grain boundaries are $\omega_g = \frac{1}{R_g C_g}$ and $\omega_{gb} = \frac{1}{R_{gb} C_{gb}}$, respectively.

In general, we attribute the first semicircle (higher frequency response) to the grain or bulk effect and the second one (lower frequency response) to the grain boundary effect, because the peak frequency for grains is usually much higher than that for grain boundaries due to their large difference in the values of capacitance and resistance. If there is a third semicircle, it would normally be considered as the electrode contribution. The intercept of each semicircle on the real axis can be evaluated as the resistance of the equivalent circuit. In fact, sometimes the curve plotted cannot be simply represented by ideal resistors and capacitors since the curves are not exactly semicircles. Hence, constant phase element (CPE) is usually put into the circuit to describe the non-ideal capacitor which causes the depressed semicircle. CPE can be described by a complex impedance of $Z = \frac{1}{(i\omega C)^\alpha}$, where C is the ideal capacitance and α is an empirical constant (between 0 and 1) that is directly related to the depression (flatness) of the semicircle. α=1 represents an ideal capacitor (*C*) in parallel with a resistor (*R*) and the relaxation behavior resembles an ideal Debye system, exhibiting a perfect semicircle. When α<1, the CPE element can be considered as a capacitor, but with a constant phase angle that is less than 90° at all frequencies. Such a capacitor, when placed in parallel with a resistor,

forms a depressed semicircle in the Cole-Cole plot.

Figure 3.23 shows the Cole-Cole plot for BFMO (x=0.1–0.4) in a frequency range of 10 Hz to 10 MHz at 293 K. Two semicircular arcs can be seen which arise from the contributions of the grain/bulk and grain boundary. The experimental data were fitted the WINFIT program provided by NOVOCONTROL and an equivalent circuit was obtained by a least-mean-square fitting routine. It was found that all the semicircles exhibit a certain degree of depression. But α is close to 1 for all the samples, which implies that it is close to Debye-like behavior. The resistances of grains (R_g) and grain boundaries (R_{gb}) were evaluated from the intercept of the corresponding arcs with the real axis as shown in Figure 3.23. The Cole-Cle plot reveals a relatively large grain boundary contribution to the total resistance with increasing Mn doping.

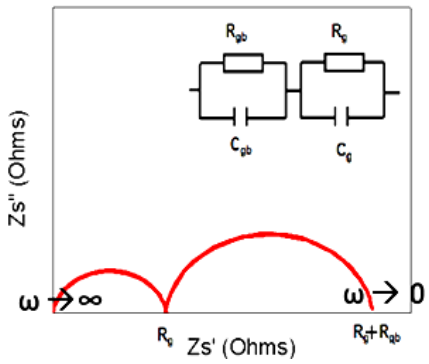

Figure 3.22 A representative Cole-Cole plot. The inset shows the equivalent circuit with two sub-circuits. The first and second circuits correspond to grain and grain boundary effect, respectively.

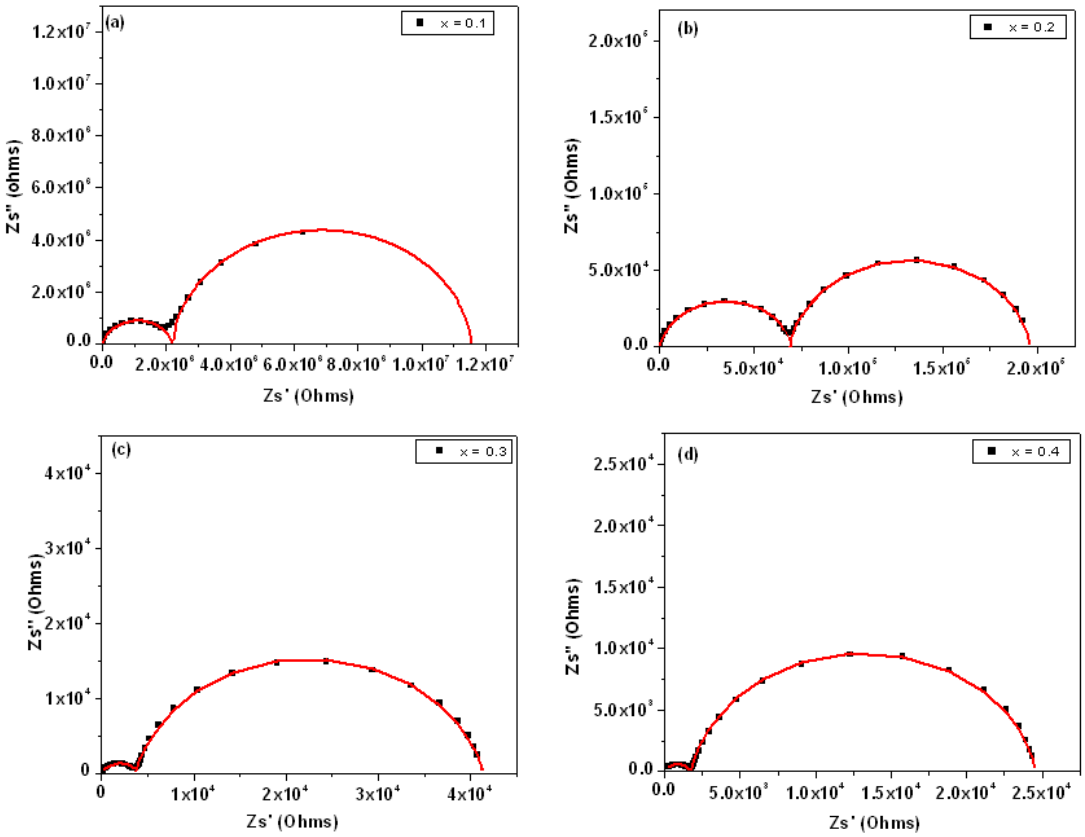

Figure 3.23 Cole-Cole plots for BFMO at 293 K in the frequency range of 10 Hz to 10 MHz: (a) x=0.1, (b) x=0.2, (c) x=0.3, and (d) x=0.4. Symbols are experimental data points, while the semicircular arcs are the fitted curves.

Figure 3.24 shows the Arrhenius plots of the bulk and grain boundary resistances evaluated from the Cole-Cole plots against the reciprocal of temperature for Mn doped ceramics. It can be seen that all the data obey the Arrhenius law $R = R_0 \exp(-E_a / kT)$, where R is the bulk/grain boundary resistances, R_0 is a pre-exponential coefficient, E_a is the activation energy of conduction or the ionization energy of a Poole-Frenkel trap, k is

Boltzmann's constant and T is the absolute temperature. The activation energies obtained for the grain and grain boundary conduction are between 0.25 and 0.39 eV. Since the activation energies for grain and grain boundary are similar, the conduction in the grain and grain boundary regions could be dominated by the same mechanism. Hence it is not appropriate to explain the conduction behavior in BFMO by the brick-layer model where the activation energy for grain boundary is larger than that for grain. The conduction mechanism in BFMO can be explained by the so-called constriction resistance model where the grain boundary region is considered to be the same as bulk but with a smaller cross-sectional area due to the development of necking between grains [81-83]. Hence the activation energy for the grain-boundary response is nearly the same as that for the grain.

The activation energies obtained from the Cole-Cole plots are consistence with those obtained from the dielectric spectrum as shown in Figure 3.21. They also show the same decreasing trend with increasing amount of Mn doping. The decreased resistivity for the grain and/or grain boundary with increasing amount of Mn doping is a result of the reduced energy barrier for conduction.

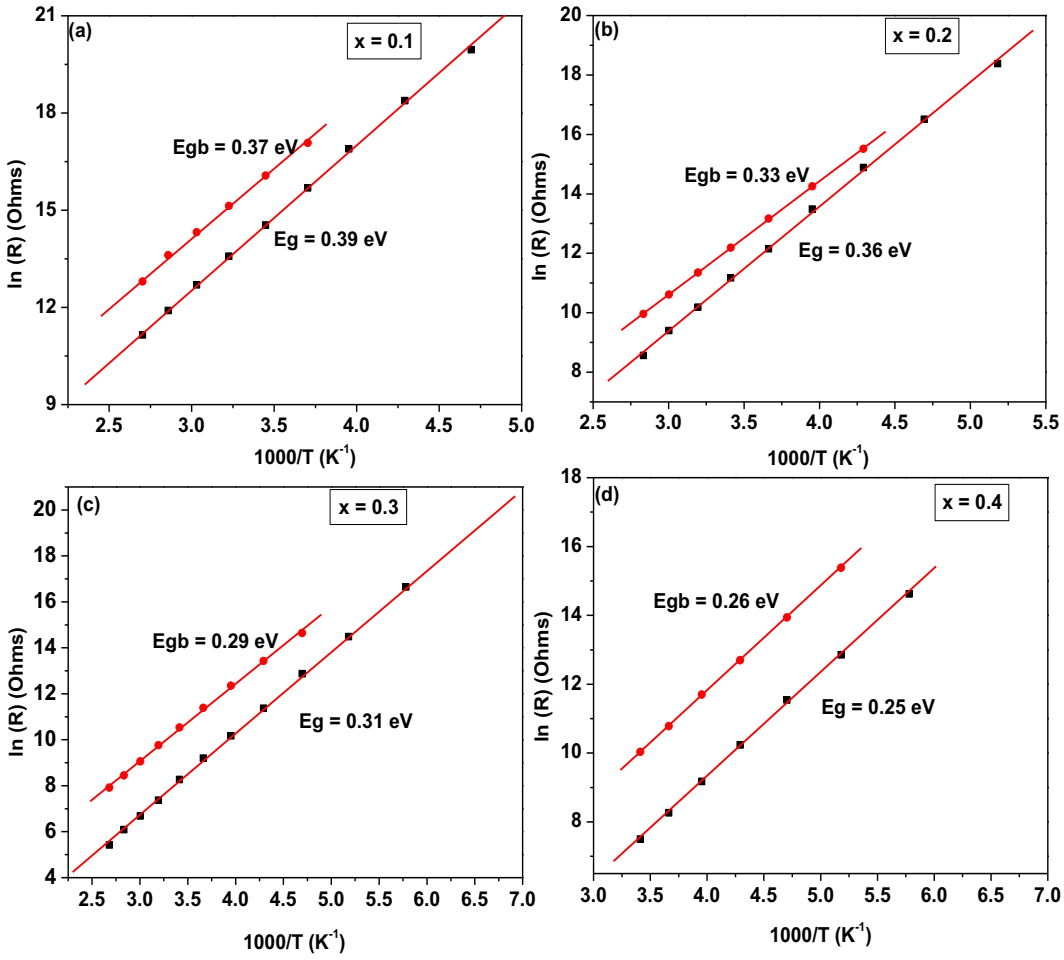

Figure 3.24 Arrhenius fit for the grain and grain boundary resistances of BFMO versus reciprocal of temperature: (a) x=0.1, (b) x=0.2, (c) x=0.3, and (d) x=0.4. Symbols are experimental data points, while the straight lines are best-fitted lines according to Arrhenius law.

3.7 Magnetic properties

VSM was employed to investigate the magnetic properties of BFMO (x=0–0.4) ceramics. Figure 3.25 shows magnetic hysteresis loop of BFO ceramic which was synthesized by the conventional solid state reaction method, exhibiting a ferromagnetic behavior. The ferromagnetic properties could have been induced by Fe-related impurity clusters in the sample, which has been detected by XRD and has been mentioned in section 3.2. The existence of large amount of Fe^{2+} has also been confirmed in XPS spectrum and will be discussed in section 3.9. Hence this ferromagnetic behavior is not intrinsic in BFO.

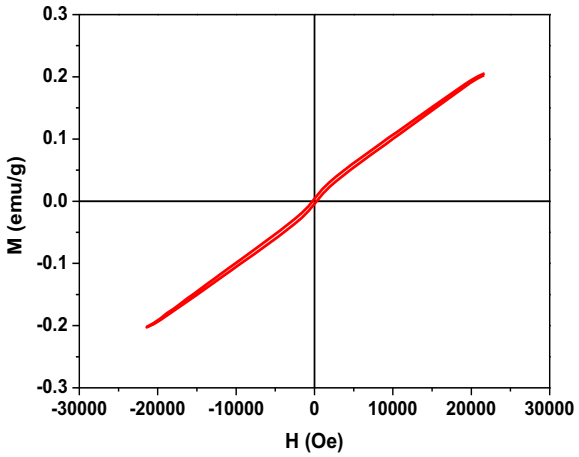

Figure 3.25 Magnetization versus magnetic field (M-H) curve of BFO ceramics which were synthesized by the conventional solid-state reaction method.

Figure 3.26 (a) – (e) show the magnetization hysteresis (M-H) loops of BFMO (x=0–0.4) ceramics measured at room temperature and 78K, respectively. The remnant

magnetization (M_r) against composition is summarized in Figure 3.27. BFO sample exhibits a M_r that is close to zero both at 78 and 300K, reflecting a typical canted antiferromagnetic behavior with a space modulated spin structure. It is noticed that as the temperature is decreased from room temperature to 78 K, the magnetization decreases slightly, in accordance with the well-known temperature dependent magnetization of antiferromagnetics [12, 84]. Figure 3.27 clearly shows that the intrinsic antiferromagnetic BFO becomes weak ferromagnetic with a small but nonzero remnant magnetization (M_r) when Mn is doped. The M_r value in BFMO (x=0.1) is around 0.00114 emu/g. Further increase in Mn concentration results in the increase of the remnant magnetization to 0.00159, 0.00449, and 0.00674 emu/g for BFMO (x=0.2, 0.3, and 0.4), respectively, at 78K. The gradually increase in remnant magnetization with increasing Mn doping level is due to the suppressed magnetic spin structure by Mn doping. As reported by Sosnowska *et al.*[26], Mn doping resulted in a transition of magnetic ordering, from the long-range spiral spin G-type antiferromagnetic ordering (BFO) to a collinear G-type antiferromagnetic one with spins along c axis. Such a suppression of the spiral spin structure is presumably responsible for enhanced macroscopic magnetization. Moreover, for BFMO (x=0.4), the remnant magnetization is enhanced greatly. As confirmed by our first principles calculation [80], the increased magnetization comes from the Fe-O-Mn antiferromagnetic superexchange interactions, rather than the antiferromagnetic superexchange interactions of Fe-O-Fe and Mn-O-Mn, which basically cancel the magnetization of BFMO system. The addition of Mn has frustrated the antiferromagnetic ordering of BFO and results in macroscopic

magnetization.

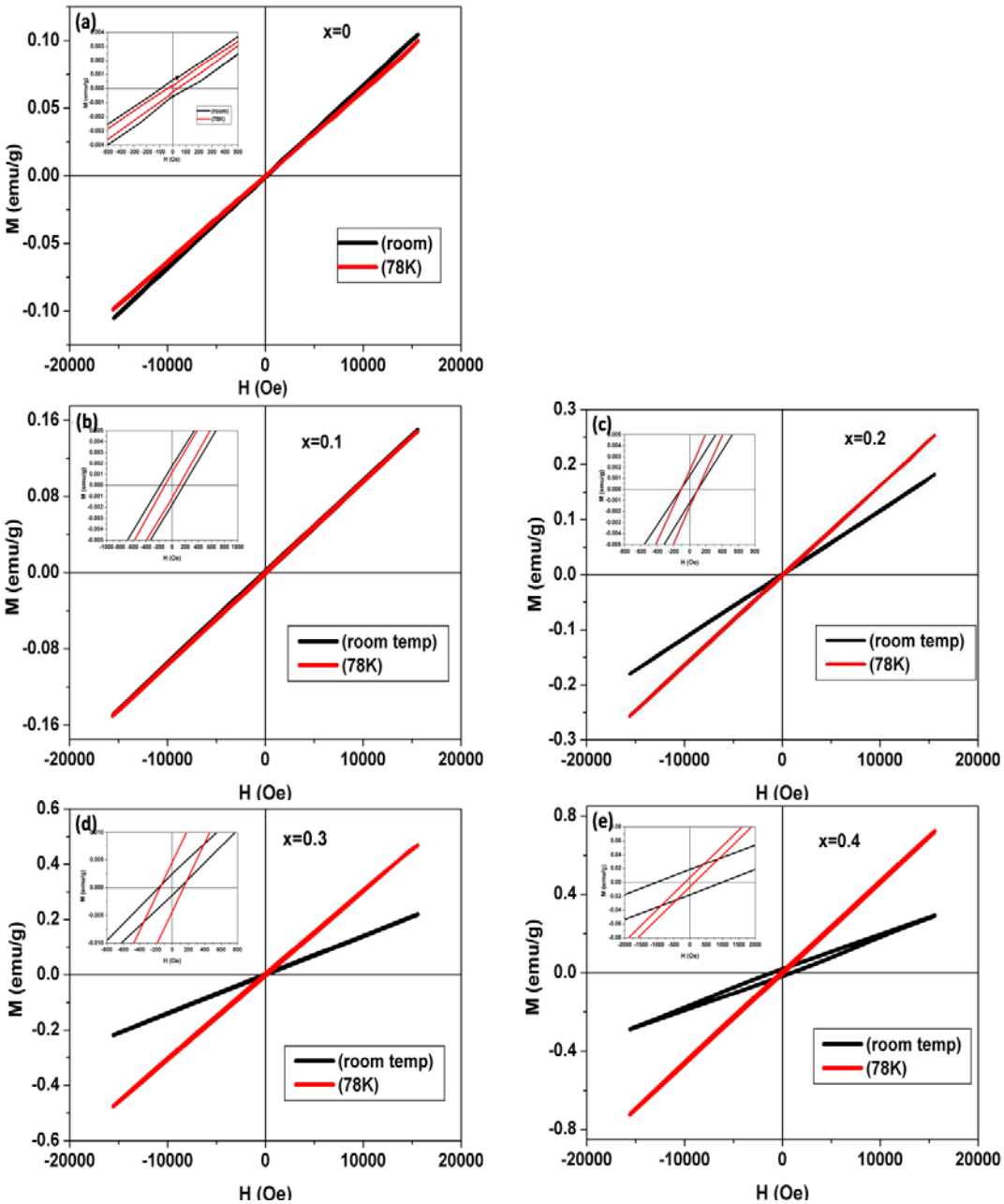

Figure 3.26 Magnetization versus magnetic field (*M-H*) curve of BFMO ceramics (a) x=0, (b) x=0.1, (c) x=0.2, (d) x=0.3, and (d) x=0.4 at room temperature and 78K, respectively. (inset) Enlarged *M-H* curve near the zero field region.

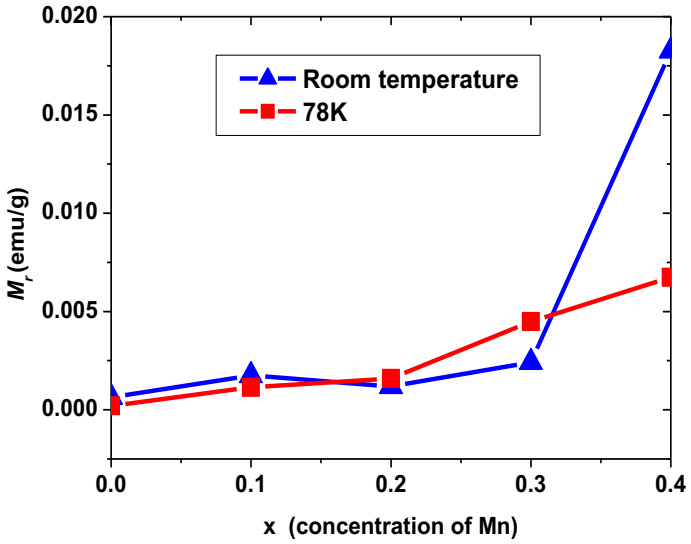

Figure 3.27 Remnant magnetization (M_r) as a function of concentration (x) in BFMO ceramics measured at room temperature and 78 K, respectively.

3.8 Raman analysis

Raman scattering spectroscopy is an effective tool to study the local structure of materials. Due to its high sensitivity to atomic vibrations, Raman spectroscopy is very helpful in the study of vibration modes of BFMO.

Base on group theory, there are 13 Raman active modes ($4A_1$+$9E$) for BFO, which has the distorted perovskite rhombohedral ($R3c$) structure [85]. All of these modes exist in the frequency range below 700 cm^{-1} and hence the current study is focused on this range. Figure 3.28 shows the Raman spectrum of pure BFO. The measured spectrum was fitted by decomposing the curve into each individual Raman active components with a Lorentz-type curve.

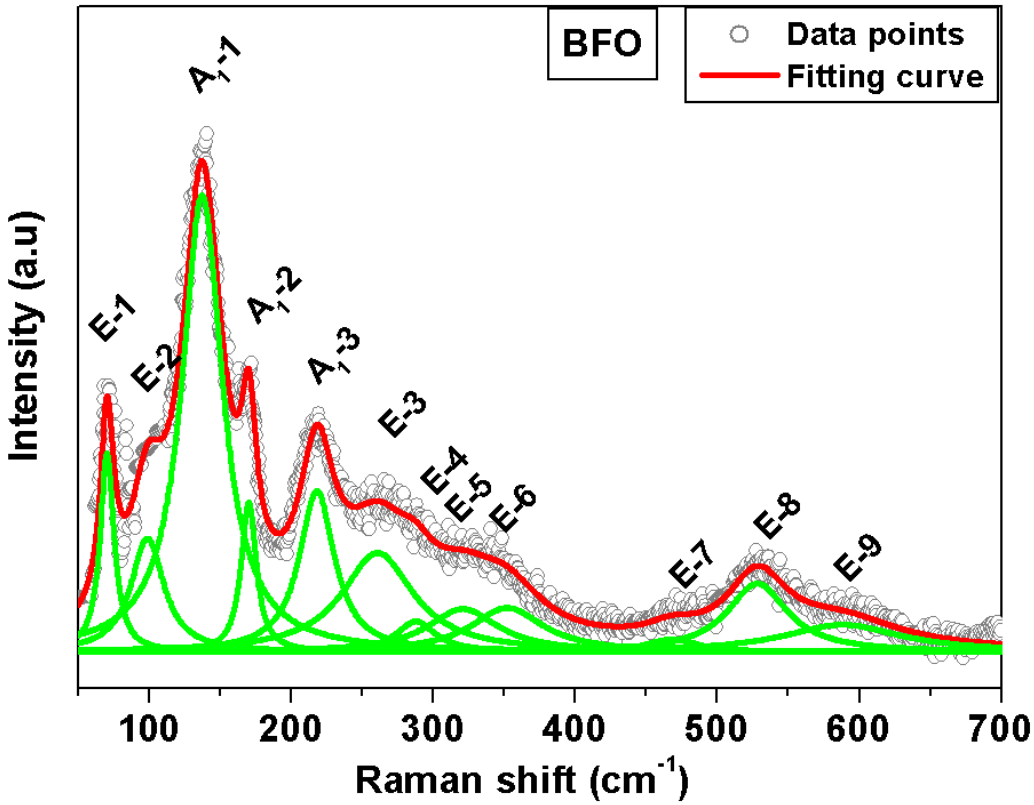

Figure 3.28 Raman spectrum of pure BFO measured at room temperature. The grey circular points are the experimental data. The red line is the fitting curve and the green ones are the individual Raman active mode with Lorentz-type curve.

The obtained Raman peak positions are compared with those reported in Table 3. 2. The reported data were either from single crystal BFO measured at low temperatures [86, 87] or from polycrystalline BFO measured at room temperature [88, 89]. The Raman modes obtained from our BFO sample match closely to the data reported, where the E modes are located at around 70, 99, 261, 288, 320, 352, 468, 528 and 588 cm^{-1} and the A_1 modes are located at around 137, 170 and 218 cm^{-1}, respectively. The A_1-4 mode

was too weak to be detected. In fact, Raman signals in polycrystalline ceramics are relatively weak when measured at room temperature. Therefore the observable Raman modes at room temperature are comparatively less than that in single crystal measured at a lower temperature. Moreover, there are slight differences in the Raman peak positions among various reported values since different synthesis conditions may affect the oxygen stoichiometry and result in different vibration frequencies involving oxygen bonding.

Mode	Ceramic	Kothari et al. ceramic at 300K [88]	Yuan et al. ceramic at 300K [89]	Cazayous et al. single crystal at 10 K [87]	Fukumura et al. single crystal at 4 K [86]
E - 1	70.27	71.39 (E)	-------	75 (E-TO)	77 (E)
E - 2	98.62	98.36 (E)	111.7 (E)	81 (E-LO)	-------
A_1 - 1	137.2	135.15 (A_1-1)	126.1 (A_1-1)	132 (E-TO)	136 (E)
	-------	-------	-------	145 (A_1-LO)	147 (A)
A_1 - 2	169.99	167.08 (A_1-2)	165.5 (A_1-2)	175.5 (A_1-LO)	176 (A)
A_1 - 3	218	218.11(A_1-3)	213 (A_1-3)	222.7 (A_1-LO)	227 (A)
E - 3	260.74	255.38 (E)	259.5 (E)	263 (E-TO)	265 (E)
E - 4	287.64	283 (E)	-------	276 (E-TO)	279 (E)
E - 5	320.68	321.47 (E)	339.6 (E)	295 (E-TO)	351 (E)
E - 6	352	352.55 (E)	366.6 (E)	348 (E-TO)	375 (E)
A_1 - 4	-------	430.95 (A_1-4)	-------	441 (E-TO)	437 (E)
E - 7	467.5	468 (E)	476.9 (E)	471 (A_1-LO)	473 (E)
E - 8	528.12	526.22 (E)	530.9 (E)	523 (E-TO)	490 (A)
E - 9	588.35	598.84 (E)	599.6 (E)	550 (A-TO)	525 (E)

Table 3. 2 Comparison among the peak positions in Raman spectrum obtained from our BFO sample and those from literatures [86-89].

The Raman spectra of BFMO (x=0.0–0.4) are shown in Figure 3.29. The Raman peak positions are summarized in Table 3. 2 and plotted as a function of composition as shown in Figure 3.30. Actually, a clear assignment of every Raman mode to a specific bond motion is still lacking. Recently, Hermet *et al*. [90] and Tutuncu *el al.* [91] attempted to give bond assignment to the active Raman modes based on first principles calculation. Hermet *et al.* [90] reported that Bi atoms participate in modes above 262 cm^{-1}. Fe atoms are mainly involved in modes between 152 and 261 cm^{-1} but also contribute to some higher frequencies. Tutuncu *el al*. [91] assigned four Raman modes with the specific bond contribution, i.e., 164 cm^{-1} mainly from the atomic vibrations of Fe-O and Bi-O, 316cm^{-1} mainly from the Fe-O bond with larger amplitude for the oxygen atoms, and 288 and 514 cm^{-1} from atomic vibrations in the oxygen planes.

As shown in Figure 3.29, the A_1-1 mode is broadened and shifted to higher frequencies in Mn doped samples. The A_1-1 mode is attributed to Bi-O vibrations. Its mode frequency (f) is dependent on local factors, such as the force constant (k), ionic mass (m) of the doping element, and specific bond length between the atoms, etc. (i.e. $f \propto \sqrt{\frac{k}{m}} \propto \frac{1}{\text{bond length between the atoms}}$). Hence the Raman shift is inversely proportional to bond length. The shift of A_1-1 mode to higher frequencies is consistent with our XRD study which shows a gradual decrease in the lattice parameter with increasing Mn doping level. The relative intensity of A_1-2 mode at 169.99 cm^{-1} is greatly reduced in Mn doped samples. This phenomenon is also reported in 5 mol % Mn doped BFO thin films [63]. The A_1-2 mode is related to the Fe-O bond and partially to

the Bi-O bond. Due to the strong hybridization between the Fe/Mn 3*d* orbitals and O 2*p* orbitals, the Fe-O-Fe chain in BFO sample was broken by Mn doping and thus resulted in the disappearance of A_1-2 mode. Moreover, the E-4, E-7, E-8 and E-9 modes all shifted gradually to higher frequencies with increasing Mn content. These modes mainly come from the oxygen plane vibrations and hence are related to the structural transformations observed in Mn doped samples.

Furthermore, there is a sharp change in the spectrum of BFMO (x=0.4) as compared to that of BFO. Two strong and wide bands appear at around 524 and 616 cm^{-1}. These two modes have also been reported in Mn doped BFO films [63] and in $LaMnO_3$ [92]. They are related to Mn^{3+}-induced strong Jahn-Teller octahedra distortion [93]. Hence, the strong Jahn-Teller octahedra distortion resulted from the Jahn-Teller active Mn ion is considered to be the origin of the observed Raman peaks.

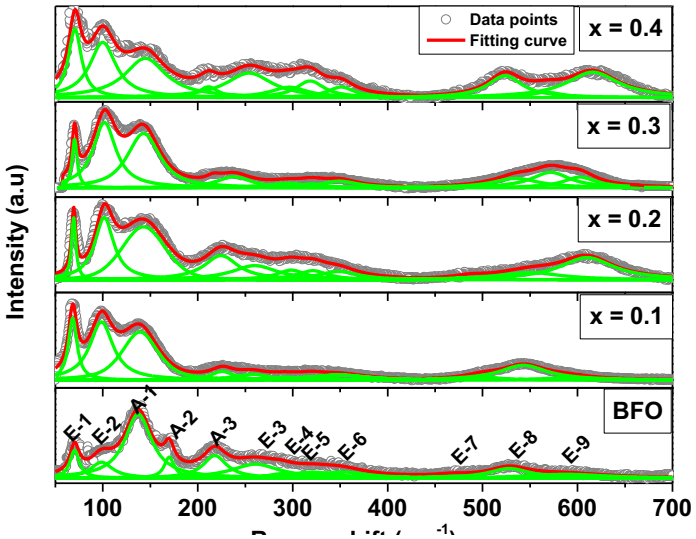

Figure 3.29 Raman spectra of BFMO (x=0–0.4) with individual Lorentz component fitting.

Mode	BFO	BFMO (10%)	BFMO (20%)	BFMO (30%)	BFMO (40%)
E - 1	70.27	69.79	69.33	70.27	70.579
E - 2	98.62	100.1	101.49	101.7	99.96
A_1 - 1	137.2	140.8	142.6	142.6	144.76
A_1 - 2	169.99	-------	-------	-------	-------
A_1 - 3	218	227.35	224.49	216	211.22
E - 3	260.74	258.9	260	238	254.04
E - 4	287.64	294.1	298.37	294	296.28
E - 5	320.68	320.56	321.15	320	318.35
E - 6	352	350.2	348.26	349.06	350.93
A_1 - 4	-------	-------	-------	-------	-------
E - 7	467.50	499.45	487.56	535.07	523.5
E - 8	528.12	542.95	549.35	571.73	567.07
E - 9	588.35	588.9	609.75	602.55	616.09

Table 3. 3 Summary of Raman modes obtained from the fitting of Raman spectrum of BFMO (x=0–0.4).

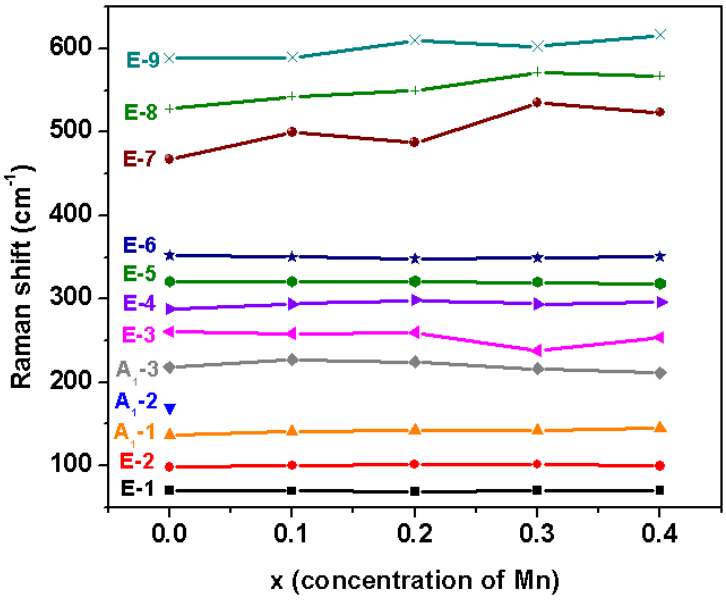

Figure 3.30 Raman shift of each mode as a function of Mn concentration (x).

3.9 Cationic stoichiometry

In order to identify the composition of the synthesized ceramics, EDX was conducted and the results were analyzed. The compositions ratio of BFMO (x = 0-0.4) samples were calculated by contrasting the atomic percentage of the Bi, Fe, Mn elements, these results are summarized in Table 3.4, it give a result of nearly equi-atomic ratio of Bi and (Fe +Mn) in all the samples with an acceptable errors. Actually, the composition ratio of the elements also can be calculated from XPS spectra; however we need to known a reference sensitivity factor from the spectrometer. In our case, we did not scan the reference material to get these parameters, we cannot compare the different elements concentration from the spectra. But XPS spectra still can help us to identify the different valence of the same element (Fe or Mn), since they are based on the same strong peak which is obey the same sensitivity factor, and deduce the same background, so the concentration ratio of each valence states, related to the area under the each corresponding valence peak curve, can be found.

BFMO (x)	Atomic %			Atomic ratio
	Bi	Fe	Mn	Bi : (Fe + Mn)
x=0	16.32±0.33	16.17±0.24	0	1.01 ±0.03: 1
x=0.1	16.45±0.38	14.70±0.21	1.59±0.08	1.01 ±0.01: (0.90 + 0.10)
x=0.2	17.10±0.48	13.80±0.40	3.38±0.05	1 ±0.05: (0.80 + 0.20)
x=0.3	16.77±0.47	12.05±0.31	4.96±0.16	0.99 ±0.03: (0.71 + 0.29)
x=0.4	16.74±0.15	10.48±0.19	6.73±0.11	0.98±0.02 : (0.61 + 0.39)

Table 3. 4 Summary of atomic percentage and composition ratio of BFMO (x=0–0.4).

3.10 Valence state

In order to identify the valence state of Fe and Mn ions in the synthesized ceramics, X-ray photoelectron spectroscopy was conducted on the samples and the results were analyzed. Figure 3.31 shows the XPS spectra of BFO samples, which were synthesized by the solid state reaction and rapid liquid-phase sintering methods, respectively. It is known that the binding energies of Fe^{2+} and Fe^{3+} are slightly different, and can be differentiated from the XPS spectra [94]. The measured Fe $2p_{3/2}$ peak can be deconvoluted into two peaks, corresponding to the Fe^{2+} and Fe^{3+} states, respectively. The binding energies for Fe^{3+} state is 711eV and that for Fe^{2+} is 709.5eV [94]. The coexistence of Fe^{3+} and Fe^{2+} states in both samples can be confirmed by curve fitting. It is found that the concentration ratio of Fe^{2+} to Fe^{3+} is higher in the sample synthesized

by solid state reaction method than the one synthesized by rapid liquid-phase sintering method. For BFO synthesized by the rapid liquid-phase sintering method, the majority of Fe ions are in a valence state of +3. This explains the better ferroelectricity observed in samples synthesized by the rapid liquid-phase sintering method. The existence of Fe^{2+} may introduce oxygen vacancies for charge compensation and thus results in large leakage current to prevent the ferroelectric hysteresis loop from being observed.

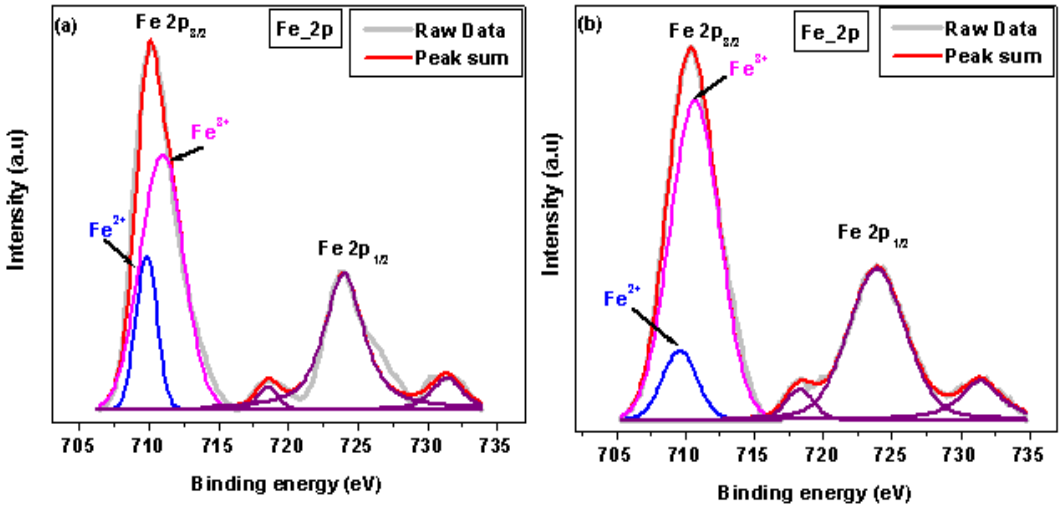

Figure 3.31 XPS spectra for Fe 2*p* in BFO samples synthesized by (a) solid-state reaction and (b) rapid liquid-phase sintering. The blue curve is the fitting curve for Fe^{2+} and the pink curve is the fitting curve for Fe^{3+}.

The Fe 2*p* lines of BFMO (x=0–0.4) samples are shown in Figure 3.32. Through curve fitting, by comparing the area under each peak, it can be found that the ratio of Fe^{3+} to Fe^{2+} is almost independent of Mn concentration and is quite similar to that of BFO. Hence, it can be concluded that the existence of Fe^{2+} may arise from intrinsic oxygen vacancies. Figure 3.33 shows Mn $2p_{3/2}$ spectrum in Mn doped BFO. The curves

were also deconvoluted into peaks corresponding to Mn^{4+}, Mn^{3+} and Mn^{2+} states with the binding energy of 642.75, 641.66 and 641 eV, respectively [95, 96]. For Mn doped BFO, the valence state for the majority of Mn ions is +3. While for BFMO (x=0.4), a tiny amount of Mn ions in +2 and +4 states can be detected.

From the above results, it can be seen that, in BFMO, the majority of Fe and Mn ions is in +3 states. The existence of Fe^{2+} state is intrinsic (due to oxygen vacancies) and independent of Mn concentration. This supports the previous discussion on the conduction mechanism of BFMO that it is dominated by the hopping conduction along Fe^{3+}-O^{2+}-Mn^{3+} chain.

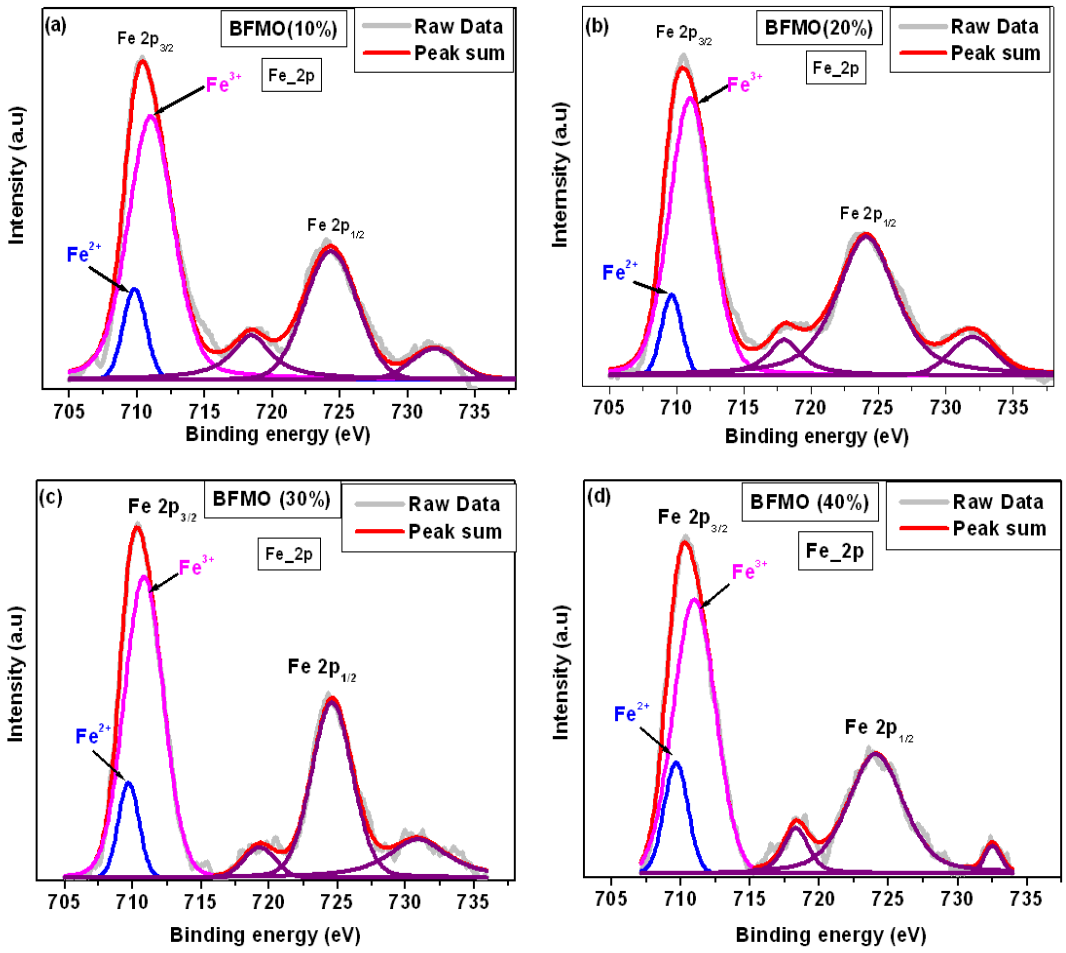

Figure 3.32 XPS spectra for Fe 2*p* in BFMO samples with (a) $x = 0.1$; (b) $x = 0.2$; $x = 0.3$; and (d) $x = 0.4$.

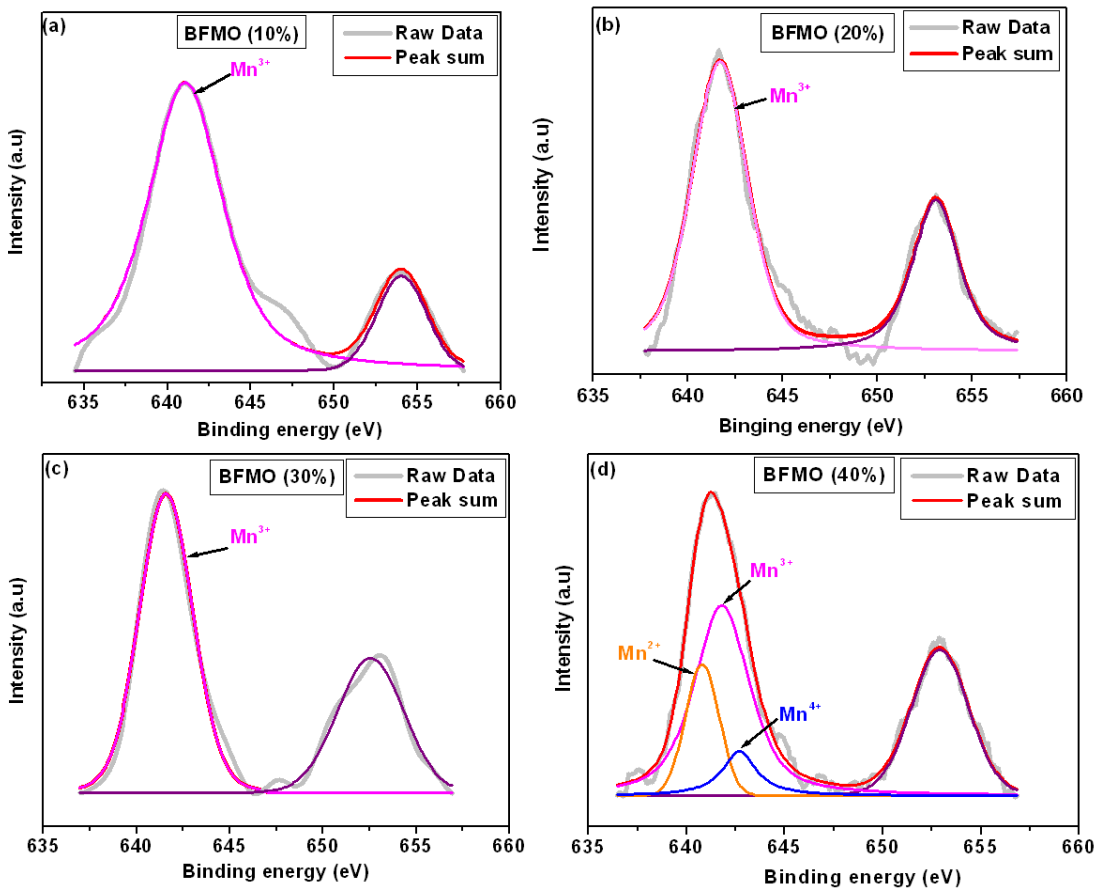

Figure 3.33 XPS spectra for Mn 2*p* in BFMO samples with (a) $x = 0.1$; (b) $x = 0.2$; $x = 0.3$; and (d) $x = 0.4$.

3.11 Summary

In this chapter, we have given a comprehensive study on single phase BFMO (x=0–0.4) synthesized by the solid state reaction and rapid liquid-phase sintering techniques. The results showed that the doping of Mn promoted the normal grain growth and developed a superlattice structure. The superlattice structure was carefully studied by electron diffraction with the help of computer simulation. Ferroelectric, dielectric and magnetic properties of the BFMO system were also studied and the results were analyzed in combination with the results obtained from Raman and XPS. The conduction mechanism in BFMO is found to be dominated by the hopping through the Fe^{3+}-O^{2+}-Mn^{3+} chain. The activation energy slightly decreased with increasing amount of Mn doping. Moreover, the activation energies for grain and grain boundary conductions were nearly the same, supporting the constriction resistance model for grain boundary. The magnetization of BFMO was increased with increasing amount of Mn doping. This was resulted from the destruction of the spiral spin structure by doping of Mn ions.

Chapter 4
Preliminary Results of Novel Synthesized Method

4.1 Introduction

As discussed in the previous chapter, the physical properties of BFO are very sensitivity to the synthesis conditions because BFO is in a metastable phase and can be easily decomposed to form secondary phases during sintering or calcination procedures. To further study the effect of processing conditions on the physical properties, a novel synthesis method (wet chemical reaction) will be adopted and the results will be presented and discussed in this chapter.

This chapter will start with the investigation on crystallization and phase stability of BFO synthesized by the wet chemical reaction method. Preliminary results of BFO will then be discussed and compared with those of BFO synthesized by other methods as shown in Chapter 3.

4.2 Crystalline study

Figure 4.1 shows the XRD patterns of the complex powders (which was synthesized by the wet chemical method as described in Chapter 2) calcined at different temperatures. The XRD pattern of the synthesized complex powders before calcination is also shown and it agrees well with that of $Bi[Fe(CN)_6]\bullet nH_2O$, showing a hexagonal structure (space group: P63/m). It can be found that single perovskite phase BFO can be obtained at a calcination temperature of 700°C or above. As discussed previously, BFO is metastable and will be decomposed into secondary phases, such as $Bi_2Fe_4O_9$ and/or $Bi_{12}(Bi_{0.5}Fe_{0.5})O_{19.5}$, after high temperature treatment. Moreover, Bi_2O_3 is volatile under a high temperature. Hence it is hard to obtain stoichiometric BFO though either the conventional solid-state reaction and/or the rapid liquid-phase sintering techniques. By using the wet chemical reaction method, single phase BFO was easily obtained and was stable even after the calcination at 900°C, much more stable than BFO synthesized by the other two methods as described in Chapter 2. The lattice parameters are summarized in Table 4.1, which agree well with the results obtained from samples synthesized by rapid liquid-phase sintering method as shown in section 3.2. It can be seen that the unit cell volume decreases with increasing calcination temperatures at above 700°C. This volume constriction may be related to the core-shell structure developed, which will be discussed below. The surface stress from the shell causes the observed volume constriction and stabilizes the structure.

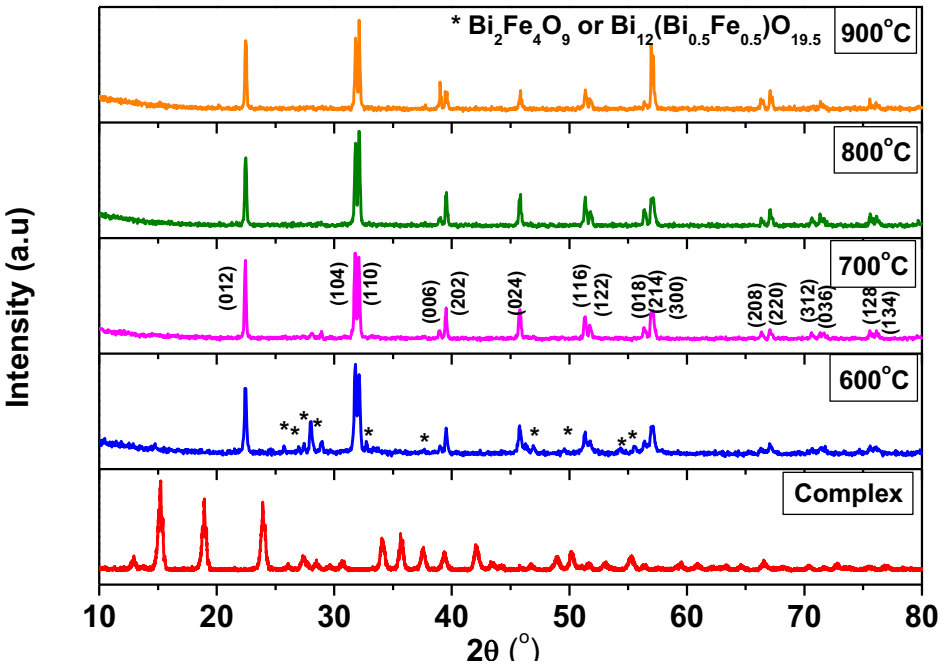

Figure 4.1 XRD diffraction patterns of BFO powders synthesized by chemical reaction method.

Temperature (℃)	a (Å)	α (◦)	V (Å^3)
600	3.9622	89.415	62.19
700	3.9628	89.466	62.22
800	3.9604	89.561	62.11
900	3.9581	89.579	62

Table 4.1 Lattice parameters of BFO calcined at different temperatures.

It has been reported that BFO is metastable and has a narrow processing window. High temperature treatment will cause the decomposition of metastable BFO to form secondary phases [97, 98]. However, the BFO synthesized by the wet chemical method

is stable up to a temperature as high as 900°C. This high stability can be explained by the compressive stress developed on the surface of BFO particles since it has been reported that the compressive stress can enhance the stability of BFO [99]. According to the XPS results below (section 4.5), the surface of BFO particles was composed of a large amount of Fe^{2+} ions. Correspondingly, a large amount of oxygen vacancies were formed for charge compensation. Therefore, the coordination number for Fe and Bi ions was reduced. Similar to a model proposed in nanosized ferroelectric particles [100], the reduced coordination number resulted in the chemical bond contraction and an equivalent compressive stress was developed in the BFO particles. Such a compressive stress would stabilize the structure of BFO. This model was also consistent with the XRD study, showing a decreased unit cell volume for BFO synthesized by the wet chemical method as compared to that for BFO synthesized by the solid state reaction and the rapid liquid-phase sintering methods.

The morphologies of BFO powders calcined at different temperatures were shown in Figure 4.2. The size of the particles is around 100-400 nm.

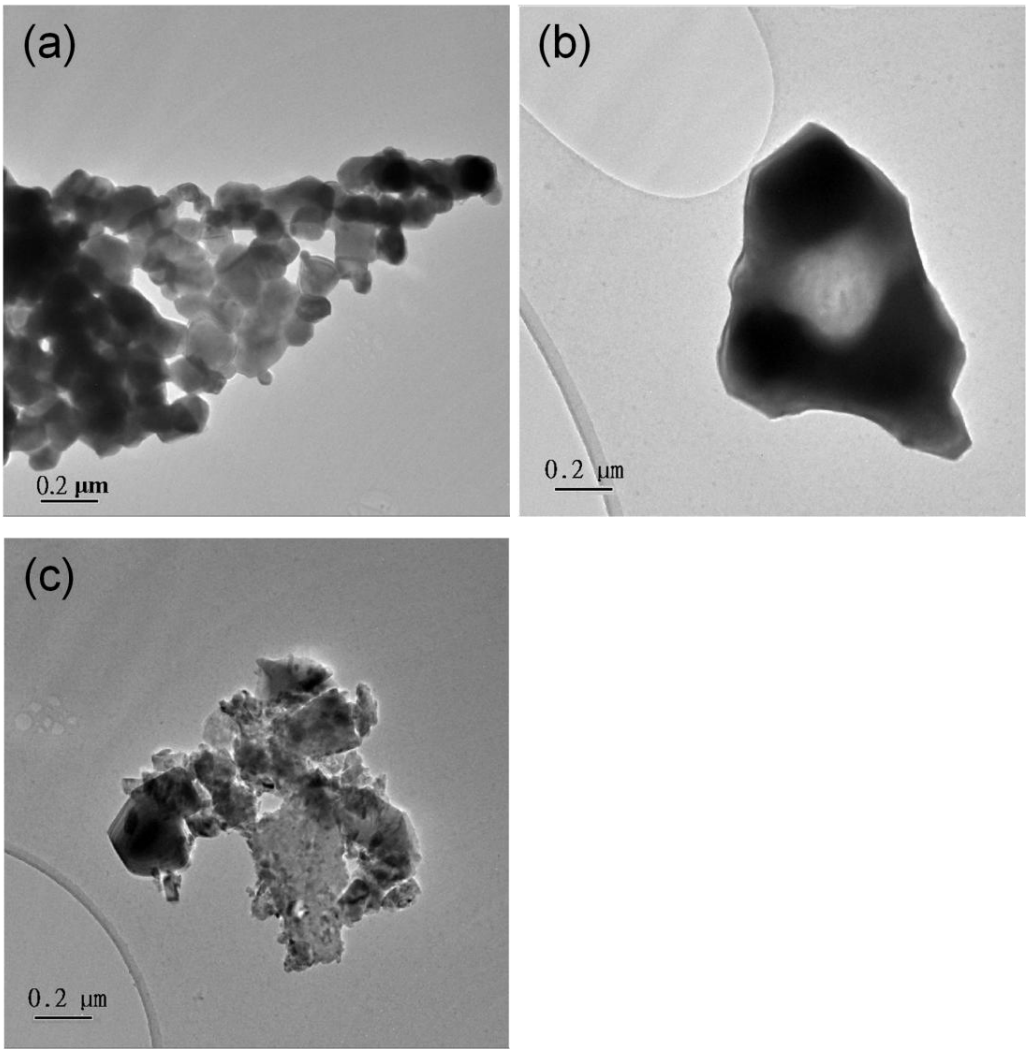

Figure 4.2 TEM pictures of BFO powders calcined at (a) 600°C, (b) 700°C, and (c) 900°C.

The BFO powders synthesized by the wet chemical method are not only stable in phase, but also stable in composition. Stoichiometric BFO can be synthesized even if the starting composition ratio is $Bi(NO_3)_3 \cdot 5H_2O$:$K_3Fe(CN)_6$=1:2, which is

non-stoichiometric. As proved by the XRD patterns in Figure 4.3, after the calcination at 700°C for 1 hour, the final product is still a single phase BFO. This shows that the extra amount of Fe ions in $K_3Fe(CN)_6$ did not react with the Bi ions in $Bi(NO_3)_3 \cdot 5H_2O$ to form the complex powder. Therefore, the composition of BFO can be precisely controlled by this wet chemical reaction method.

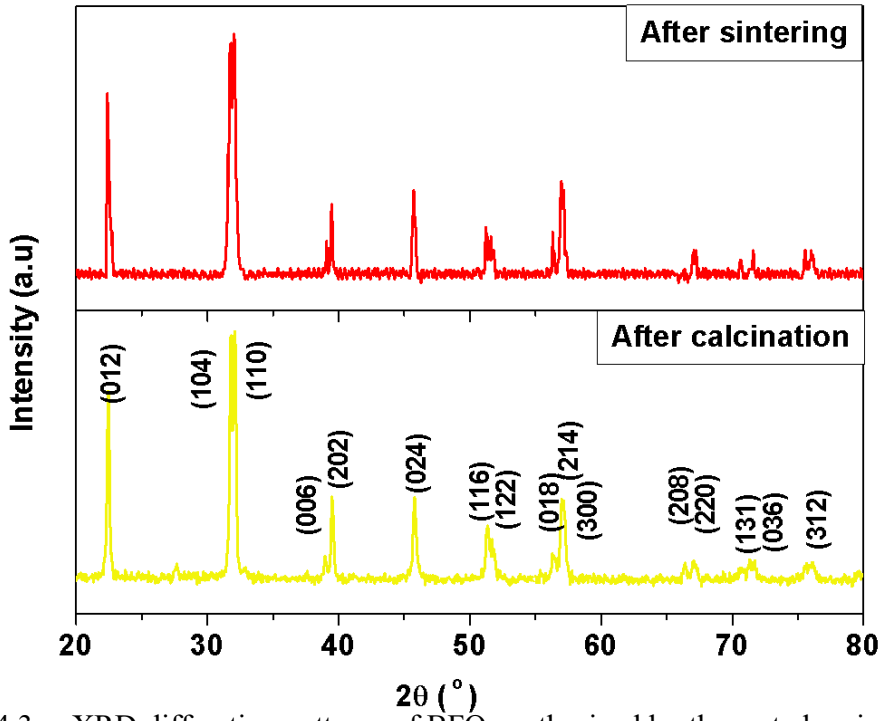

Figure 4.3 XRD diffraction patterns of BFO synthesized by the wet chemical reaction method with a starting composition ratio of $Bi(NO_3)_3 \cdot 5H_2O$:$K_3Fe(CN)_6$=1:2.

4.3 Ferroelectric and dielectric properties

BFO synthesized by the wet chemical method exhibited a high leakage current and the ferroelectric *P-E* hysteresis loop could not be measured. This high leakage current resulted from the high concentration of Fe^{2+}, which was confirmed by XPS result as shown in Figure 4.7. As compared to the samples synthesized by the solid-state reaction and liquid-phase sintering methods, BFO synthesized by the chemical method shows higher leakage current which depends strongly on the concentration of Fe^{2+} and oxygen vacancies formed.

The dielectric properties of BFO synthesized by the wet chemical method are shown in Figure 4.4. Two relaxations, one in a low temperature region and the other in a high temperature one, can be clearly observed. The activation energies associated with these relaxations are 0.39 and 0.61 eV, respectively as deduced from the Arrhenius plot (

Figure 4.5) where ln(*f*) is plotted against 1000/T. The activation energy of 0.39 eV is related to the typical hopping motion between Fe^{2+} and Fe^{3+}, where the existence of Fe^{2+} has been confirmed by the XPS spectra (to be shown in section 4.5). The activation energy of 0.61 eV is related to the thermal activation of oxygen vacancies. It is the existence of large amount of Fe^{2+} and oxygen vacancies that results in the leaky BFO ceramics.

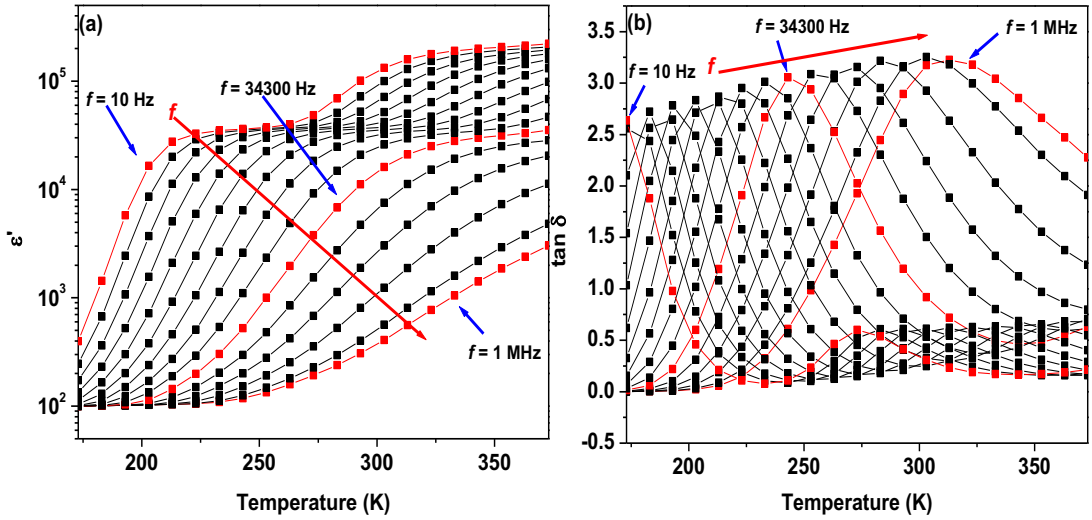

Figure 4.4 Dielectric properties of BFO ceramics synthesized by the wet chemical reaction method: (a) relative dielectric permittivity ε' and (b) dielectric loss tanδ.

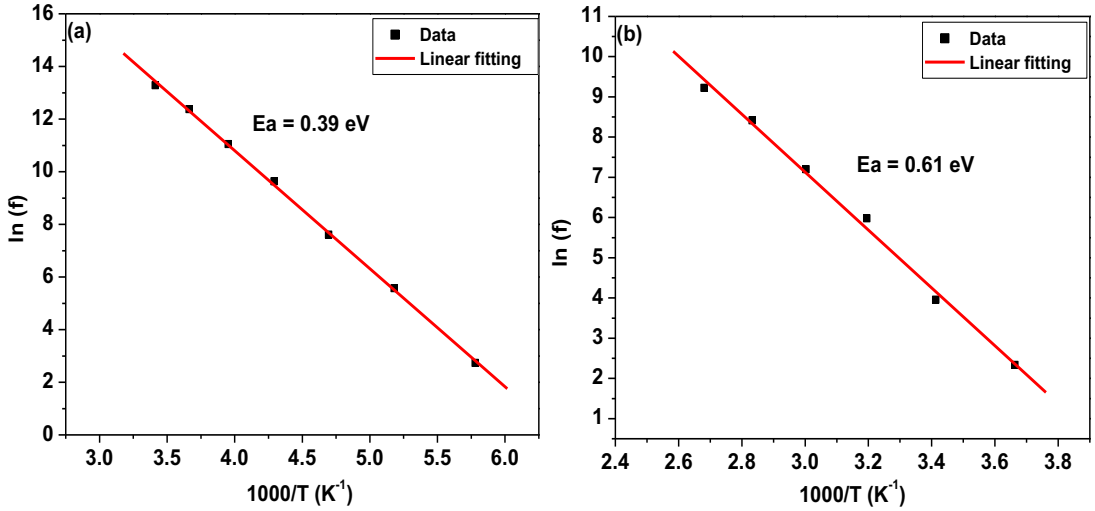

Figure 4.5 Arrhenius plot of the two relaxations in BFO synthesized by the wet chemical reaction method: (a) low temperature relaxation and (b) high temperature relaxation.

4.4 Magnetic properties

Figure 4.6 shows the magnetic hysteresis loop of BFO synthesized by the wet chemical reaction method. A ferromagnetic behavior can be observed. This ferromagnetic behavior should not be the intrinsic property of BFO since it has been reported that BFO is G-type antiferromagnetic [24]. The ferromagnetic property might be induced by Fe^{2+} in the sample [101-103]. This is similar to the ferromagnetic behavior found in BFO synthesized by the solid state reaction method (as discussed in Chapter 3), which contains a large amount of Fe^{2+} to induce ferromagnetic property of BFO.

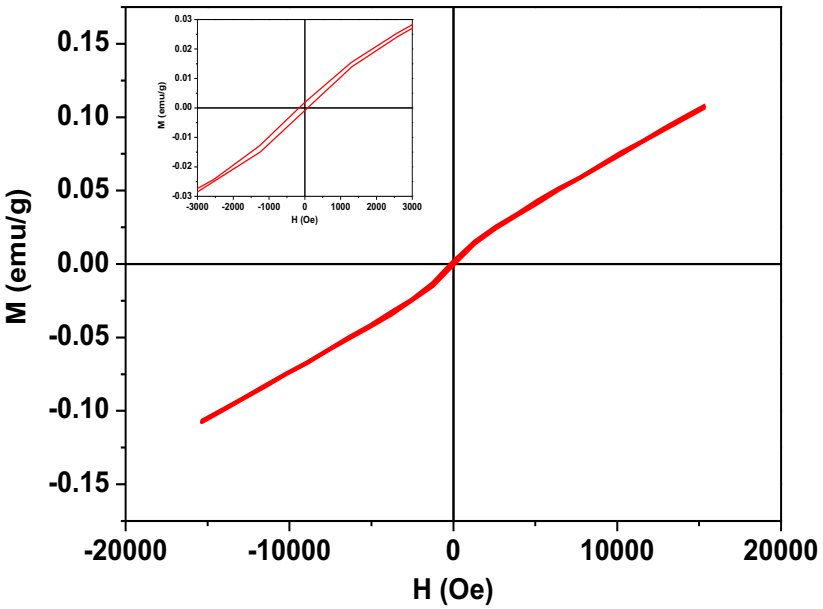

Figure 4.6 Magnetization versus magnetic field (*M-H*) curve of BFO ceramic synthesized by the wet chemical reaction method and measured at room temperature. (Inset) Enlarged *M-H* curve near the zero field region.

4.5 Valence state

Figure 4.7 shows the XPS spectrum (Fe 2*p* line) of BFO synthesized by the wet chemical reaction method. The measured Fe $2p_{3/2}$ peak which is located at around 710eV can be regarded as the superposition of two peaks corresponding to Fe^{2+} and Fe^{3+} states, respectively [94]. The coexistence of both Fe^{3+} and Fe^{2+} states can be confirmed in the sample. Moreover, it is found that the wet chemical reaction method introduces more Fe^{2+} than the solid state reaction and rapid liquid-phase sintering methods do. The existence of Fe^{2+} causes the formation of oxygen vacancies for charge compensation. The large amount of Fe^{2+} and associated oxygen vacancies will bring about significant different physical properties as compared to BFO synthesized by others methods.

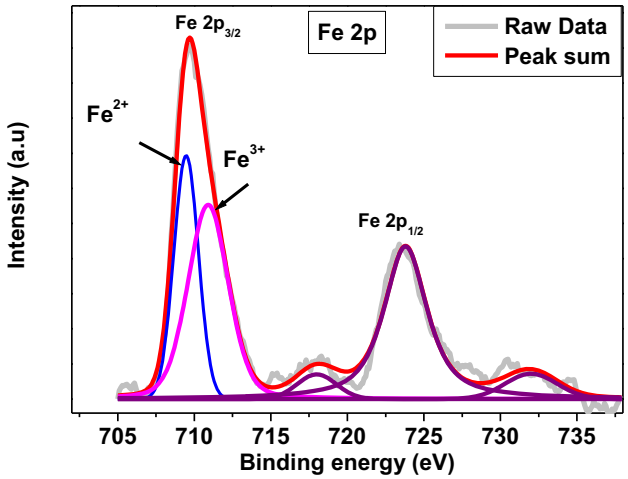

Figure 4.7 XPS spectrum of Fe 2*p* in BFO synthesized by wet chemical reaction method.

4.6 Summary

In this chapter, the preliminary results of BFO synthesized by a novel method (wet chemical reaction) are shown. The experimental results demonstrated that BFO synthesized by the wet chemical reaction method was highly stable up to an annealing temperature of 900°C. The synthesized BFO also had a stoichiometric composition which was insensitive to the starting Bi/Fe ratio before synthesis. Two types of dielectric relaxations were observed in BFO ceramics. The calculated activation energies were 0.39 and 0.61 eV, which were related to the hopping motion of Fe^{2+}-O-Fe^{3+} and the migration of oxygen vacancies, respectively. A large amount of Fe^{2+} states was found to exist in the sample and this was the reason that a ferromagnetic-like hysteresis loop was observed in BFO synthesized by the wet chemical method.

Chapter 5
Conclusion and Suggestions for Future Work

5.1 Conclusion

We have systematically investigated multiferroic perovskite BFMO (x=0–0.4) ceramics synthesized by various methods and particularly by the rapid liquid-phase sintering technique. Their phase, structure, dielectric and magnetic properties were studied. The main conclusions can be summarized as follows.

XRD results showed a structural phase transition from hexagonal to tetragonal in BFMO when x=0.4. Superlattice structure was observed in the electron diffraction patterns. The ¼<111>-type superlattice spots observed in BFMO when x≥0.2 might arise from the cation ordering while the possibility for oxygen vacancy ordering could be excluded. The dielectric properties were dependent on the Mn doping level and a strong dielectric relaxation was found in Mn doped BFO samples, which was absent in pure BFO. The relaxation frequencies shifted to higher frequencies with increasing Mn content. The relaxation could be well described by the Arrhenius law and the activation energy decreased from 0.39 (x=0.1) to 0.29 eV (x=0.4), which implied that the relaxation mechanism was related to the Mn-dependent hopping motion between Fe^{3+} and Mn^{3+} ions. Cole-Cole plot was used to analyze the effect of grain and grain boundary based on the equivalent circuit model. The activation energies for grain and grain boundary

conduction were nearly the same and this could be well explained by the constriction resistance model. The doping of Mn also resulted in the increase of magnetization which was due to the suppression of the spiral spin structure by Mn doping. The XPS results indicated that the main valence states for Fe and Mn are +3. A small amount of Fe^{2+} also existed, but it was independent of the doping level of Mn. Mixed valence states of Mn occurred in BFMO (x=0.4). Raman spectra suggested that there were structural distortions in Mn doped samples and Mn^{3+} induced a strong Jahn-Teller octahedral distortion especially in BFMO (x=0.4).

Among the various synthesis techniques used in this study, single phase BFO ceramics could only be synthesized by the rapid liquid-phase sintering and wet chemical reaction methods. The samples synthesized by the rapid liquid-phase sintering exhibited the least leakage current. The difference in leakage current could be due to the difference in the concentration of Fe^{2+} and associated oxygen vacancies. The wet chemical reaction method proved to be an effective technique to obtain stable and stoichiometric single phase BFO. The stability of BFO particle was related to the compressive stress developed on the particles surface which resulted from the chemical bond contraction.

5.2 Suggestions for future work

The current work has studied the structural and physical properties of perovskite BFMO (x=0–0.4) ceramics. However, several issues remain unresolved and need to be further studied. Below are some suggestions for further investigation and can be

regarded as an extension of the present work.

Searching appropriate annealing conditions under different atmosphere (N_2 or O_2) can further help understand the dominate effect for the giant dielectric permittivity observed since several other factors (interface effect, grain size effect and so on) may also contribute the permittivity of BFMO. The detailed mechanism for the giant dielectric permittivity needs to be further studied.

In the current work, a novel wet chemical reaction method has been tried to synthesize BFO nano powders. It is an effective method to obtain stoichiometric and stable single phase BFO. Due to time constraint, only a few preliminary results were obtained from BFO synthesized by this method. A comprehensive work needs to be conducted to further explore this novel synthesis method. Future work will be performed to answer the following questions: (1) Why is the synthesized BFO stable up to 900°C? (2) What is the detailed microstructure? and (3) Can this wet chemical reaction method be extended to the synthesis of doped BFO ceramics, such as BFMO?

Reference

[1] Curie P. On Symmetry in Physical Phenomena, Symmetry of an Electric Field and of a Magnetic Field. Journal de Physique. 1894;3:393.

[2] Fiebig M. Revival of the magnetoelectric effect. Journal of Physics D-Applied Physics. 2005;38(8):R123-R52.

[3] Eerenstein W, Mathur ND, Scott JF. Multiferroic and magnetoelectric materials. Nature. 2006;442(7104):759-65.

[4] Fiebig M, Lottermoser T, Frohlich D, Goltsev AV, Pisarev RV. Observation of coupled magnetic and electric domains. Nature. 2002;419:818-20.

[5] Wang J, Neaton J B, Zheng H, Nagarajan V, Ogale S B, Liu B, Viehland D, Vaithyanathan V, Schlom D G, Waghmare U V, Spaldin N A, M RK, Wuttig M, Ramesh R. Epitaxial $BiFeO_3$ multiferroic thin film heterostructures. Science. 2003;299:1719-22.

[6] Hur N, Park S, Sharma PA, Guha S, Cheong SW. Colossal Magnetodielectric Effects in $DyMn_2O_5$. Physical Review Letters. 2004;93(10):107207.

[7] Goldschmidt VM. Geochemische verteilungsgesetze der elemente, I Mater Naturvid Kl no 2 Oslo: Skrifter Norske Videskaps-Akad. 1926.

[8] Muller O, Roy R. The Major Ternary Structural Families. Springer-Verlag New York. 1974.

[9] Reaney IM, Colla EL, Setter N. Dielectric and Structural Characteristics of Ba- and Sr-based Complex Perovskites as a Function of Tolerance Factor.

Japanese Journal of Applied Physics. 1994;33.

[10] Woodward DI, Reaney IM. Electron diffraction of tilted perovskites. Acta Crystallographica Section B: Structural Science. 2005;61:387--99.

[11] Buscaglia MT, Buscaglia V, Viviani M, Petzelt J, Savinov M, Mitoseriu L, Testino A, Nanni P, Harnagea C, Zhao Z, Nygren M. Ferroelectric properties of dense nanocrystalline $BaTiO_3$ ceramics. Nanotechnology. 2004;15(9):1113-7.

[12] Barsoum MW. Fundamentals of ceramics. The McGraw-Hill Companies, Inc. 1997:559-608.

[13] Ruette. B. MS thesis. Virginia Tech. 2003.

[14] Popov YF. Features of the magnetoelectric properties of $BiFeO_3$ in high magnetic fields. Journal of Low Temperature Physics. 2001;27:478-9.

[15] Wang YP, Zhou L, Zhang MF, Chen XY, Liu JM, Liu ZG. Room-temperature saturated ferroelectric polarization in $BiFeO_3$ ceramics synthesized by rapid liquid phase sintering. Applied Physics Letters. 2004;84(10):1731-3.

[16] Yuan GL, Or SW, Wang YP, Liu ZG, Liu JM. Preparation and multi-properties of insulated single-phase $BiFeO_3$ ceramics. Solid State Communications. 2006;138:76-81.

[17] Kumar MM, Palkar VR, Srinivas K, Suryanarayana SV. Ferroelectricity in a pure $BiFeO_3$ ceramic. Applied Physics Letters. 2000;76(19):2764-6.

[18] Popov YF, Zvezdin AK, Vorobev GP, Kadomtseva AM, Murashev VA, Rakov DN. Linear magnetoelectric effect and phase-transitions in bismuth

ferrite, $BiFeO_3$. Jetp Letters. 1993;57(1):69-73.

[19] Kubel F, Schmid H. Structure of a Ferroelectric and Ferroelastic Monodomain Crystal of the Perovskite $BiFeO_3$. Acta Crystallographica Section B-Structural Science. 1990;46:698-702.

[20] Bucci JD, Robertso.Bk, James WJ. Precision determination of lattice parameters and coefficients of thermal expansion of $BiFeO_3$. J Appl Crystallogr. 1972;5(JUN1):187.

[21] Haumont R, Kreisel J, Bouvier P, Hippert F. Phonon anomalies and the ferroelectric phase transition in multiferroic $BiFeO_3$. Physical Review B. 2006 Apr;73(13):4.

[22] Seshadri R, Hill NA. Visualizing the Role of Bi 6s " Lone Pairs" in the Off-Center Distortion in Ferromagnetic BiMnO3. Chemistry of Materials. 2001;13(9):2892-9.

[23] Neaton JB, Ederer C, Waghmare UV, Spaldin NA, Rabe KM. First-principles study of spontaneous polarization in multiferroic $BiFeO_3$. Physical Review B. 2005;71(1):014113.

[24] Sosnowska I, Peterlinneumaier T, Steichele E. Spiral Magnetic-ordering in bismuth ferrite. Journal of Physics C-Solid State Physics. 1982;15(23):4835-46.

[25] Zhang S-T, Zhang Y, Lu M-H, Du C-L, Chen Y-F, Liu Z-G, Zhu Y-Y, Ming N-B, Pan XQ. Substitution-induced phase transition and enhanced multiferroic properties of $Bi_{1-x}La_xFeO_3$ ceramics. Applied Physics Letters. 2006;88(16):162901-3.

[26] Sosnowska I, Schaffer W, Kockelmann W, Andersen KH, Troyanchuk IO.

Crystal structure and spiral magnetic ordering of $BiFeO_3$ doped with manganese. Applied Physics a-Materials Science & Processing. 2002;74:S1040-S2.

[27] Sugawara F, Iiida S, Syono Y, Akimoto S. Magnetic Properties and Crystal Distortions of $BiMnO_3$ and $BiCrO_3$. Journal of the Physical Society of Japan. 1968;25:1553.

[28] Atou T, Chiba H, Ohoyama K, Yamaguchi Y, Syono Y. Structure Determination of Ferromagnetic Perovskite $BiMnO_3$. Journal of Solid State Chemistry. 1999;145(2):639-42.

[29] Kimura T, Kawamoto S, Yamada I, Azuma M, Takano M, Tokura Y. Magnetocapacitance effect in multiferroic $BiMnO_3$. Physical Review B. 2003;67(18):180401.

[30] Bokov. VA, Mylnikova. IE, Kizhaev. SA, Bryzhina. MF, Grigorian. NA. Structure and magnetic properties of $BiMnO_3$. Soviet Physics-Solid State. 1966;7:2993–4.

[31] Moreira dos Santos A, Cheetham AK, Atou T, Syono Y, Yamaguchi Y, Ohoyama K, Chiba H, Rao CNR. Orbital ordering as the determinant for ferromagnetism in biferroic $BiMnO_3$. Physical Review B. 2002;66(6):064425.

[32] Moreira dos Santos A, Parashar S, Raju AR, Zhao YS, Cheetham AK, Rao CNR. Evidence for the likely occurrence of magnetoferroelectricity in the simple perovskite, $BiMnO_3$. Solid State Communications. 2002;122(1-2):49-52.

[33] Eerenstein W, Morrison FD, Scott JF, Mathur ND. Growth of highly

resistive $BiMnO_3$ films. Applied Physics Letters. 2005;87(10):101906-3.

[34] Kundu AK, Ranjith R, Kundys B, Nguyen N, Caignaert V, Pralong V, Prellier W, Raveau B. A multiferroic ceramic with perovskite structure: $(La_{0.5}Bi_{0.5})(Mn_{0.5}Fe_{0.5})O_{3.09}$. Applied Physics Letters. 2008;93(5).

[35] Sahu JR, Rao CNR. Beneficial modification of the properties of multiferroic $BiFeO_3$ by cation substitution. Solid State Sciences. 2007;9(10):950-4.

[36] Palkar VR, Kundaliya DC, Malik SK. Effect of Mn substitution on magnetoelectric properties of bismuth ferrite system. Journal of Applied Physics. 2003;93(7):4337-9.

[37] Bi L, Taussig AR, Kim H-S, Wang L, Dionne GF, Bono D, Persson K, Ceder G, Ross CA. Structural, magnetic, and optical properties of $BiFeO_3$ and Bi_2FeMnO_6 epitaxial thin films: An experimental and first-principles study. Physical Review B (Condensed Matter and Materials Physics). 2008;78(10):104106-10.

[38] Yang CH, Koo TY, Jeong YH. How to obtain magnetocapacitance effects at room temperature: The case of Mn-doped $BiFeO_3$. Solid State Communications. 2005;134:299-301.

[39] Azuma M, Kanda H, Belik AA, Shimakawa Y, Takano M. Magnetic and structural properties of $BiFe_{1-x}Mn_xO_3$. Journal of Magnetism and Magnetic Materials. 2007;310(2, Part 2):1177-9.

[40] Kothari D, Reddy VR, Gupta A, Phase DM, Lakshmi N, Deshpande SK, Awasthi AM. Study of the effect of Mn doping on the $BiFeO_3$ system. Journal of Physics: Condensed Matter. 2007;19(13):136202.

[41] Singh SK, Ishiwara H, Maruyama K. Room temperature ferroelectric properties of Mn-substituted $BiFeO_3$ thin films deposited on Pt electrodes using chemical solution deposition. Applied Physics Letters. 2006;88(26):262908-3.

[42] Kumar M, Yadav KL. Rapid liquid phase sintered Mn doped $BiFeO_3$ ceramics with enhanced polarization and weak magnetization. Applied Physics Letters. 2007;91(24):242901-3.

[43] Baettig P, Spaldin NA. Ab initio prediction of a multiferroic with large polarization and magnetization. Applied Physics Letters. 2005;86(1):012505-3.

[44] Azuma M, Takata K, Saito T, Ishiwata S, Shimakawa Y, Takano M. Designed Ferromagnetic, Ferroelectric Bi_2NiMnO_6. Journal of the American Chemical Society. 2005;127(24):8889-92.

[45] Nechache R, Harnagea C, Pignolet A, Normandin F, Veres T, Carignan L-P, Menard D. Growth, structure, and properties of epitaxial thin films of first-principles predicted multiferroic Bi_2FeCrO_6. Applied Physics Letters. 2006;89(10):102902-3.

[46] Tan X, Wongmaneerung R, McCallum RW. Ferroelectric and magnetic properties of $Pb(Fe_{2/3}W_{1/3})O_3$-based multiferroic compounds with cation order. Journal of Applied Physics. 2007;102(10):104114-6.

[47] Yasui S, Uchida H, Nakaki H, Nishida K, Funakubo H, Koda S. Analysis for crystal structure of $Bi(Fe,Sc)O_3$ thin films and their electrical properties. Applied Physics Letters. 2007;91(2):022906-3.

[48] Davies PK. Cation ordering in complex oxides. Current Opinion in Solid

State and Materials Science. 1999;4(5):467-71.

[49] Reaney IM, Petzelt J, Voitsekhovskii VV, Chu F, Setter N. B-site order and infrared reflectivity in A(B'B'')O_3 complex perovskite ceramics. Journal of Applied Physics. 1994;76(4):2086-92.

[50] Levin I, Chan JY, Geyer RG, Maslar JE, Vanderah TA. Cation Ordering Types and Dielectric Properties in the Complex Perovskite $Ca(Ca_{1/3}Nb_{2/3})O_3$. Journal of Solid State Chemistry. 2001;156:122-34.

[51] Colla EL, Reaney IM, Setter N. Effect of structural changes in complex perovskites on the temperature coefficient of the relative permittivity. Journal of Applied Physics. 1993;74(5):3414-25.

[52] Peter K. Davies JT, Taki Negas,. Effect of Ordering-Induced Domain Boundaries on Low-Loss $Ba(Zn_{1/3}Ta_{2/3})O_3$-$BaZrO_3$ Perovskite Microwave Dielectrics. Journal of the American Ceramic Society. 1997;80(7):1727-40.

[53] Chai L, Davies PK. Effect of M^{4+} (Ce, Sn, Ti) B-site substitutions on the cation ordering in $Ba(Mg_{1/3}Ta_{2/3})O_3$. Materials Research Bulletin. 1998;33(8):1283-92.

[54] Liang Chai PKD. Formation and Structural Characterization of 1:1 Ordered Perovskites in the $Ba(Zn_{1/3}Ta_{2/3})O_3$-$BaZrO_3$ System. Journal of the American Ceramic Society. 1997;80(12):3193-8.

[55] Park J-H, Woodward PM, Parise JB, Reeder RJ, Lubomirsky I, Stafsudd O. Synthesis, Structure, and Dielectric Properties of $(Bi_{1/2}Ag_{1/2})TiO_3$. Chemistry of Materials. 1999;11(1):177-83.

[56] Davies PK, Wu H, Borisevich AY, Molodetsky IE, Farber L. Crystal

Chemistry of Complex Perovskites: New Cation-Ordered Dielectric Oxides. Annual Review of Materials Research. 2008;38(1):369-401.

[57] Wongmaneerung R, Tan X, McCallum RW, Ananta S, Yimnirun R. Cation, dipole, and spin order in $Pb(Fe_{2/3}W_{1/3})O_3$-based magnetoelectric multiferroic compounds. Applied Physics Letters. 2007;90(24):242905-3.

[58] Qu W, Tan X, McCallum RW, Cann DP, Ustundag E. Room temperature magnetoelectric multiferroism through cation ordering in complex perovskite solid solutions. Journal of Physics: Condensed Matter. 2006;18(39):8935-42.

[59] Uratani Y, Shishidou T, Ishii F, Oguchi T. First-principles exploration of ferromagnetic and ferroelectric double-perovskite transition-metal oxides. Physica B: Condensed Matter. 2006;383(1):9-12.

[60] Kumar MM, Palkar VR, Srinivas K, Suryanarayana SV. Ferroelectricity in a pure $BiFeO_3$ceramic. Applied Physics Letters. 2000;76(19):2764-6.

[61] Morozov MI, Lomanova NA, Gusarov VV. Specific Features of $BiFeO_3$ Formation in a Mixture of Bismuth(III) and Iron(III) Oxides. Russian Journal of General Chemistry. 2003;73(11):1676-80.

[62] Lahmar A, Habouti S, Solterbeck C-H, Es-Souni M, Elouadi B. Correlation between structure, dielectric, and ferroelectric properties in $BiFeO_3$--$LaMnO_3$ solid solution thin films. Journal of Applied Physics. 2009;105(1):014111-8.

[63] Kartopu G, Lahmar A, Habouti S, Solterbeck CL, Elouadi B, Es-Souni M. Observation of structural transitions and Jahn--Teller distortion in $LaMnO_3$-doped $BiFeO_3$ thin films. Applied Physics Letters.

2008;92(15):151910-3.

[64] Tokura Y, Nagaosa N. Orbital Physics in Transition-Metal Oxides. Science. 2000 April 21, 2000;288(5465):462-8.

[65] Thrall M, Freer R, Martin C, Azough F, Patterson B, Cernik RJ. An in situ study of the formation of multiferroic bismuth ferrite using high resolution synchrotron X-ray powder diffraction. Journal of the European Ceramic Society. 2008;28(13):2567-72.

[66] Pradhan AK, Zhang K, Hunter D, Dadson JB, Loiutts GB, Bhattacharya P, Katiyar R, Zhang J, Sellmyer DJ, Roy UN, Cui Y, Burger A. Magnetic and electrical properties of single-phase multiferroic $BiFeO_3$. Journal of Applied Physics. 2005;97(9):093903-4.

[67] Shen ZJ, Chen WP, Yuan GL, Liu JM, Wang Y, Chan HLW. Hydrogen-induced degradation in multiferroic $BiFeO_3$ ceramics. Materials Letters. 2007;61(22):4354-7.

[68] Yuan GL, Yang Y, Or SW. Aging-induced double ferroelectric hysteresis loops in $BiFeO_3$ multiferroic ceramic. Applied Physics Letters. 2007;91(12):122907-3.

[69] Zhang LX, Chen W, Ren X. Large recoverable electrostrain in Mn-doped (Ba,Sr) TiO_3 ceramics. Applied Physics Letters. 2004;85(23):5658-60.

[70] Sun D, Ren X, Otsuka K. Stabilization effect in ferroelectric materials during aging in ferroelectric state. Applied Physics Letters. 2005;87(14):142903-3.

[71] Zhang L, Ren X. Aging behavior in single-domain Mn-doped $BaTiO_3$ crystals: Implication for a unified microscopic explanation of ferroelectric

aging. Physical Review B (Condensed Matter and Materials Physics). 2006;73(9):094121-6.

[72] Woodward DI, Reaney IM, Eitel RE, Randall CA. Crystal and domain structure of the $BiFeO_3$--$PbTiO_3$ solid solution. Journal of Applied Physics. 2003;94(5):3313-8.

[73] Huang H, Zhou LM, Guo J, Hng HH, Oh JT, Hing P. F spots and domain patterns in rhombohedral $PbZr_{0.9}Ti_{0.1}O_3$. Applied Physics Letters. 2003;83(18):3692-4.

[74] Sosnowska I, Przenioslo R, Fischer P, Murashov VA. Neutron diffraction studies of the crystal and magnetic structures of $BiFeO_3$ and $Bi_{0.93}La_{0.07}FeO_3$. Journal of Magnetism and Magnetic Materials. 1996;160:384-5.

[75] Yang H, Chi ZH, Yao LD, Zhang W, Li FY, Jin CQ, Yu RC. Structural defects in multiferroic $BiMnO_3$ studied by transmission electron microscopy and electron energy-loss spectroscopy. Journal of Applied Physics. 2006;100(4):044105-6.

[76] Yang H, Chi ZH, Li FY, Jin CQ, Yu RC. Ordered oxygen-deficient superlattice from electron irradiation of biferroic $BiMnO_3$. Physical Review B (Condensed Matter and Materials Physics). 2006;73(2):024114-6.

[77] Qi X, Dho J, Tomov R, Blamire MG, MacManus-Driscoll JL. Greatly reduced leakage current and conduction mechanism in aliovalent-ion-doped $BiFeO_3$. Applied Physics Letters. 2005;86(6):062903-3.

[78] William L. Warren KV, Duane Dimos, Gordon E. Pike, Bruce A. Tuttle,.

Oxygen Vacancy Motion in Perovskite Oxides. Journal of the American Ceramic Society. 1996;79(2):536-8.

[79] Ikeda N, Ohsumi H, Ohwada K, Ishii K, Inami T, Kakurai K, Murakami Y, Yoshii K, Mori S, Horibe Y, Kito H. Ferroelectricity from iron valence ordering in the charge-frustrated system $LuFe_2O_4$. Nature. 2005;436(7054):1136-8.

[80] Wang H, Huang H, Wang B. Effect of Mn Substitution for Fe in Multiferroic $BiFeO_3$: A First-Principles Study. Science of Advanced Materials. in press.

[81] Bruce PG, West AR. The A-C Conductivity of Polycrystalline LISICON, $Li_{2+2x}Zn_{1-x}GeO_4$, and a Model for Intergranular Constriction Resistances. Journal of The Electrochemical Society. 1983;130(3):662-9.

[82] Roca RA, Botero ER, Guerrero F, Guerra JDS, Garcia D, Eiras JA. Effect of the sintering conditions on the electrical properties of Nd^{3+} modified PLZT ceramics. Journal of Physics D: Applied Physics. 2008;41(4):045410.

[83] Li M, Feteira A, Sinclair DC. Origin of the high permittivity in $(La_{0.4}Ba_{0.4}Ca_{0.2})(Mn_{0.4}Ti_{0.6})O_3$ ceramics. Journal of Applied Physics. 2005;98(8):084101-6.

[84] Zhang ST, Lu MH, Wu D, Chen YF, Ming NB. Larger polarization and weak ferromagnetism in quenched $BiFeO_3$ ceramics with a distorted rhombohedral crystal structure. Applied Physics Letters. 2005;87(26):262907-3.

[85] Haumont R, Kreisel J, Bouvier P, Hippert F. Phonon anomalies and the ferroelectric phase transition in multiferroic $BiFeO_3$. Physical Review B

(Condensed Matter and Materials Physics). 2006;73(13):132101-4.

[86] Fukumura H, Harima H, Kisoda K, Tamada M, Noguchi Y, Miyayama M. Raman scattering study of multiferroic $BiFeO_3$ single crystal. Journal of Magnetism and Magnetic Materials. 2007;310(2, Part 2):e367-e9.

[87] Cazayous M, Malka D, Lebeugle D, Colson D. Electric field effect on $BiFeO_3$ single crystal investigated by Raman spectroscopy. Applied Physics Letters. 2007;91(7):071910-3.

[88] Kothari D, Raghavendra Reddy V, Sathe VG, Gupta A, Banerjee A, Awasthi AM. Raman scattering study of polycrystalline magnetoelectric $BiFeO_3$. Journal of Magnetism and Magnetic Materials. 2008;320(3-4):548-52.

[89] Yuan GL, Or SW, Chan HLW. Raman scattering spectra and ferroelectric properties of $Bi_{1-x}Nd_xFeO_3$ (x = 0--0.2) multiferroic ceramics. Journal of Applied Physics. 2007;101(6):064101-5.

[90] Hermet P, Goffinet M, Kreisel J, Ghosez P. Raman and infrared spectra of multiferroic bismuth ferrite from first principles. Physical Review B (Condensed Matter and Materials Physics). 2007;75(22):220102-4.

[91] Tutuncu HM, Srivastava GP. Electronic structure and zone-center phonon modes in multiferroic bulk BiFeO3. Journal of Applied Physics. 2008;103(8):083712-7.

[92] Martín-Carrón L, de Andrés A. Melting of the cooperative Jahn-Teller distortion in $LaMnO_3$ single crystal studied by Raman spectroscopy. The European Physical Journal B - Condensed Matter and Complex Systems. 2001;22(1):11-6.

[93] Kawasaki T, Ogimoto Y, Ogawa N, Miyano K, Tamaru H, Izumi M. Charge- and orbital-ordering patterns in $Bi_{1/2}Sr_{1/2}MnO_3$ thin films studied by Raman scattering. Journal of Applied Physics. 2007;101(12):123714-6.

[94] Grosvenor AP, Kobe BA, Biesinger MC, McIntyre NS. Investigation of multiplet splitting of Fe 2p XPS spectra and bonding in iron compounds. Surface and Interface Analysis. 2004;36(12):1564-74.

[95] Wei J, Xue D, Wu C, Li Z. Enhanced ferromagnetic properties of multiferroic $Bi_{1-x}Sr_xMn_{0.2}Fe_{0.8}O_3$ synthesized by sol-gel process. Journal of Alloys and Compounds. 2008;453(1-2):20-3.

[96] Chung C-F, Lin J-P, Wu J-M. Influence of Mn and Nb dopants on electric properties of chemical-solution-deposited $BiFeO_3$ films. Applied Physics Letters. 2006;88(24):242909-3.

[97] Haumont R, Kornev IA, Lisenkov S, Bellaiche L, Kreisel J, Dkhil B. Phase stability and structural temperature dependence in powdered multiferroic $BiFeO_3$. Physical Review B (Condensed Matter and Materials Physics). 2008;78(13):134108-8.

[98] Maître A, François M, Gachon J. Experimental study of the Bi_2O_3-Fe_2O_3 pseudo-binary system. Journal of Phase Equilibria and Diffusion. 2004;25(1):59-67.

[99] Selbach SM, Einarsrud M-A, Grande T. On the Thermodynamic Stability of $BiFeO_3$. Chemistry of Materials. 2008;21(1):169-73.

[100] Huang H, Sun CQ, Hing P. Surface bond contraction and its effect on the nanometric sized lead zirconate titanate. Journal of Physics: Condensed Matter. 2000;12(6):L127-L32.

[101] Huang F, Lu X, Wang Z, Lin W, Kan Y, Bo H, Cai W, Zhu J. Impact of annealing atmosphere on the multiferroic and dielectric properties of $BiFeO_3/Bi_{3.25}La_{0.75}Ti_3O_{12}$ thin films. Applied Physics A: Materials Science & Processing. 2009.

[102] Eerenstein W, Morrison FD, Dho J, Blamire MG, Scott JF, Mathur ND. Comment on "Epitaxial $BiFeO_3$ Multiferroic Thin Film Heterostructures". Science. 2005;307(5713):1203a.

[103] Wang J, Scholl A, Zheng H, Ogale SB, Viehland D, Schlom DG, Spaldin NA, Rabe KM, Wuttig M, Mohaddes L, Neaton J, Waghmare U, Zhao T, Ramesh R. Response to Comment on "Epitaxial BiFeO3 Multiferroic Thin Film Heterostructures". Science. 2005 February 25, 2005;307(5713):1203b-.